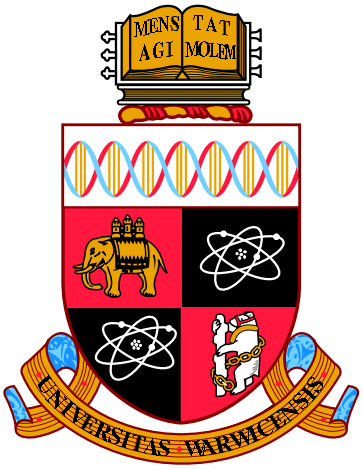

Development and Application of Electrochemical Scanning Probe Microscopy Techniques for Studying Interfacial Processes

by

Sophie Laura Kinnear

Thesis

Submitted to the University of Warwick

for the degree of

Doctor of Philosophy

Department of Chemistry

September 2015

THE UNIVERSITY OF WARWICK

Dedicated to all the dogs!

Contents

List of Tables

List of Figures

Abbreviations

AFM	Atomic Force Microscopy
APTES	(3-aminopropyl)triethoxysilane
BDM	Bockris, Devanathan, and Müller Model
BM	Bias Modulation
BNC	Bayonet NeillConcelman
C-AFM	Conductive Atomic Force Microscopy
CFC	Channel Flow Cell
CV	Cyclic Voltammetry
DDL	Diffuse Double Layer
DM	Distance Modulation
EBSD	Electron Backscatter Diffraction
EDL	Electric Double Layer
FE-SEM	Field Emission - Scanning Electron Microscopy
FIB	Focused Ion Beam
FIFO	First In First Out
FPGA	Field Programmable Gate Array
FT	Feedback Type
HAP	Calcium Hydroxyapatite
HOPG	Highly Orientated Pyrolytic Graphite
I16	16 Bit Signed Integer
ICR	Ion Current Rectification

IC-SECM	Intermitant Contact - Scanning Electrochemical Microscopy
IT	Current-Time
LSV	Linear Sweep Voltammetry
PLL	Poly-L-Lysine
PSD	Phase Sensitive Detector
PZC	Potential of Zero Charge
QRCE	Quasi-Reference Counter Electrode
RD	Rotating Disc
SAM	Self Assembled Monolayer
SECCM	Scanning Electrochemical Cell Microscopy
SECM	Scanning Electrochemical Microscopy
SG-TC	Substrate Generation - Tip Collection
SHE	Standard Hydorgen Electrode
SICM	Scanning Ion Conductance Microscopy
SIR	Surface Induced Retification
SPIP	Scanning Probe Image Processing
SPM	Scanning Probe Microscopy
STM	Scanning Tunnelling Microscopy
SVN	Subversion
SWNT	Single Walled Carbon Nanotube
TDMS	Technical Data Management System
TG-SC	Tip Generation - Substrate Collection
U64	64 Bit Unsigned Integer
UME	Ultra Micro Electrode
VI	Virtual Instrument

Glossary of Symbols

Symbol	Common Units	Description
A	V	Amplitude
A_n	-	New value to average
A_{sum}	-	Sum of average values
C_B	mM	Bulk concentration
c	mM	Concentration
$c*$	mM	Starting concentration
C_{sat}	M	Saturation concentration
D_b	$\mathrm{mm^2\,s^{-1}}$	Diffusion coeffiecnt
D_r	Hz	Data collection rate of FPGA card
e	C	Charge on an electron
E_b	V	Potential difference between barrels
f	Hz	Frequency
h	J	Planck's Constant
i_b	A	Conductance current
$\mathbf{J}$	$\mathrm{A\,m^{-2}}$	Current density vector
j	$\mathrm{mm^2\,s^{-1}}$	Diffusional flux
k	$\mathrm{mm^2\,s^{-1}}$	Dissolution flux
$\mathscr{K}$	$\mathrm{J\,K^{-1}}$	Boltzman Constant
m_c	µm	Menicus contact diameter
m_h	nm	Menicus height

$\mathbf{N}$	$\mathrm{mm^2\,s^{-1}}$	Flux vector
n	-	Inward unit vector
N	-	Number of data points to average
P	-	Proportional Factor
r_p	nm	Radius perpendicular to the septum
r_t	nm	Radius parelle to the septum
t	s	Time
T	K	Temperature
t_w	nm	Septum width
u_i	$\mathrm{S\,m^{-1}}$	Ionic conductivity of species i
x	nm	distance
z	C	Charge of speices
α	-	Slope of the current distance curve
ε	$\mathrm{F\,m^{-1}}$	Dielectric constant
θ	$^\circ$	Semi-angle of pipet
κ	$\mathrm{m^{-1}}$	Inverse thickness of the double layer
σ	$\mathrm{S\,m^{-1}}$	Solution conductivty
σ_m	$\mathrm{C\,m^{-2}}$	Charge density
ϕ	V	Applied potential
φ	$^\circ$	Phase shift
ϕ_0	V	Potential offset from pzc
ϕ_b	V	Bulk potential
ϕ_s	V	Surface Potential

Acknowledgments

I would like to express my gratitude to all the members of Warwick Electrochemistry and Interfaces Group, past and present. These four years have been an amazing experience of learning and working with you all. The group has really felt like a family, for good and bad! To the people in my year, this has been a fantastic journey to go on with you guys, thanks to Binoy Nadappuram, Jenny 'I spin my web in order to protect you' Webb and Changhui 'Hui' Chen and thanks to Barak Aaronson for always providing a challenge. Of course, I would also like to thank Rob Channonball for being a complete and utter dude, I still remember meeting you and Cat in first year of undergrad!

It has been a privilege to have worked with my supervisors, Patrick Unwin and Julie Macpherson, thanks to them both for their help and guidance. Thanks to my postdocs, Massimo Peruffo and Kim McKelvey whose experience and teachings were of invaluable help for the first half my PhD and Max Joseph for putting up with my constant stream of questions. This project benefited greatly from the amazing technical expertise of Alex Colburn and Rod Wesson, along with Lee Butcher and Marcus Grant from mechanical workshops. Thanks also to David Perry, Ashley Page and Dmitry Momotenko for working on the surface charge mapping projects, it was tough but it was rewarding. I feel privileged that I was accepted onto this course being funded by the European Research Council, who fully funded my studies for four years,

as part of the QUANTIF fund.

My friends outside of uni played a vital role in not letting me go crazy so many thanks to all my hundreds of housemates from Acorn House, I have learnt something from all of you, even if it was only how live with basically anyone. I hope you all keep being awesome and that the Acornmas tradition continues. I am grateful to all members of the Kali-JKD society and of course our exceptional instructor, Lucky, for some fantastic years of effective stress relief and good fun. In the last few difficult months, my thanks go to the people who were around and looking out for me, Paul Long and Miri Volger, in particular. Special thanks go to Helen Cockerton and Philip Carter, I hope our friendship lasts however far apart we end up and, of course, to my dear friend, Rehab Al Botros, whose amazing courage in the face of adversity has given me so much strength and perspective in my own troubles.

Most importantly, I am grateful to my interesting family who have been a never ending supply of support and humour. Thanks to my brother Tim, especially for LaTeX advise, my sisters Amy and Hayley, my dogs Rocky, Sally, Jack and Ollie and my parents Michael and Natalie. Lastly, so much thanks to my partner, Adam, whose love and support has been truly remarkable.

I relied heavily on the Inkscape program, so I would like thank all the developers that made such a great program for free use. This thesis was typeset with LaTeX 2_ε[1] by the author.

[1] LaTeX 2_ε is an extension of LaTeX. LaTeX is a collection of macros for TeX. TeX is a trademark of the American Mathematical Society. The style package *warwickthesis* was used.

Declarations

This thesis is submitted to the University of Warwick in support of my application for the degree of Doctor of Philosophy. It has been composed by myself with the exception of the list below and has not been submitted in any previous application for any degree.

Chapter 3: The majority of the WEC-SPM project code was written by Dr. Kim McKelvey.

Chapter 4: All FEM data was obtained by models from Dr. Michael Snowden and Dr. Kim McKelvey. The work discussed in this chapter has been published: Sophie L. Kinnear, Kim McKelvey, Michael E. Snowden, Massimo Peruffo, Alex W. Colburn and Patrick R. Unwin, *Langmuir*, 29, 15565

Chapter 5: All data from FEM models and CrystalMaker was obtained by Rehab Al Botros. Dr. Monica Ciomaga Hatnean performed all Laue X-ray crystallography used in this chapter.

Chapter 6: All data from FEM models was obtained by Kim McKelvey. The work discussed in this chapter has been published: Kim McKelvey, Sophie L. Kinnear, David Perry, Dmitry Momotenko and Patrick Unwin, *J. Am. Chem. Soc* 136, 13735

Chapter 7: Experimental work was halved between myself and Ashley Page.

Abstract

This thesis is concerned with the construction of new electrochemical scanning probe microscopes. Designed to support a wide variety of existing techniques as well as to develop new techniques. This flexibility was achieved by basing the equipment around a field programmable gate array card (FPGA), which allows for a software program to be configured on the physical FPGA card as hardware. This technology provides the efficiency and high speed of bespoke hardware and can be reprogrammed like software. The instrumentation was programmed in-house using the graphical programming language, LabVIEW, which allowed for changes and upgrades to be made when necessary. Two branches of projects were studied with the FPGA instrumentation, crystal dissolution and surface charge mapping. For the crystal dissolution studies, dual-barrel conductance micropipettes were used to investigate the dissolution of NaCl and calcite, with microscale spacial resolution. This technique had many advantages over traditional methods. For instance, high temporal resolution in the order of sub-milliseconds was achieved through the employment of in-house built current followers. In addition, fast mass transport inside the pipette allowed the study of surface kinetic processes. The implementation of finite element method simulations complemented the experimental findings, by enabling the quantitative analysis of the data to extract intrinsic dissolution rate constants. The technique is also complemented by atomic force microscopy, which provides an alternative method for analysing the etch pits. The same equipment is used as a scanning ion conductance microscope (SICM) to investigate the surface charge of both conductive and non-conductive surfaces. A double electric layer forms at the solid-liquid interface of a sample that is immersed in electrolyte solution, at low ionic strength the thickness of the double layer increases, which enables its detection via the SICM pipette. The formation of the double layer at the pipette walls induces ion current rectification, at the same time a surface induced rectification arises as the nanopipette approaches the substrate surface. The combination of these results in the creation of an ion perm-selective region, which results in an increase or decrease in current that is proportional to surface charge. Point measurements, maps and CVs of dynamically changing surfaces have been recorded.

Chapter 1

Introduction

> "The famous pipe. How people reproached me for it! And yet, could you stuff my pipe? No, it's just a representation, is it not? So if I had written on my picture 'This is a pipe', I'd have been lying!"

Rene Magritte

This thesis is concerned with developing techniques to study the properties and nature of solid-liquid interfaces. Two branches of this topic are considered: (1) ionic crystal dissolution prompted by an undersaturated solution, and (2) mapping of the surface charge of both inert and dynamically changing substrates. The new techniques were developed on instrumentation consisting largely of in-house constructed hardware and completely in-house developed software. A major component of the studies herein involve developing sophisticated instrument control and data acquisition routines. Building everything in-house allowed changes to be made to the instruments without the constraints of proprietary hardware and software.

1.1 An Overview of Surface Science and Electrochemistry

Surface (or interfacial) science, very broadly, is the study of reactions and phenomena at the interface between two phases. These phases can be a liquid-gas interface, like the exchange of CO_2 in air to HCO_3^- in an aqueous solution due to the accompanying chemical reaction, a liquid-liquid layer of two immiscible fluids or, as will be the focus of this body of work, a solid in contact with a solution. Surface science also defines a large field where well-defined single crystals of metals or semiconductors are studied in ultra high vacuum. Common examples for surfaces that might be studied include an electrode with an externally applied potential in contact with a salt solution or a crystal immersed in an undersaturated solution prompting dissolution. Although the work herein does not have a focus on the more common use of electrochemistry, namely redox reactions, understanding the kinetics and behaviour of species under a potential field and at electrode surfaces is of paramount importance and is dealt with in this thesis.

An appropriate starting point when discussing electrochemistry is to explain the two and three electrode setups and the function of reference electrodes in both. Reference electrodes are electrodes that are capable of being held at a constant potential that does not drift with time. This is normally achieved by employing a redox couple, in which the solid electrode of one half of the reaction is in contact with a constant concentration of saturated solution containing the other half of the redox couple. The standard hydrogen electrode (SHE) has been used as the basis for comparing any half cell. The SHE is given a half cell potential of 0.000 V, at any temperature and other half cells are calculated compared to the SHE. The half cell equation for the SHE is

$$2\,H^+_{(aq)} + 2\,e^- \rightleftharpoons H_{2(g)} \tag{1.1}$$

However, the SHE is not convenient for experiments as it requires a platinum electrode and a constant source of hydrogen gas, as shown in Figure 1.1(A). One of the more commonly used reference electrode in practical experiments is

the Ag|AgCl reference electrode. The equilibrium reaction proceeds as follows:

$$\mathrm{AgCl_{(s)} + e^- \rightleftharpoons Ag_{(s)} + Cl^-_{(aq)}} \tag{1.2}$$

and is achieved physically by chlorodizing the outside of a silver wire then sealing the wire in a tube filled with Cl^- saturated solution, such as KCl. There is a metal connector through the top of the tube so the electrode can be connected to a circuit and a frit at the bottom of the tube so current can be passed into the saturated solution from the bulk solution without contamination in either direction. (See Figure 1.1(B)) The electrode pictured is of a standard size, although they can be slightly smaller they are still large, bulky and fragile and not suitable for incorporation into scanning microscope probes or flow cells which restricts their usage to bulk measurements. When smaller, thinner electrodes are needed a quasi-reference counter electrodes (QRCE) can be used. These electrodes are reasonable stable, but do not have the constant equilibrium that reference electrodes do. They can be made from a thin metal wire often simply platinum or silver. To fabricate a QRCE similar to the Ag|AgCl electrode the same process is applied to chlorodize the silver wire, but then the wire is washed in water and used without being in contact with a saturated solution, directly into the solution of interest.[1] If this contains a reasonable Cl^- concentration the potential is fixed.[2]

With a stable reference electrode, a two electrode system can be constructed by adding a working electrode and applying a constant potential with respect to the reference electrode. However, if a large current is applied to a reference electrode (µA or higher) it will start to oxidise or reduce in excess and drift away from its equilibrium, changing the effective bias of the system compared to the bias applied. Therefore only currents in the nA range should be passed though a two electrode setup. For systems that pass larger currents, a three electrode setup is required. Here a third, 'counter', electrode collects the current, while the reference electrode can still be used against which to apply a constant bias. Counter electrodes are commonly a platinum wire or mesh with a surface area far in excess of that of the working electrode in order to ensure the complete collection of current in the system.

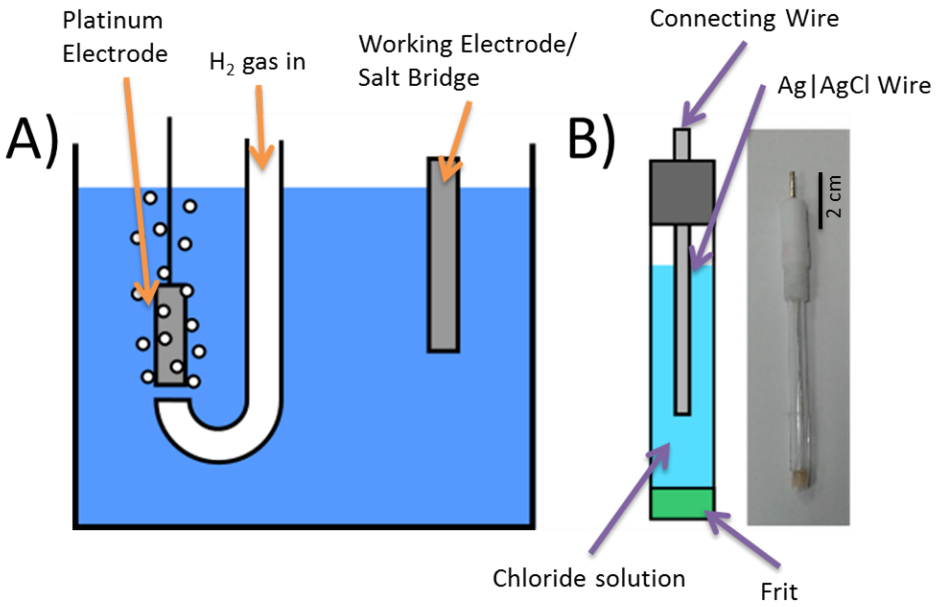

Figure 1.1: Schematic of both A) standard hydrogen electrode and B) Ag|AgCl electrode. Also shown in (B): a photo of a Ag|AgCl electrode.

A staple of electrochemical research is linear sweep and cyclic voltammetry (LSV and CV). This is an experiment which sweeps the potential of either the working or reference electrode and the resulting change in current is measured, linear sweep voltammetry sweeps the voltage in just one direction. In the more commonly used cyclic voltammetry the potential is swept back and forth for any number of cycles. The uses of CV include, but aren't limited to: observing the overpotential of redox reactions,[3] reversibility of those reactions,[4] calculating charge density, observing capacitance,[5,6] and ion current rectification[7] and various electrode cleaning procedures.[8]

1.2 Scanning Probe Microscopy

Scanning probe microscopy (SPM) is an umbrella term for any microscopy technique that employs a positionable, physical probe to collect data which can then be interpreted as a physical property of the surface, such as sample height, or chemical reactivity.[9] SPMs have revolutionised how we study surfaces and interfaces and has opened up the field of nanotechnology. Importantly, what

the probe collects is only a dependent variable of what is to be measured. Rather like the affect of aberrations and minimum wavelengths have on optical and electron microscopy, SPM must consider the morphology of the probe used and its potential affect on the data recorded.

1.2.1 Atomic Force Microscopy

Atomic force microscopy (AFM) is one of the older forms of SPM. This technique came directly after scanning tunnelling microscopy (STM)[10] and was a breakthrough for imaging as AFM was capable of scanning non-conductive surfaces, unlike STM. First developed in the mid 1980s by Binnig *et al*,[11] the technique employs an extremely sharp tip, on the end of a horizontal cantilever, which is brought into contact with a surface and then the movement of the cantilever bending against the surface can be used to map topography. The cantilever is reflective and a laser is aligned precisely onto the back in order to reflect onto a detector. When the tip is pulled onto a substrate, due to inter-atomic forces, the cantilever bends, as shown in Figure 1.2(A). The detector records the movement of the laser as the cantilever bends due to the topography of the sample that the tip is scanning. This deflection is converted to height and a topography map is recorded. The activity of inter-atomic forces can be seen in the force curves. A schematic of an approach and retract of an AFM tip to a surface is shown in Figure 1.2(B).

The generic shape of a force curve shows the tip coming into contact suddenly as the inter-atomic forces pull the tip down. The retract will not mimic the approach, as the tip can become stuck to the surface by atomic force, and the adhesion of the tip on the surface has to be overcome.

The simplest mode of operation is named 'contact mode' or 'constant force'. In this mode once the tip has made contact with the surface it is then dragged in a raster scan pattern while being in contact with the surface. Contact mode is fast, simple and effective, but comes at a cost. The tip and sample are in constant physical contact and if the sample is harder than the tip, the end of the tip wears down over time and becomes flatter, reducing XY resolution. If the sample is softer than the tip, or has micro- or nanoscale

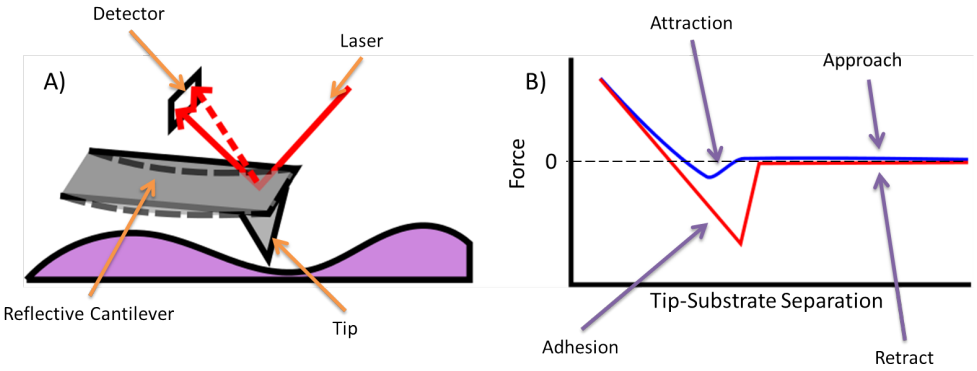

Figure 1.2: A) Schematic of the AFM tip as it makes contact with a surface, bends the cantilever and deflects the laser. B) Sketch of a force curve showing the approach (blue line) and retract (red line) of an AFM tip.

objects not sufficiently attached, the tip can damage the surface or drag objects on the surface around, for example polymer fibres unsecured to a surface.[12]

There is an alternative method called 'tapping mode' which alleviates these problems to a certain extent. In tapping mode the probe still makes physical contact with the surface but only intermittently. An oscillation is applied at or near the cantilever's resonant frequency, and the amplitude is monitored. Many different tip sizes and shapes have been developed and the resonant frequencies range between 1 kHz to 1 MHz. When the tip nears the surface, the amplitude experiences dampening, which can be used as feedback to indicate the tip has reached the surface. Although this method has longer scan times than contact mode due to the slow movement of the tip towards and away from the sample, an advantage is that a force curve can be recorded at each point. Force curves can provide a large volume of different information on the physical properties of the sample.[13] Figure 1.2(B) shows a generic force curve, in reality the gradient of the attraction, and the height of the pull-off force and the distance from the surface at which these events take place can all be used to inform on a range of different surface properties. These include, but are not limited to, surface hardness,[14,15] adhesion,[16,17] friction,[18] and elasticity.[19]

Due to the range of modes and tips that AFM provides, and the range of sample that can be scanned, AFM is used across all the sciences, with wide

use as a characterisation technique. Efforts have been made to expand the functionality of AFM. Chemical sensitivity can be added to AFM experiments by chemically modifying the end of the tip.[20] Conductive AFM (C-AFM) employs a metal coated tip which, during a scan, passes a current between the tip and sample under an applied bias, so that a topography and conductivity map are recorded simultaneously.[21] Studies on molecular wires have used C-AFM to look at conductive molecules within nonconductive self-assembled monolayers (SAM).[22] Crystal dissolution studies with direct relevance to the concerns of this thesis will be discussed in Section 1.4.3.

1.2.2 Scanning Electrochemical Microscopy

Scanning electrochemical microscopy (SECM) was first developed by Bard *et al* in the late 1980s.[23] Employing an ultramicroelectrode (UME) as a probe to investigate the electrochemistry of surfaces, and for the first time a scanning probe could be used to probe specific chemicals.[24] To create microscale electrodes two methods are predominately used. The first method is to etch a metal wire down to a conical tip and then insulate the wire excluding the end of the cone. A number of different coatings have been investigated including silica coatings and various polymers.[25] Even sub-micron probes have been reported with this method.[26] However, these conical probes proved not to have the desired level of reproducibility. The second method creates a disk electrode by starting with a wire of the diameter required for the finished electrode and sealing it in glass using a laser puller to stretch out a capillary.[27] Standard sizes are tens of microns, commonly 25 µm[28,29] but nano sized probes have been created,[30] with probes as small as ∼20 nm now being reported.[31,32] The advantages of this method are reliability, reproducibility and these electrodes can be polished repeatedly to a flat, clean surface without changing the diameter of the electrode. This method is used for work in this thesis and more information on their fabrication can be found in Section 2.2.2. The major drawback is that the electrode is surrounded by glass, with a diameter much larger than the electrode. This must be taken into account when calculating the spatial resolution. The ratio of electrode diameter to that of the surrounding glass, known as RG, must be known and accounted for when

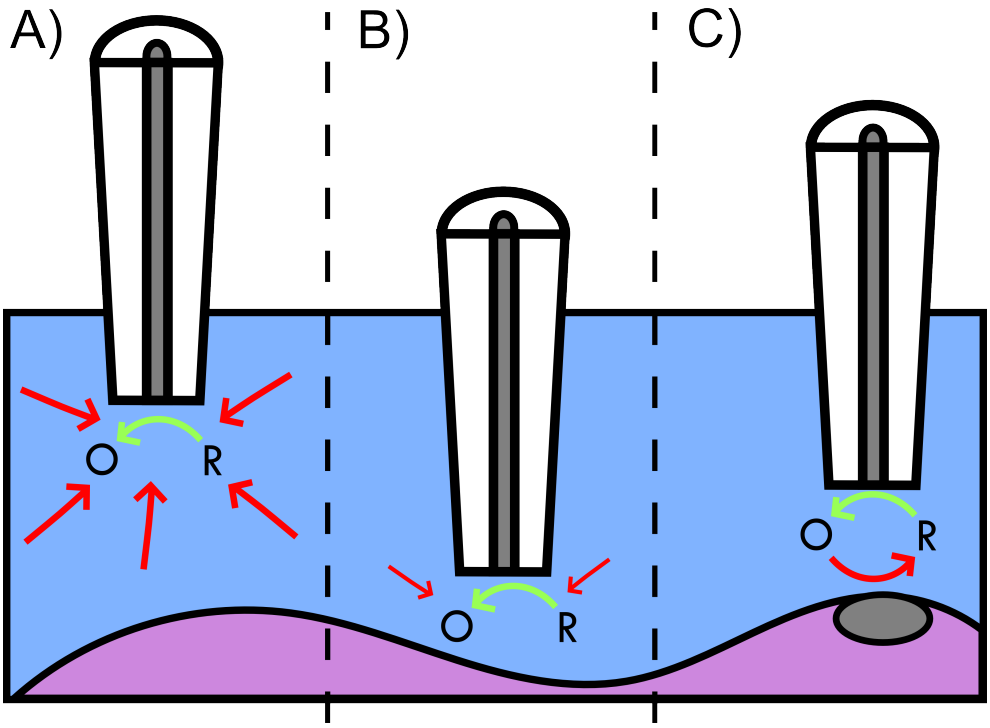

Figure 1.3: A) The UME in bulk, slowly turning over reactant. B) When approached to an insulating surface mass transport to the UME is decreased, and therefore a lower current is recorded at the UME. C) Approaching to a conductive surface will result in a higher current as the product of the reaction is renewed.

analysing data and when designing simulations to mimic an SECM system. Some applications of SECM include studying the hydrogen evolution reaction (HER) for use in fuel cells,[33] patterning nanostructures,[34] and probing fluxes through materials such as human dentine,[35] and nanopores.[36] SECM has also been used to study crystal dissolution, which will be discussed in Section 1.4.3.

Modes of Operation

Upon invention, the technique immediately presented a number of different scanning modes.[37] The most simple is the feedback mode. As shown in Figure 1.3(A), in the bulk solution a potential can be applied to the UME which will oxidise or reduce the redox mediator in the solution, usually at a diffusion controlled rate. If approached to an insulating surface the mass transport to

the UME is blocked and the recorded current at the UME will drop (Figure 1.3(B)). Conversely, approaching to a conductive surface will increase the current, because the surface will regenerate the reactant (Figure 1.3(C)).

Another mode is known as tip generation - substrate collection (TG-SC).[38,39] A steady, quantifiable stream of reactant is generated at the probe and is collected at the substrate with up to 100% collection efficiency. This makes TG-SC excellent for experiments such as screening for oxygen reduction reaction catalysts,[40] among many other applications. Microarrays of different alloys can be quickly fabricated and compared in a single experiment. Hydrogen oxidation has been studied in much the same way on a selection of noble metal electrodes.[41] In some cases it is the reaction at the surface itself that is in question and so substrate generation-tip collection (SG-TC) can be used. SG-TC has been employed to study diffusion coefficients,[42] and oxygen reduction reaction mechanisms.[43]

Both of these techniques can be used only on conductive substrates, and they lack the ability to simultaneously measure topography. A solution to these problems is AC feedback mode. There are a variety of modes under the umbrella term 'AC experiment'. They can be divided into two main categories: piezo oscillation and bias oscillation. In piezo oscillation mode, an AC signal is added to the physical movement of the probe, also known as 'shear force' mode, one piezo is oscillated and another measures the dampening of this oscillation as the probe reaches the surface.[44,45] This mode requires new hardware so is complicated to retrofit. A simpler, easier method is intermittent contact SECM (IC-SECM), where only one additional piezo is required, named a 'soft' or 'bender' piezo, where the probe is gently tapped against the surface. IC-SECM takes advantage of the imperfect alignment of the SECM probe and the surface. When the closest edge of the probe touches the surface the AC signal from the bender piezo will be dampened but the probe will still register a current as the probe is often slightly titled with respect to the surface. Bias oscillation mode applies an AC signal to the potential applied to the system, as the tip approaches a surface the current pathway begins to be blocked, creating a height dependence in the DC signal which is registered by the AC

signal.[46,47] This mode has been used for a range of applications including studying corrosion[48] and imaging living cells.[49,50]

Combined Scanning Electrochemical Microscopy and Atomic Force Microscopy

To further enhance the capabilities of SECM, work has been done to couple UMEs with other probes, the most common are SICM, which will be discussed in Section 1.2.3, and AFM. The combination of AFM and SECM provides chemical sensitivity and excellent topography capability in a single probe.[51,52] Tip creation began as a complicated process that made one probe at a time sealed in a polymer[51] or glass.[53] In more recent years advances in microfabrication has allowed batches of tips to be produced, utilising focused ion beam (FIB) milling.[54,55] Tips tend to be one of two forms: conductive apex or recessed electrode. The former are created by modifying conventional AFM tips. The tip is coated with a conductive layer and then an insulating layer, with the conductive tip re-exposed from the insulating layer, either mechanically or using FIB. Tips have been fabricated from conductive materials such as platinum,[56] boron doped diamond (BDD) or gold.[57]

Because AFM tips make physical contact with the surface there is a great risk that the electrode will be damaged during a scan, which may make conductive apex tips inherently fragile. Recessed electrode style tips were designed to avoid this problem by having the SECM electrode set back, slightly above the AFM tip. A number of fabrication methods exists including FIB milling an AFM tip onto the end of an epoxy covered UME,[58] or FIB etched out of BDD.[59,60] This combined technique can be used for a great many different topics, from inorganic problems such as corrosion[58,61] to answering biological questions about the activity of living cells.[62,63]

1.2.3 Scanning Ion Conductance Microscopy

From its inception[64] to the present day scanning ion conductance microscopy (SICM) has been used almost solely for topographical imaging. In essence, SICM works by measuring the ionic conductance between a QRCE in bulk solution and an electrode enclosed in a single barrelled pipette. The probe is

approached towards a surface of interest and, as the probe reaches approximately 1 tip diameter away from the surface, the currents starts to decrease as the surface starts to obstruct the solution from entering to probe, which increases the resistance in the circuit. This drop in current is detected and is used as feedback to scan laterally across a surface to measure topography. This technique has also been used to measure the release of ions from a substrate containing pore features.[65,66] A schematic diagram of the most basic SICM setup is shown in Figure 1.4(A). Relying solely on the DC ion current as a method of feedback can be unwise, as many factors can impact the DC current such as local or general changes in ionic strength, particulate matter blocking the pipette or drift of the current.[67]

For more reliable feedback the probe is oscillated in the Z direction. When close to the sample surface, the resulting AC current can be used as feedback. The AC magnitude is essentially the gradient of the DC-distance curve. Thus, in bulk solution there is no variation in DC current and the AC value will be minimal. The differences are shown in Figure 1.4(C and D) where C shows the DC current decreasing with height, while the gradient of that decrease increases so too does the magnitude of the AC current. Once the probe begins to reach the surface the DC current will change with the oscillating position of the probe. This will induce an AC current of the same frequency as the applied Z oscillation, which can be detected by a lockin amplifier (the function of which will be discussed further in Section 2.4.3).

As well as these two modes of approach, SICM also has two main modes of scanning. Constant distance mode, analogous to contact mode in AFM, rasters the probe close to the surface, at a constant separation, while the Z piezo moves to try and maintain a constant value for either DC or AC.[68] Hopping mode, approaches the probe to a given setpoint then retracts the probe into the bulk before moving laterally and approaching the surface again.[69]

Applications of SICM

One of the main advantages of SICM over other imaging techniques is that experiments can be performed in environments amenable to living biological

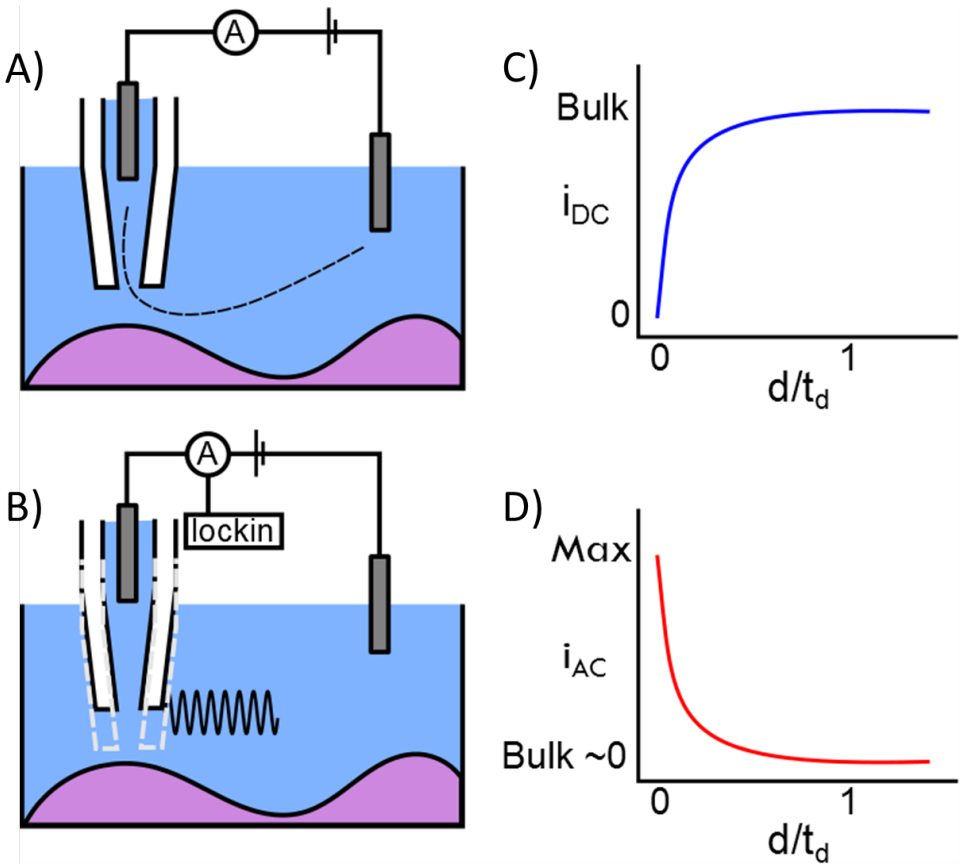

Figure 1.4: Schematic of SICM setup for both A) DC feedback and B) AC feedback. C) DC approach curve showing the drop in current as the probe approaches the surface, due to the surface restricting ion flow. D) AC approach curve increases as the DC current becomes dependent on height.

samples.[70] This has led to a much greater understanding of cells *in-vitro* and has been used to image cells in a wide variety of projects, such as proteins in living cell membranes,[71] cell volume measurement,[72] and leaf surface morphology.[73] An additional advantage is that the probe does not make physical contact with the sample, unlike AFM that has been proven to deform cells as they are being scanned.[73,74]

If not used for imaging, the SICM can be used to measure ions delivered through channels. For biological systems this is achieved by inserting a patch clamp micropipette into the cell in order to drive ions through the cells channels,[75] and can be coupled with confocal laser spectroscopy.[76]

Combined Scanning Electrochemical - Scanning Ion Conductance Microscopy

With a number of incredible high resolution techniques for measuring topography of both conductive and non-conductive substrates now available, a push has been made toward functional imaging. Maps of surfaces that can inform on surface properties and activity rather than just topography. SECM, as a stand alone technique, can achieve this, but at the expense of accurate topography. When the two techniques are combined into one dual-function probe, both topography and reactivity can be mapped simultaneously. SICM-SECM has a number of advantages over AFM-SECM, namely, probes can be based on glass capillaries making them cheap and easy to produce.

There are a number of ways to fabricate SECM-SICM probes, each with a different geometry. Starting with a regular SICM probe, an SECM electrode can be added to the side by evaporation of an electrode material such as gold.[77] More commonly a dual-barrel pipette is used and an electrode is fabricated in the barrel for SECM by pumping butane gas down the wide end of the probe and heating the tip. The butane forms a carbon electrode at the tip of the SECM barrel.[78,79] To prevent the SICM barrel becoming blocked with carbon it is temporarily blocked from the wide end and an inert gas is pumped towards the tip end to prevent the butane from the SECM barrel escaping and ensuring it is burnt to form carbon. The downside of this technique is that the carbon can be recessed far back down the barrel and the exact distance of the recession is not reproducible. The best probes have to be flattened using FIB milling.[80]

Both SICM and SECM are non-contact techniques, which means the probes do not risk damaging the sample or becoming damaged themselves during regular use. Although SECM-SICM is a relativity new technique, studies have proven the techniques ability in SG-TC SECM mode,[77] and it has been used to investigate live cells[81] and transport of species through pores and ion channels.[82] The probes can be functionalized further and there have been reports of successfully depositing platinum on the carbon tip to sensitize the electrode.[83] Iridium oxide can be deposited on the carbon in order to create a pH probe, which has been used to measure the changing topography and local pH around a calcite crystal while it is dissolving.[84]

1.2.4 Scanning Electrochemical Cell Microscopy

The technique of scanning electrochemical cell microscopy (SECCM) is very young but is finding many areas in which its abilities can be of considerable advantage. SECCM, like SICM, use cheap disposable probes created from glass or quartz capillaries pulled to a sharp tip in a commercial laser puller. However, SECCM uses capillaries with a vertical wall, known as the septum, down the middle. These are referred to as 'theta capillaries'.

SECCM Setup

When theta capillaries are pulled in a laser puller, the septum is stretched and thinned as well, producing a sharp tip with two micro, or nano, scale barrels. (Figure 1.5(1)). Both barrels are then filled with an electrolyte solution appropriate for a given application (Figure 1.5(3)). This can be anything from aqueous solutions[85] to organics and even ionic liquids[86] and there can be a different solution in each barrel.[87] The solutions in both barrels meet at the tip of the probe and protrude from it in the form of a liquid meniscus, this meniscus forms a connection between the two barrels. A QRCE is then added to each barrel, the material of which can vary depending on the solution. However most commonly a Ag|AgCl wire can be used, (Figure 1.5(4)). When electrical contact is made to the QRCEs, an electrochemical cell is formed (Figure 1.5(6)). The ionic current of this micro cell is dependent on the most resistive section of the circuit, which for the SECCM setup is always the liquid meniscus connecting the barrels. The state of the meniscus can be elucidated from the ion current in the cell. For instance to land the SECCM probe on a surface, the probe is moved vertically downwards until the meniscus contacts the surface. A sudden increase in ion current results from the meniscus dimensions expanding and the resistance in the meniscus dropping. This can be detected and the vertical movement stopped in response before the physical tip touches the surface. 3D scanning over conductive and non-conductive surfaces is possible (Figure 1.5(7,10)).

It should be noted that the electrical circuit shown in Figure 1.5 is an example of a common setup. Many different studies have been conducted

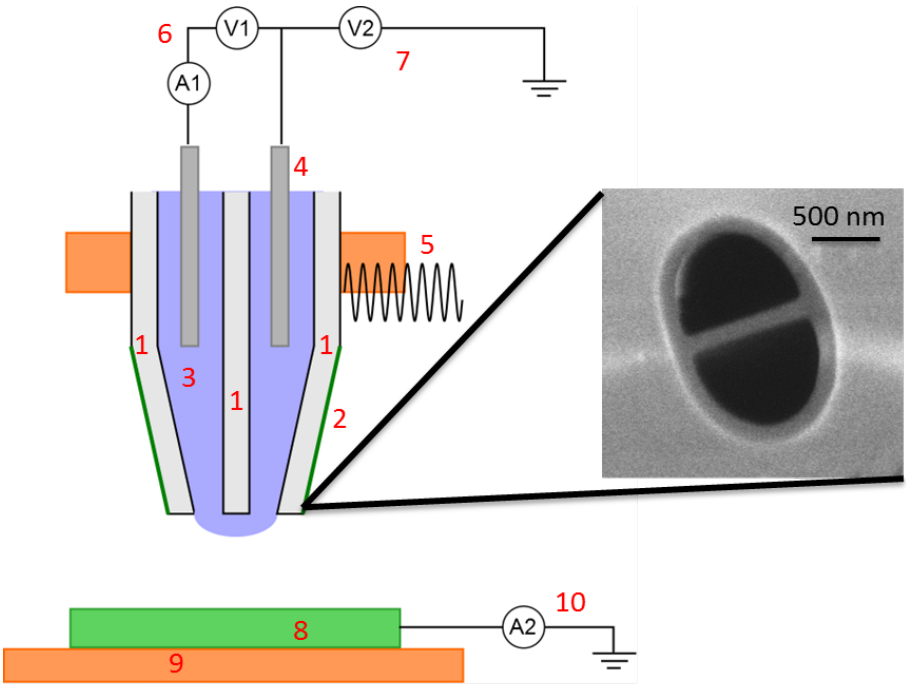

Figure 1.5: Schematic diagram of the dual barrelled conductance micropipette. 1. Capillary with septum pulled to a sharp point. 2. Silanised outer walls to prevent liquid meniscus from spreading. 3. Electrolyte solution inside both barrels. 4. A QRCE in both barrels. 5. The Z piezo to move the probe towards the surface. An oscillation is applied to the overall movement. 6. Circuitry to hold a potential between the barrels and record the current. 7. Optional second potential to offset the probe from the surface for conductive samples. 8. Sample, held in custom sample holder. 9. XY Piezo for lateral movement. 10. Optional current follower for conductive samples. Also shown: an SEM image of the tip of a probe.

using SECCM and most will have a similar setup.[88,89] For experiments on non-conductive samples, a simplified version may be used in which only one potential is required, applied directly to the QRCE in one barrel, and a current follower is connected to the other QRCE.

Among the advantages of SECCM is that the meniscus from the probe can be landed on a surface without the surface needing to be submerged in an electrolyte solution. The spatial resolution of the technique is dependent on both the size of the probe opening and the wetability of the surface. The more hydrophilic a surface, the more an aqueous meniscus will spread, for example. However, in general a rule of thumb is that the meniscus wetting area is of the order of the probe size.[90,91] Depending on application the tip of the probe can be silanised on the outside,[90] this ensures that when the tip is filled with solution the meniscus does not leak onto the outside of the probe (Figure 1.5(2)).

Landing the probe can be achieved with DC current feedback only, but in many cases the sensitivity and variability of the DC current means that a more sophisticated mode of approach is required. The most common mode of SECCM is distance modulation (DM), working under the same principles as AC-SICM, in which the probe is oscillated in the Z direction (Figure 1.5(5)). While in air the AC component of the barrel current is close to zero and does not change (similar to SICM). Once the meniscus makes contact with the sample the physical Z oscillation causes the meniscus to squash and stretch, therefore causing the ionic resistance in the meniscus to change and this gives rise to a detectable AC signal. This method is highly reproducible and reliable. In addition, the SECCM probe can be modelled with a high degree of detail in computer simulations.[90] This allows data from most experiments to be matched to simulated values.

Application of SECCM

SECCM was used to image evaporated gold bands on glass, and proved the high spatial resolution attainable compared to SECM.[85] In DM mode the probe is translated laterally across a surface and the height is adjusted to match

a given AC setpoint, representative of a fixed distance away from the surface. A redox mediator was present in the barrels so when the probe was over gold an electrochemical current was detected which did not interfere with the topography measurement as the redox current was orders of magnitude smaller than the ionic current. Then when the probe is over glass no electrochemical current is recorded. In this manner two maps were plotted: topography and electroactivity.

The high spacial resolution has been used to answer important questions about heterogeneity in the surface electrochemistry. Highly orientated pyrolytic graphite (HOPG) has often been used as a model for other carbon based materials, such as graphene.[92] From macroscopic measurements it was believed that only the step edges were active and were responsible for the entire electrochemical activity of HOPG. With the SECCM the surface could be mapped with spacial resolution high enough to distinguish these features and the results showed the basal plane had near-reversible electron transfer kinetics.[93] The same principle was later applied to multilayer graphene, which allowed the differences between basal and step edges to be seen, as well as the differences between areas of different numbers of layers.[94]

Another advantage of SECCM is the high mass transport in the meniscus. Due to this it has been possible to probe nanoscale structures for their surface kinetics with redox mediators. The electrochemical reactivity of single walled carbon nanotubes (SWNT) has been studied,[95] and in conjunction with a finite element method (FEM) model proved to be reasonably uniformly active along their entire length. Single particle resolution has been achieved with this system.[96] Platinum nanoparticles can be grown on pristine SWNT template and each can be scanned for both size and chemical reactivity. The particles can then be investigated with SEM to provide an even greater understanding of their morphology and therefore how the size and shape of individual particles affects their reactivity.

The SECCM has already been used for patterning of various materials.[87,97] Conductive wires with a diameter matching that of the probe can be fabricated from the electropolymerisation of monomers. This can be done while the probe is moving to form wires. So long as the wire starts on the con-

ductive surface it can be grown out onto an insulating surface. 3D structures can be constructed by moving the probe vertically.[97] Poly-L-Lysine (PLL) patterns have been deposited in order to create a sample analogous to living cells.[98]

Impressively, one study used two different solution in the barrel to deliver, in a predetermined pattern, three colours, and therefore create an image.[87] DNA will adhere to positivity charged surfaces so streptavidin coated glass was used as a substrate. In single colour tests it was observed that florescence material would only deposit from one barrel, the barrel of matching charge that would push the material out. By reversing the potential it was possible to flip the direction in which the material was deposited. Varying the driving force of the potential deposits different amounts of material, resulting in a graded colour. Two materials can be patterned simultaneously by changing the sign of the applied potential to drive the chosen species out. Green was deposited from rhodamine green labelled DNA and red from alexa 647-labeled DNA. Yellow can also be seen in locations where both species were deposited. In this fashion entire pieces of artwork can then be copied.

In the previous year more advancements have been made to the technique. In order to collect more information about a surface, SECCM is being used in hopping mode and a CV run at each hop. To run several scans at fixed potential is highly time consuming, and only gives a small voltage resolution. Running a CV at every hop means that each pixel will have a voltage resolution limited only by the chosen data collection rate (hardware limits will typically be higher, on the order of tens of microseconds). The clearest way to show this high volume of data is to create a movie where each frame is the entire map at a single voltage. This produces a movie with hundreds of frames, showing the entire map as the voltage is swept, making it easy to see the affect of surface heterogeneity on reactivity.

The work of Chen *et al*[99] shows this technique applied to the study of hydrazine oxidation at platinum electrodes. In the movies created from this technique, it was possible to see the quantifiable differences in reactivity of the different faces making up a polycrystalline platinum electrode. The faces

in the mapped region were correlated to their grain orientation by combining SECCM images with electron backscatter diffraction (EBSD) data.

1.3 Ionic Crystals and Crystal Dissolution

Crystals, at their most basic, can be described as a solid composed of a regular, repeating arrangement of atoms or molecules. The study of crystal dissolution is of high importance in many areas of nature science, such as geology and the carbon cycle,[100,101] but also has huge importance in industries affecting peoples everyday lives such as in oral drug delivery[102,103] to food[104] and construction.[105] Consequently, methods for studying crystal dissolution are equally important, with a need for reliable techniques that can provide quantitative information on the kinetics and mechanisms.

1.3.1 Mechanisms for Crystal Dissolution

Dissolution is governed by two competing processes, mass transport and surface phenomena,[106] as shown in Figure 1.6. These processes occur in series so, when measuring dissolution rates, only the rate limiting step, the slower of the two, can be observed. The former is the movement of material from the interfacial region to the bulk solution, this occurs in three separate ways:

1. Convection, very generally, is defined as the physical movement of a fluid. This can be from natural causes, such as temperature gradients or density differences resulting from a reaction. Examples of artifcial introduced convection include the movement of solution under a mechanical force, such as stirring, or a flow cell. Convection can be purposefully added in the form of a rotating disk or flow cell in order to overwhelm the contribution from natural convection with a highly controlled and defined form, Increasing convection is also used to increase the overall mass transport rate, in order to access surface kinetics of some crystal systems. However, convection is usually discounted from experiments by keeping the solution still and at constant temperature or conducting each experiment on a short time scale.

2. Diffusion is the motion of particles along a concentration gradient, acting to homogenize the solution. Fick mathematically described diffusion

as a function of diffusional flux (j), defined as the moles of material diffusing through a unit area in one second, this is Fick's first law of diffusion.

$$j = -D_B \frac{\delta[B]}{\delta x} \tag{1.3}$$

where [B] is the concentration of diffusing species B and D_B is the diffusion coefficient for B. Each species has a constant diffusion coefficient. A more useful form of this equation gives the change of concentration of B at a point in space. This is Fick's second law and is used to describe the diffusion component in the time dependent 3D FEM models used in this thesis.[107]

$$\frac{\partial[B]}{\partial t} = D_B \left(\frac{\partial^2[B]}{\partial x^2} \right) \tag{1.4}$$

Diffusion is highly important to understand and quantify as it cannot be removed under experimental conditions.

3. Migration, which is movement of ions under an applied potential, is worth discussion here despite most crystal dissolution studies not requiring a potential to be applied. However, some techniques, such as channel flow cells and SECM are dependent upon the use of electrodes for detection or control and therefore migration must be considered. In this thesis, crystal dissolution is not dependent on an electrochemical reaction, however, an electric field is still present and is described as migratory flux, j_m

$$j_m \propto -u[B] \frac{\partial \phi}{\partial x} \tag{1.5}$$

where ϕ is the applied potential and u is the ion mobility.[108] Ion mobility is dependent not only on the characteristics of the ion but also on the solution. H^+ moving in aqueous solution has a mobility of $3.62 \times 10^{-7} \mathrm{m^2\,s^{-1}\,V^{-1}}$ at 298 K,[109] and can move under the Grotthuss mechanism, in which rather than a single pacticle moving, a proton will attach to a water molecule and force another off, then that one forces a proton from a second water molecule in a 'bucket chain' style.[110] However, most ions have a mobility on the order of $10^{-}8$.[111] Migration carries the ion current through the bulk solution, however, at the surface of electrodes the double layer can form and interfere with elec-

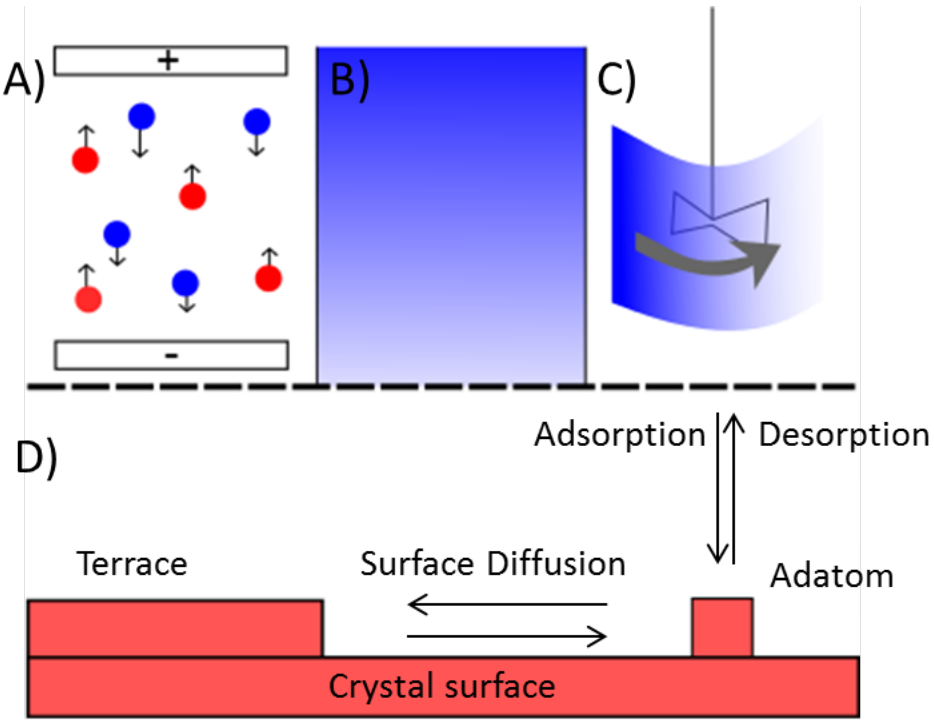

Figure 1.6: Diagram of mass transport processes: A) Migration, particles moving under the influence of an electric field B) Diffusion, particles moving down a concentration gradient C) Convection, particles moving under the influence of an external force, in this case stirring. D) Surface processes: surface diffusion and adsorption/desorption.

tron transfer. In the large majority of cases migration can be neglected by increasing the ionic strength of the solution used.

Surface phenomena includes processes such as surface diffusion and the detachment of ions or molecules at the crystal surface, this detachment or movement of ions on a surface is often treated as following the terrace ledge kink model[112]. This model provides the basis to consider the processes of adatoms desorbing, surface vacancies forming and step edges retreating. The relative thermodynamic probability of each of these processes will then vary between crystal systems.

If one is interested in surface kinetics, the experimental setup must be capable of making mass transport sufficiently high and well-defined to enable

the kinetics of the surface processes to be measured. Additionally, due to the dependence of surface process rates on the surface morphology, different sites on the same crystal surface may have different dissolution characteristics.[113] This means the most informative studies are those which have a means of controlling and defining the surface in question.

1.3.2 Defects in Crystal Structure

There is a considerable body of work on the topic of dissolution from dislocations and defects, which can seriously alter and also control dissolution in crystals.[114] Many types of defect exist, such as point defects, dislocations, stacking faults and grain boundaries.[115,116] Point defects are single atom defects arising from breaks in a crystalline materials crystal structure, such as a missing atom or the wrong atom. Dislocations and stacking faults are more substantial defects which cause large section of a crystal to shift away from the crystalline structure. Grain boundaries tend to be formed when the many faces of the crystal are crystallising at the same time, when the faces grow towards each other they form a rough edge where they meet. A full awareness of the affect of defects in crystal structures is vital to understanding more complex dissolution kinetics as dissolution can partly or almost entirely dependent on defect density.[117,118]

1.4 Previous Techniques for Studying Crystal Dissolution

Due to the range and variety of crystalline materials, a number of different methods for studying their dissolution have been required throughout the history of the field. The earliest methods were fairly simple, batch techniques, where a sample was placed into an appropriate solution and the reaction followed by removing and analysing aliquots.[119] These were easy to implement but unreliable. Once mass transport was better understood, hydrodynamic methods were introduced, which controlled mass transport allowing much more accurate and informative studies to be conducted.[120] In more recent years, scanning probe techniques have come into use,[121,122] which allow the reactions

of microscale sections of a crystal to be measured rather than an average of the whole surface that previous techniques were restricted to.

1.4.1 Batch Technique

One of the first methods for studying crystal dissolution utilised a batch setup in which powdered samples were dissolved in solution under controlled conditions.[123,124] This normally consisted of a beaker filled with an appropriate solution for the dissolution of the chosen crystal with a sample of crushed crystal powder. This powder is either recompressed into a disc or added in powder form to the solution. Dissolution rates were quantified by tracking the change of speciation in solution by taking aliquots and employing a complementary technique. The dissolution rates measured using this technique are averaged over all crystal faces exposed to the solution. This setup can be stirred but convection is usually complex and ill-defined.

1.4.2 Hydrodynamic Control Techniques

The next generation of crystal dissolution techniques introduced the ability to control the hydrodynamics of the studied systems. The first technique in this category is the rotating disc (RD) method. Based on the rotating disc electrode[125], this method used well-defined hydrodynamics to control and increase mass transport. A disc of the crystal to be studied, either made by compressing powdered crystal[126] or by mechanical cutting of a single crystal[127], is rotated in an undersaturated solution, the exact level of undersaturation and other factors such as pH[128] and temperature[128,129] can be chosen. The solution composition can then be monitored with respect to time as dissolution occurs, the method to measure this change normally consists of taking aliquots of the solution while dissolution is occurring and testing the composition for the concentration of the crystal being dissolved.[130] Higher mass transport rates allowed investigations of higher surface reaction rates by increasing mass transports rates and expanding the range of pure surface kinetics controlled systems that can be studied.[131,132] Not only is mass transport increased but also due to their well-defined hydrodynamics it is also possible to calculate intrinsic rates from mixed mass transport kinetic cases.[133] However, there is a physical

limit to how fast you can rotate a sample, this physical limit means that there is a maximum rate that mass transport can reach and systems with a higher surface kinetics than this can not be probed.

An alternative to RD was the Channel Flow Cell (CFC) methods in which the etching solution is flowed under laminar conditions through a flow cell which provides a well-defined hydrodynamics at the substrate surface.[134,135] Aliquots are removed from downstream of the flow cell and their composition can be measured with respect to time with a range of quantitative analytical techniques, *i.e.* Raman spectroscopy,[136] interferometry[129] or mass spectroscopy.[137] Real time monitoring can be performed by positioning an electrode downstream of the crystal to measure the rate of dissolution by electrochemically detecting the concentration of dissolved product.[138]

Limitations exist for these systems however, even if higher dissolution rates are accessible, for some systems the higher mass transport is still not high enough to enter a surface controlled system.[139] Flow rate and rotation speed can only be increased up to a point before reaching physical limitations. Another drawback is the sample preparation restrictions. These techniques require large flat bulk surfaces[127,140] or samples embedded in a support material.[134] No microscale analyse is possible as these techniques can only give a dissolution rate that is an average for the whole surface.

1.4.3 Scanning Probe Techniques

A different approach to dissolution measurements involves using scanning probe microscopy techniques to allow real time monitoring of crystal dissolution and eliminate a number of drawbacks the previous techniques were hindered by. Unlike the previous techniques, SPM can provide spatial resolution of crystal dissolution allowing the study of heterogeneities across the surface. Measurements are no longer limited to an average of the entire sample surface. Such techniques include *in-situ* atomic force microscopy (AFM),[141,142] and scanning electrochemical microscopy (SECM).[45,143] *In-situ* AFM has been used to track the movement of step edges along a crystal surface,[144] with the restriction that the rate must be slow enough that the step movement can be

followed on a series of images,[145,146] this speed reaches 20-50 nm s^{-1}. A wide range of materials have been studied, some include calcium based minerals such as dolomite, calcite[147,148] and gypsum[149] and weak acid compounds such as aspirin[102] and oxalate.[150] However, the use of AFM to measure reaction kinetics showed to be problematic; the probe has an impact on the hydrodynamics in the flow cell used during AFM experiments[151] as well as the tip having a wearing effect on the crystal surface.[152,153] This can introduce errors in the dissolution rate measured. Moreover, many works in the literature report a big discrepancy between dissolution rates measured via AFM and other techniques for the same material showing a difference between microscale and bulk measurements.[154]

SECM can be used to study crystal dissolution, the probe is positioned close to the surface of the sample to probe or trigger dissolution.[112] The probe can promote dissolution by generating a species that is reactive with the substrate e.g. H^+ for enamel[143] or calcite[155] etching. The work of McGeouch *et al*[143] looks at the dissolution of calcium hydroxyapatite (HAP), the major component of enamel. HAP is amenable to SECM study as it dissolves via acid attack following the equation:

$$Ca_{10}(PO_4)_6(OH)_2 + 8\,H^+ \rightleftharpoons {}_{10}Ca^{2+}_{(aq)} + 6\,HPO^{-2}_{4(aq)} + 2\,H_2O \qquad (1.6)$$

To avoid the problem of having to generate protons and record *in-situ* the resulting products, this study used the UME to quantitatively produce protons next to the surface of enamel and then study the etch pits *ex-situ* using interferometry. The parameters of the physical experiment were used to inform a novel moving boundary finite element method (FEM) model and rate information could be deduced. The simulated value for heterogeneous dissolution rate was found to be 0.08 ± 0.04 cm s^{-1}.

Corrosion is another field in which SECM can be utilised in a similar fashion. The corrosion of iron in Cl^- rich environments have been studied.[156] Samples of iron are held in a bulk solution of trichloroacetic acid, which can

be reduced to release Cl^- locally by the UME, following the reaction:

$$Cl_3CCOO^- + H_2O \rightleftharpoons Cl_2CHCOO^- + OH^- + Cl^- \tag{1.7}$$

The work of Seo *et al*[157,158] also studied the corrosion of iron but using a Ag UME coated in AgCl to deliver Cl^- to the surface. The probe was approached to the iron surface and the reaction shown in Equation (1.2) can be driven to the left hand side to generate Cl^- ions to dissolve the iron. A passive film was formed on the iron prior to dissolution and SECM was shown to detect the different products of passive layer and iron corrosion. SECM dissolution techniques can be used only with crystals which are stable in a bulk solution and their dissolution must be triggered electrochemically, e.g. pH change[143] or susceptibility to a certain ion, such as Cl^- on iron.[156] This high spatial resolution gives SECM the ability to make multiple measurements on a single sample.[159] A major drawback of this technique is that it requires the sample to be submerged in a bulk solution. There is also a lack of any feedback system to measure topography.

1.5 Surface Charge and the Electric Double Layer

Surfaces and particles often exist with an intrinsic surface charge, the nature of which arises from the terminal groups on the edges of the substance. For example, glass is an insulator but still has a surface charge due to the hydroxyl groups at the surface. In contact with a solution, the hydrogen can dissociate leaving a negative charge on the remaining oxygen atom. The charge on the surface will be compensated for in the solution by the creation of a layer of counter ions, this simplistic view of two layers of opposite charge gives rise to the name 'electric double layer' (EDL).

The EDL depends on a range of factors, such as solution concentration, pH, and surface charge. By controlling other dependent factors, the surface charge could be estimated through measuring of the EDL. The EDL can be defined in many ways as to include the interfacial charges at the interface of any two materials. However, for the purposes of the work herein it will

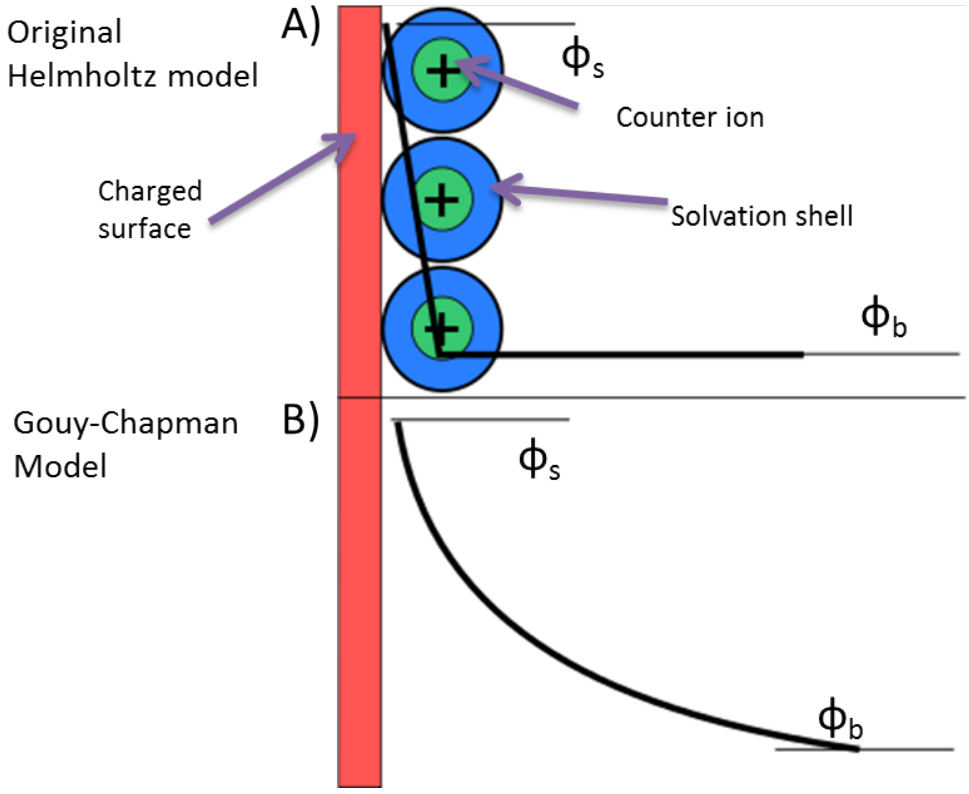

Figure 1.7: A) The Helmholtz model of point charges on an oppositely charged solid surface. Superimposed on the diagram is a sketch of the potential drop from surface potential, ϕ_s to the bulk potential ϕ_b. B) Gouy-Chapman model that represents the double layer as a continual and diffuse layer.

be defined as the surface charge on a solid surface and the opposite charge extending into a salt solution in contact with that solid.

This phenomenon was first proposed by Hermann von Helmholtz whose theory stated that surfaces in contact with a solution can build up charge like a capacitor. The Helmholtz model treated the counter ions as fixed to the surface of the solid in a 'compact layer'.[160] At the surface of the electrode the potential is at a maximum and decreases linearly away from the electrode. This layer extends only as far as the distance of closest approach to the center of the solvated ionic species (See Figure 1.7(A)). It was the starting point for developing an understanding of the double layer, but did not take into account a number of important physical factors such as the ions simultaneous moving under diffusion and convection and the possibility of adsorption of ions

to the surface. In the early 1910s, both Gouy and Chapman independently developed the Helmholtz model to consider the influence of both the charge of the solid and concentration in the solution. Instead of a single compact layer of adsorbed solvated ions, the EDL was described as a 'diffuse double layer' (DDL) where the ions are mobile due to Brownian motion and the length of the double layer varied with concentration. The potential charge extends out into the bulk whilst dropping exponentially in magnitude, as shown in Figure 1.7(B). The lower the concentration the further into the solution the DDL reaches, with less ions in solution the double layer must extend further in order to equilibrate the charge on the surface. The limits of this model are seen at high bulk concentration when ions, treated as point charges, have no maximum concentration close to the surface.[161] Despite this limitation for high concentrations, at low concentrations the Gouy-Chapman model is a good approximation and will be used in this thesis as the basis for calculating surface charge as all experiments will be conducted in solutions of low ionic concentration.

The model was developed further by Stern (Figure 1.8(A)) to have aspects of both the compact layer consisting of solvated ions close to the electrode and also the DDL.[162] This was an important step as it fixed a problem with the Gouy-Chapman model by accounting for the finite size of the ions and the minimum distance they can be from the surface. Grahame was then the first to outline a theory including the specific adsorption, which gave the double layer three distinct regions.[163] The first layer in this model is the inner Helmholtz layer (IHP), which accounts for specific adsorption of ions on an electrode surface. These ions have no solvation shell, and could be co-ions or counter-ions, and as such this will only occur for certain ions. For instance, it has been shown with electrocapilarity measurements on a mercury electrode that positive ions are highly unlikely to lose their hydration shell, whereas negative ions can adsorb to the surface.[164]

The outer Helmholtz plane (OHP), which is the same as in the original Helmholtz model, one ionic radius away from the electrode, when the ion is solvated. Beyond this is the diffuse layer, as described by Gouy and Chapman. A more recent model, called the Bockris, Devanathan and Müller

Model (BDM),[165] takes account of the fact that the solvent molecule is always the highest concentration of any species at the interface, as reflected in the representation shown in Figure 1.8(B). Common to all the models is that the majority of potential drop occurs close to the electrode, in all but the Gouy-Chapman model this is due to the presents of the compact layer. The BDM model predicts the potential drops with a higher gradient between the electrode and the IHP.[161]

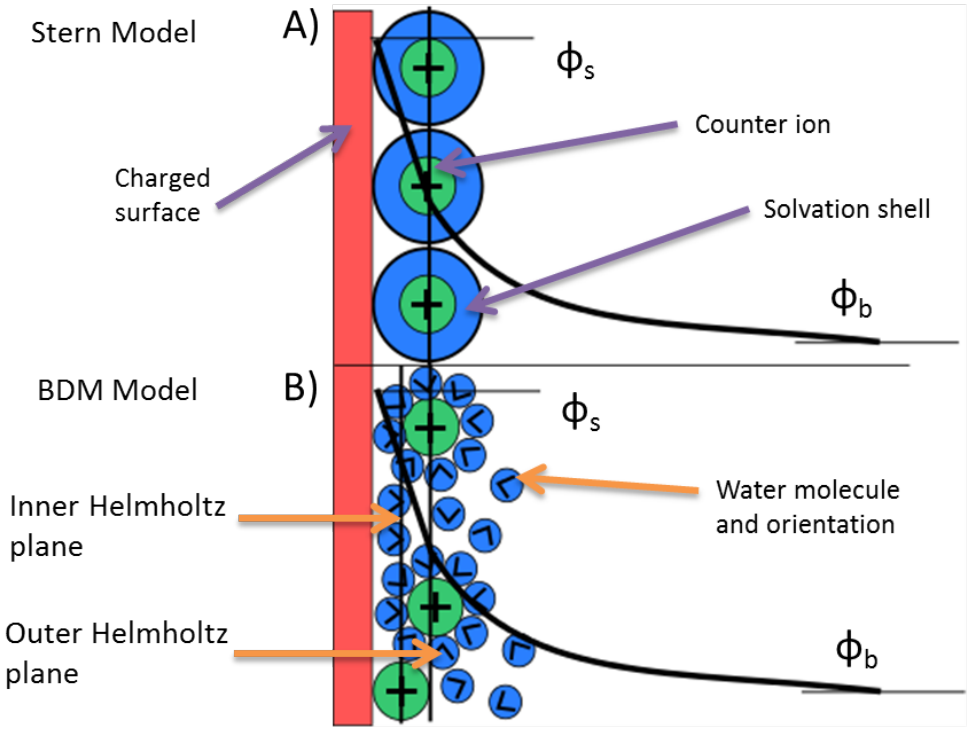

Figure 1.8: A) The double layer model developed by Stern which incorporates the ideas of both Helmholtz and Gouy-Chapman. B) The BDM model showing the abundance of solvent molecules at the surface and the three distinct regions: IHP, OHP and diffuse layer. Superimposed on both diagrams are sketches of the potential drop from surface potential, ϕ_s to the bulk potential ϕ_b

1.5.1 Current Methods for Probing Surface Charge

There are a number of techniques that can explore aspects of the double layer, one of the first methods employed for this purpose was taking electrocapillar-

ity curves from a glass capillary filled with mercury. The capillary is held in a bath of aqueous solution and has a mercury reservoir at the top, the potential between the mercury and aqueous solutions can be changed, which, in turn will change the surface tension. These measurements allowed surface tension *vs* potential to be plotted, thus by knowing the surface tension, a value for surface charge can be calculated. Unfortunately, this technique is applicable only to mercury, and due to its difficulty to implement and its toxicity, mercury is no longer commonly used as an electrode in electrochemical experiments. This technique presents no possibility of being used for non-conductive samples.

The surface charge on colloids is an important factor when designing them to resist coagulation, thus a range of techniques emerged to study what is known as the zeta potential of the particles.[166] The zeta potential is theoretically similar to the electric potential in the double layer, as the colloidal particles are dispersed in an ionic solution there exists a double layer, however the zeta potential is defined as a different point out into the bulk than either helmholtz planes. Electrokinetics[167] and electrophoresis[168] have been used to measure the zeta potential but are both based on the movement of colloids in an electric field. Because of this, only particulate matter can be measured rather than solid surfaces, and only an average of all particles is obtained. There is the possibility of using probing particles to measure the zeta potential of a surface, which has been demonstrated with new hardware (Desla Nano,Beckman Coulter).

An adaptation of AFM has been used for surface charge measurements, it has been shown that the force curve towards a surface is a function of the surface charge,[169] and the AFM setup is already capable of imaging on conductive and non-conductive surfaces. However, the tips needed to achieve this functionality are highly specialised. The method to fabricate reproducible tips is labour intensive and non-trivial.[170] In addition to this, all the drawbacks of standard liquid phase AFM still impact on results, soft samples will be compressed by the tip and introduce an error. Although these techniques have been vastly important for developing our understanding of the double

layer, none of them provide a robust and versatile platform for non-contact mapping of surface charge on a substrate.

1.5.2 Surface Charge Mapping

This thesis will introduce the concept of using SICM as a robust and simple technique for surface charge mapping. This introduces the ability to map functional surfaces, the spatial resolution of which is increasing as methods for fabricating nano-sized glass tips become more reliable, probes down to <50 nm radius have been reported.[171–173] However, to fully appreciate the data collected from these sub 100 nm probes, current rectification must be accounted for as it can be seen on glass pipettes[174] and nanopores[7,175] of this size regime. The double layer is a function of solution composition and surface charge therefore by knowing the precise solution composition and measuring the double layer a reliable value for surface charge is definable. Based on the Gouy-Chapman model the thickness of the double layer can be expressed as the inverse thickness of the double layer (κ cm^{-1}) defined as

$$\kappa \propto \varepsilon z \sqrt{C_b} \tag{1.8}$$

where ε is the dielectric constant, z is the charge of the ionic species and C_b is the concentration of ions in bulk solution. The variable κ represents the inverse of a characteristic thickness of the double layer at a given concentration and surface potential. To predict the double layer potential to its full extent into the solution the following equation can be used,

$$\phi = \phi_b e^{\kappa x} \tag{1.9}$$

where ϕ and ϕ_b are the applied potential at the surface and bulk potential, respectively, and x is the distance from the surface. These equations are based on reasonable assumptions but do not provide accurate values for surface charge. The problem is challenging as surface charge on a substrate can be highly heterogeneous.

SICM is in a unique position to study the double layer, as the probes used can be fabricated down to very small sizes with relative ease and repro-

ducibility, and the technique can be used with a wide range of samples and solutions. In order to observe surface charge, the double layer on the surface must be comparable in size to the diameter of the SICM probe, which in 10 mM salt solution, not only is possible, but also reproducible. The ability to map surface charge on the nanoscale will allow new research into tailoring how electrodes work under extreme or non-ideal conditions, how drugs interact with different cells or how to design functional polymers for better performance in a range of tasks, such as shampoo or colloidal paint and electrospray deposited paint.

1.6 Aims of this Thesis

Scanning probe microscopy techniques have a long history and an ever widening range of capabilities; the possibilities for functionality, speed and resolution are great. Improving SPM techniques is also of high importance because surfaces and structures need to be studied on the nano scale in order to be properly understood. It is one accomplishment to study a new system with existing techniques but another accomplishment altogether to design and build a technique better suited to studying emerging problems. This is why the next two chapters of this thesis are concerned with the methods and techniques employed. The second chapter not only outlines general experimental information but also gives a detailed description of the experimental setup, explaining the hardware and its uses. The third chapter deals with the software used to run the microscopes. An in-house LabVIEW codebase is described in this chapter. The main design point of the codebase is that only one version would be needed for any of the nine rigs that are available in the Warwick group. The codebase is flexible enough to accommodate variation in the hardware used for each microscope and also functional enough to allow for a wide range of experiments with different types of scanning probe.

The remaining chapters deal with two applications of microscopy: crystal dissolution and surface charge mapping. These topics are inherently linked, although the crystal dissolution in this thesis is explored using the dual-barrelled probes and surface charge with SICM probes, developing a method

to measure the surface charge of a dissolving crystal will be highly beneficial to our understanding of the process. The forth and fifth chapters look at using the SECCM setup for the study of NaCl and calcite dissolution. The NaCl study introduces the dual-barrelled conductance micropipette for studying dissolution with high time and spatial resolution. The fifth chapter is based on the same technique but this time combines the dual-barrel pipette technique with AFM. Using two different techniques that compliment each other is very powerful and provides more information about the system. Both these studies were completed with the addition of a FEM model designed to quantitatively deduce the dissolution rate constant in both systems.

The second branch of research starts at chapter six where the concept of surface charge mapping with a SICM probe is discussed and demonstrated on simple substrates. The techniques used is essentially SICM, however there are subtle differences such as using a much lower concentration of electrolyte in bulk solution and recording the phase of the AC signal generated. The ability to map surface charge is expanded upon in chapter seven where a bias-modulated (BM) approach is used to study a dynamically changing surface charge on an electrode. Not only could the surface be mapped while the potential was changed, but this technique is shown to open up the possibility of being used to elucidate the PZC of the sample. To the best of the authors knowledge there is lack of robust, reliable experimental methods for measuring the PZC on solid electrodes. Lastly, a conclusions chapter will bring together all the findings of the previous chapters and suggest some of the possibilities for future advances for which this work has laid the foundations.

Chapter 2

Experimental Methods and Instrumentation

> "We are stuck with technology when what we really want is just stuff that works."
>
> Douglas Adams

2.1 General Materials

All chemicals and materials were used as received, without further purification. Solid chemicals were weighed in a four decimal place balance (AAA 100LE, AE Adam). All crystal samples were mounted onto glass microscope slides (Thermo Scientific) NaCl crystals were grown from solution directly onto the slides and the natural calcite samples were secured with transparent nail varnish. All solutions used in SICM probes were filtered (200 nm,

Minisart Syringe Filters) as the diameter of the SICM probes are of a similar order to dust particles in the solution, which could cause the probe to become blocked. The solution for mercury electrode experiments was degased with BOC Pureshield Argon and had a supply of argon blowing over the solution during the experiment. A list of all other materials and chemicals can be found in Table 2.1

Table 2.1: List of all chemicals and materials used in this thesis.

Name	Details	Source
(3-aminopropyl)triethoxysilane	98%	Sigma Aldrich
11-dodecanethiol	98%	Aldrich
11-mercaptoundecanoic acid	95%	Aldrich
Acetone	99%	Sigma Aldrich
Alumina	na	Buehler
Chloroform	99%	Fisher
Dimethyldichlorosilane	95%	Sigma Aldrich
Hydrochloric acid	37%	VWR Chemicals
Isopropylalcohol	Reagent grade	VWR Chemicals
Mercury(I) nitrate dihydrate	97%	Sigma Aldrich
Nitric acid	62-66%	Sigma Aldrich
Perchloric acid	70%	Acros
Platinum wire	25 µm	Goodfellow
Poly-L-lysine	Mw 30k-70k	Sigma Aldrich
Polystyrene	Mw 280k	Sigma Aldrich
Potasium chloride	99%	Fisher
Potasium nitrate	99%	Sigma Aldrich
Silver wire	0.125 mm	Goodfellow
Silver wire	0.25 mm	MaTecK
Sodium chloride	99.92%	Fisher
Toluene	Reagent grade	Fisher

2.1.1 Solutions

Milli-Q reagent grade water (resistivity *ca.* 18.2 MΩ cm at 25°C) was used for all solutions in chapters 4 and 5. Purite water (same resistivity) was used in chapters 6 and 7. SECCM probes for dissolving NaCl were filled with 5 mM NaCl and for calcite acid induced dissolution 1 mM KCl and 1 mM HCl. 10 mM KCl (pH 6.6, Sigma-Aldrich) solutions were prepared for

the SICM charge mapping experiments on inert surfaces and Pt ultra micro electrodes (UME)s coated in self-assembled monolayers. For charge mapping experiments on an Hg electrode, 10 mM KNO_3 was used as the Cl^- ion is known to adsorb to the surface of mercury.[164] The pH values of electrolyte solutions were examined systematically before and after experiments to ensure stability, as pH could be a critical parameter controlling the charge properties of the interfaces, in particular those involving glass. Polystyrene (Sigma-Aldrich) was dissolved in chloroform (Fisher Scientific) at two different concentrations, one for creating a thick layer for SICM nanopipette approach tests (20 mg ml^{-1}) and one for dip-coating glass to create a thin (partial) film for imaging (0.66 mg ml^{-1}). A solution of (3-aminopropyl)triethoxysilane (APTES, Sigma Aldrich) and toluene (2 µl ml^{-1}) was used for glass surface modification with APTES. In order to protonate the amino groups and produce a positively charged surface, all experiments carried out on APTES samples were done in a slightly acidic solution of HCl (pH 3.4, Fisher Scientific) and KCl (9 mM). To create 5 µm diameter dots of poly-l-lysine (PLL) on glass, a solution of 0.25 mg ml^{-1} PLL with a supporting electrolyte of 25 mM KCl was used. A solution of 0.5 M KNO_3, 0.5 M HNO_3 and 1 mM $Hg(NO_3)_2$ was prepared for the electrodeposition of Hg.

2.2 Probe Fabrication

2.2.1 Capillary Probes

Dual-barrel conductance micropipettes were fabricated from borosilicate theta pipettes (30-0114, Harvard Apparatus) pulled to a sharp point using a laser puller (P-2000, Sutter Instruments). The laser heats the pipette and the puller slowly pulls the pipette longer, this step is known as the soft pull. At one point the hard pull is activated which pulls the pipette into two seperate pieces. There are many parameters to define the exact pull of the laser puller. Heat, which indicates the power of the laser. Filament (Fil) describes the spread of the laser, which will change the area of glass that is heated. Velocity (Vel) is the speed at which the hard pull starts. Delay (Del) allows the user to set a wait time between the soft and hard pull. Finally, the Pull (Pul) parameter

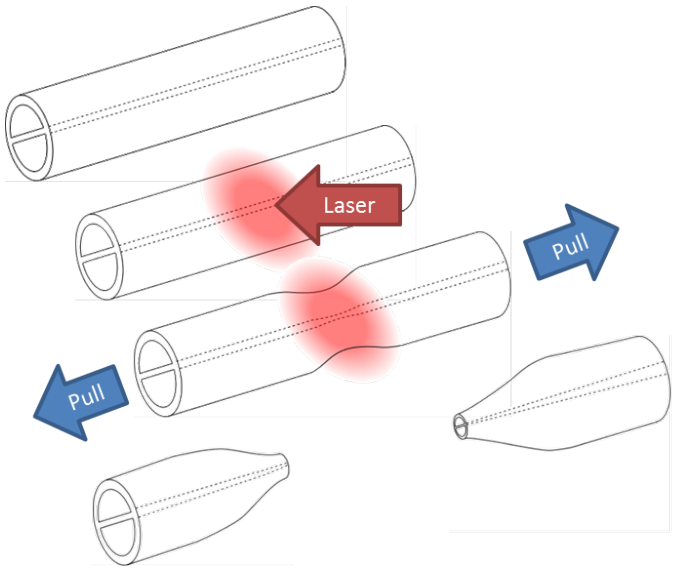

Figure 2.1: The pipette is first heated in the middle, causing the 'soft pull', then the 'hard pull' is activated and two probes are made. Not to scale

determines the strength the hard pull will use. Figure 2.1 shows a schematic diagram of the process. The pulling parameters used for the 1 µm probes are as follows: Heat 550, Fil 4, Vel 30, Del 120, Pul 28.

Each channel of the pipette was filled with 5 mM aqueous NaCl, together with a chloridized 0.25 mm diameter silver wire (99%, MaTecK) that acted as a quasi-reference counter electrode (QRCE) to form the conductance cell.[90] Experiments were performed with pipettes of dimension (effective radii) $r_p = 0.65$ µm perpendicular to the septum, and dimension $r_t = 0.4$ µm parallel to the septum from the center to the inner edge. The pipette semi-angle (σ) was typically 8°. The outside walls of the pipette were silanized with dimethyldichlorosilane which functionalized the glass with a hydrophobic coating thereby keeping the meniscus confined to the end of the pipette.[90] This was achieved by dipping the tip into the silane solution for 60 seconds and then leaving the tip to dry in air for 120 seconds, throughout the process argon gas was flowed down the pipette to prevent the silane from entering inside.

Single barrel probes used for SICM were 60 nm radius nanopipettes with a half cone angle of 3°(dimensions measured with a Zeiss Supra 55VP field

emission scanning electron microscope, FE-SEM) were pulled from borosilicate glass capillaries (o.d. 1.2 mm, i.d. 0.69 mm, Harvard Apparatus) using a laser puller (P-2000, Sutter Instruments, Pulling Parameters: Line 1: Heat 350, Fil 3, Vel 30, Del 220, Pul -, Line 2: Heat 350, Fil 3, Vel 40, Del 180, Pul 120).

2.2.2 Ultramicroelectrodes

The platinum UME were fabricated according to the standard method for creating UMEs with an electrode diameter of 25 µm.[176] A diagram of the UMEs features can be seen in Figure 2.2(A) A wide, single barrel capillary (2.0 mm OD, 1.16 mm ID 100 mm length, Harvard Apparatus) is pulled slightly to a taper at one end, the resulting capillaries used for the work in this thesis were ∼3 cm in length, this was to ensure the UME was compatible with the XY piezo sample holder. A 1 cm length of Pt wire of diameter 25 µm is inserted into the tip. The wire is then permanently sealed into the glass by heating the glass around it. At this point the UME is checked to ensure a good seal of glass around the wire and that no air bubbles have formed. An electrical contact is made by inserting a small volume of silver epoxy (RS Components) into the capillary to make contact with the electrode wire. A 1 mm copper wire that is longer than the length of the capillary is then inserted into the silver epoxy, the section of wire that protrudes from the end of the UME is used to establish an electrical contact and is secured in place in the glass capillary with epoxy. Lastly, the UME is polished in two steps. The geometry of the end of the tip is important when using the UME as a probe,[177] however in this thesis they are used as a substrate that a SICM probe lands on so a large glass to electrode diameter ratio was actually desirable. The more a UME is polished the wider the glass becomes. The coarse polishing step involves polishing the UME on a rotating polishing wheel onto pads of grit size ranging from 5 µm to 100 nm from Buehler. This makes the surface of the UME flat, but there will still be rough steps and polishing lines. The fine polishing step achieves a smooth surface and is performed by hand. The UME is moved in a figure eight on microcloth pads (40-7212, Buehler) covered in a water/alumina mix, then to clean the alumina away, another pad with only water is used. A diagram of

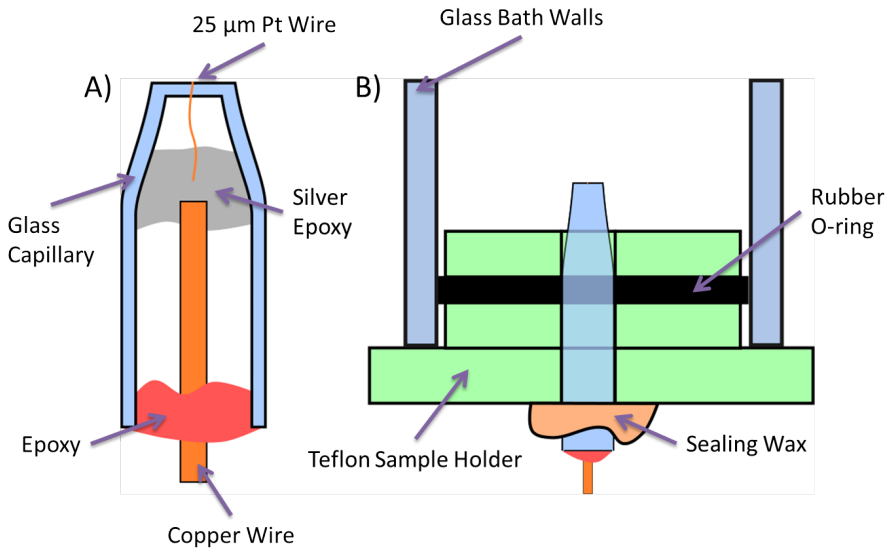

Figure 2.2: A) The cross section of the completed UME. The setup for landing on an inverted UME is shown in (B). Not to scale

the UMEs features can be seen in Figure 2.2(A)

Either of these steps can be used during the lifetime of the UME to clean the electrode. The fine polish was performed immediately prior to every mercury deposition. In order to deposit thio SAMs onto the UMEs a more rigorous cleaning procedure was employed. The UMEs were cycled in 500 mM perchloric acid, this destroys any previous SAM layer and removes any other organic contaminates.[178] Due to the speed at which Pt electrode foul when exposed to air, the UMEs were removed from the acid, rinsed with Milli-Q water and submerged in the SAM solution within a minute.

The design of the inverted UME holder can be seen in Figure 2.2(B). The cylindrical teflon cell was designed to fit a sample holder of the 300 by 300 µm XY piezos. The mounting for the piezos meant the sample sat only 6 cm from the table requiring short UMEs to be used. The UME was inserted into a hole in the middle of the teflon cell from the back and sealed with wax to prevent leaks. A glass cylinder was placed firmly down over the rubber O-ring to form the water-tight solution bath.

2.3 Characterisation Techniques

2.3.1 Atomic Force Microscopy

An atomic force microscope (AFM), Veeco BioScope Catalyst Atomic Force Microscope, (Bruker) with a Nanoscope V controller (Veeco) was used to characterise a range of samples. The roughness of the NaCl and calcite samples and the morphology of the etch pits produced were extracted from AFM images. The topography of the polystyrene/glass substrate was imaged in order to compare to the results of the SICM surface charge. NaCl was imaged in 'Scan Asyst' mode, a form of tapping mode with the addition of proprietary software to analyse tip response and maintain optimal settings. The remaining samples were relatively hard compared to an AFM tip so a contact mode was used for speed. For both methods of imaging the same variety of tip was used, which was a silicon tip on the nitride lever (SNL-10, Veeco). AFM images were processed using the Scanning Probe Image Processor program (SPIP 6.0.14, Image Metrology).

2.3.2 Scanning Electron Microscopy

To measure accurate probe tip dimensions field emission-scanning electron microscopy (FE-SEM) (Supra 55-VP, Zeiss) was used. The dual-barrel conductance probes were ∼1 µm diameter and could be imaged clearly by simply attaching them to a SEM peg with silver paint (RS Components, UK). A low power of ∼0.5 to 5 kV was used to prevent charging of the tip, most images were acquired in backscattered electron mode. SICM probes, being an order of magnitude smaller 100-120 nm for borosilicate probes and 50-60 nm for quartz probes, were sputter coated with gold (10 nm thickness). This conductive layer improved the ease with which images could be acquired but this method produced mixed results in quality.

Table 2.2: List of rigs and their permanent features

Name	X/Y (µm)	Z (µm)	Features	Suitable experiments
High Sensitivity	12	38	Low noise	Single particle
Top View	300	38	Multiple cameras	Non trivial probe positioning
Environmental	200	38	Environmental cell	Anaerobic experiments
Fast Scanning	30	38	Highly sensitive piezo	Fast scanning and spiral scanning
Fluorescence	300	38	Flurorescence light in inverted microscopy	Transparent and biological samples
Illumination	100	100	LED lightsource	Photo voltaics
Soft Piezo	500	100	Addition soft piezo	SECM
Inverted Mic	100	100	Inverted Microscope	Transparent samples
Confocal	100	100	Confocal Microscope	Confocal

2.4 Electrochemical Scanning Probe Microscopy Instrumentation

This section will deal with the general setup and function of the collection of instruments within the group using the FPGA card and codebase, each instrument will be referred to as a 'rig'. There are nine rigs in operation at the time of writing. Although in theory, any experiment could be performed on any rig with the same accuracy and low noise level, some samples require specific sample holders or an experiment requires a piece of specific hardware. Table 2.2 displays a list of rigs and the features that are not interchangeable, and therefore some experiments are preferentially performed on certain rigs. All current followers and potentiostats are interchangeable between rigs. Specifics for the experiments within this thesis will be discussed in the relevant chapter.

2.4.1 Probe and Sample Movement

Of the nine rigs currently employing the FPGA codebase, five of them operate with XY sample movement controlled via various piezoelectric positioning systems and the probe movement is separate and restricted to only the Z axis. This system is beneficial as the Z axis can have a smaller range and higher resolution and noise inducing 'crosstalk' between piezos is limited to the X and Y axis. Three of the remaining rigs employ a 'cube' piezo and move the probe in three dimensions over a stationary sample. The last rig moves the probe in three dimensions but the X/Y and Z piezos are two separate entities. This rig also has an additional 'soft' piezo to oscillate the probe in the Z axis in order to measure damping. A full list of the rigs and piezos is shown in Table 2.2. All piezos were purchased from Physik Instrument (Germany), with the exception of the 300 by 300 µm XY piezos which are from Mad City Labs (US).

In addition to piezos a coarse, long range movement control was required. Each rig has manual micropositioners in three dimensions for the probe and three rigs have an additional X and Y axis micropositioner for the sample. Due to the wide range of samples that can be used the ability to move the probe and the sample in the X and Y axis in order to align the camera to the area of interest has been found to be highly useful. All rigs are equipped with computer controlled, coarse movement picomotors on the Z axis so that the probe can be manipulated to close range of the surface without the risk of human error and without having to open the Faraday cage, compromising thermal stability.

2.4.2 Signal Generation and Collection Hardware

With the exception of the piezos, all hardware is easily interchangeable between rigs as can be seen in Figure 2.3. A full list of hardware with a brief description is shown in Table 2.4. The breakout box, Figure 2.3(A2), addresses all the inputs and outputs of the FPGA card to separate Bayonet Neill-Concelman (BNC) connectors. A list of the addressable channels to and from the FPGA card, through the breakout box is shown in Table 2.3. As the breakout box is

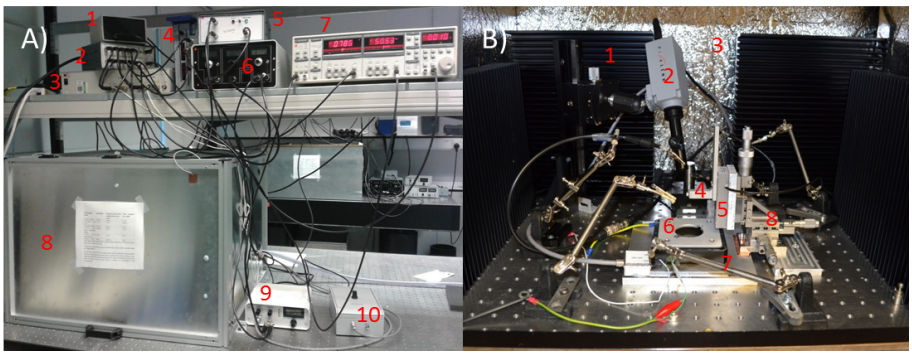

Figure 2.3: A) Typical Rig setup showing 1.Picomotor controller, 2. Breakout box, 3. X/Y Piezo controller, 4. Z Piezo controller, 5. Signal Adder, 6. Bipotentiostat, 7. Lockin Amplifier, 8. Faraday Cage, 9. High bandwidth electrometer and 10. Low noise electrometer. B) Inside the Faraday cage of a typical rig showing 1. Heat Sinks, 2. Camera, 3. Vacuum insulating panel, 4. Probe holder, 5. Z Piezo, 6. Sample holder, 7. XY Piezo and 8. Manual Micropositioners

a custom built piece of hardware, in order to connect it to the FPGA card an unterminated shielded cable assembly (SHC68-NT-S, National Instruments) was used. The large majority of hardware is connected with BNC to BNC cables (RG58, 50 Ω OneCall, UK).

2.4.3 Lockin Amplifiers

In order to use small AC currents as feedback in techniques such as SECCM and SICM it is vital that they are detected accurately. Lockin amplifiers can significantly increase the signal to noise ratio. A reference sine wave is applied to the experiment, the signal from the experiment then has the same frequency as reference. The signal from the experiment (now containing noise) is fed back in to the phase sensitive detector (PSD) in the lockin, and is multiplied by the reference. This creates a new signal with components from experimental noise and the experimental signal. Any component with a different frequency to the reference (the noise) with create an AC component. The experimental signal will have an identical frequency to the reference and when multiplied together, these frequencies will cancel out and produce a DC signal. A low pass filter is applied to the output of the PSD, eliminating all the AC components, which were the noise. The lockin has an additional PSD which applies the same

Table 2.3: List of inputs and outputs from the FPGA card to the experiment through the breakout box

Label	Function
AI0	Real X position
AI1	Real Y position
AI2	Real Z position
AI3	Current 1
AI4	Current 2
AI5	AC Ampiltude
AI6	Current 3
AI7	AC Phase
AO0	Desired X Position
AO1	Desired Y Position
AO2	Desired Z Position
AO3	Voltage 1
AO4	Voltage 2
AO5	X Picomotor
AO6	Y Picomotor
AO7	Z Picomotor

function but with a reference offset by 90°. The AC amplitude and AC phase of the experimental signal is then calculated from these two PSD outputs.

Both hardware and software based lockin amplifiers can be used, however, due to the use of the FPGA card to maintain speed the lockin amplifier would have to be implemented on the card itself. The amount of space on the card is limited and with hardware versions having an advantage on speed against software anyway, all rigs were equipped with a hardware based lockin amplifier. The lockin amplifiers used in this thesis (Figure 2.3(A7)) generate their own reference signal which is output as the AC signal and superimposed onto either the Z position signal for distance modulation modes or the DC signal using the signal adder (Figure 2.3(A5)).

2.4.4 Shielding

All rigs are stood on anti-vibration tables to protect them from the physical vibrations. Any source of vibration has the potential to crash a probe when

dealing with probe to substrate separations of mere nanometers, this includes people walking in the lab and cars on the road outside. Each Faraday cage has acoustic foam coating the inside to provide a layer of vibrational protection.

The sample, probe and electrometer are housed inside a Faraday cage (Figure 2.3(A8)) grounded to the mains electricity supply, to insulate the experiment from electrical noise. To further improve the level of electrical noise, the mains line is run through an isolation transformer (Carroll & Meynell (UK)) before it reaches the rig's hardware. This serves to clean the AC mains signal to lower the noise contribution from the mains and to protect from electric shocks from the large volume of equipment.

Piezo materials are susceptible to thermal drift if they are exposed to a temperature gradient. For many experiments this is not an issue and would be less noticeable than sample tilt, both of which can be corrected for in data post-processing. However, for the instances where relative piezo position to a sample must be known and/or maintained, several measures ensure thermal stability. The inside of the Faraday cages, including the doors, have vacuum insulating panels (Figure 2.3(B3)) installed. Large aluminium heat sinks (Hamilton Sundstrand, USA) surround the sample holder to speed the environment reaching thermal stability and maintain it, Figure 2.3(B1).

2.5 Data Analysis Using MATLAB

A LabVIEW code written in-house was used to collect data, however LabVIEW is not well suited to analysing large volumes of data. For all data analysis, processing and graph presentation of data from the rigs a program called MATLAB (MathWorks) is used, it is a programming language specializing in handling large matrices of data, hence the expanded name: MATrix LABoratory. The data files from the rigs are saved in a tab delimited format of up to 15 channels and potentially millions of data points. For any experiment a custom program was coded in-house to process the data. To fully take advantage of the bespoke rig hardware it is necessary to write analysis programs on an individual basis so that new experiments and methodologies can be tested. Even with only a rudimentary knowledge of the MATLAB language, analysis programs can be written quickly to suit the exact needs of a particular

experiment. The ideology of each program is to search through the data file and identify the important sections based on the Line Numbers recorded, then perform the required analysis and processing on the chosen sections. An explanation of Line Numbers and data file structure can be found in Section 3.4.2. A multitude of analysis programs were written preforming functions such as aligning multiple dissolution transients on the same graph, normalising and plotting approach curves and generating movies from 2D cyclic voltammetry data.

Table 2.4: Rig hardware list, labels refer to Figure 2.3

Label	Name	Source	Function
A1	PicoMotor	In-house	Controls the picomotor positioner
A2	Breakout Box	In-house	Converts the wires from the FPGA card to BNC connectors
A3	XY Piezo Controller	Mad City Labs (US)	Applies voltage to the XY piezo and outputs the piezo position
A4	Z Piezo Controller	Physik Instrumente (Germany)	Applies voltage to the Z piezo and outputs the piezo position
A5	Signal Adder	In-house	When a DC and AC signal are input the combination of those signals are output
A6	Bipotentiostat	In-house	Holds two electrodes at a set potential and records the current between them
A7	Lockin Amplifier	Stanford Research Systems (US)	Filters noise from a signal in order to amplify and measure a single frequency
A8	Faraday Cage	In-house	Grounded to the mains trunk, the cage shields the experiment from electrical noise
A9	High Bandwidth Electrometer	In-house	High sensitivity current follower with local, changeable heads
A10	Low Noise Electrometer	In-house	Standard current follower for low noise experiements
B1	Heat Sinks	Hamilton Sundstrand (US)	Maintain thermal stability
B2	Camera	PixeLink	Locating area of interest on samples and aligning probes
B3	Vacuum Insulating Panel	Kevothermal (UK)	Maintain thermal stability
B4	Probe Holder	In-house	Provide a temperory but stable connection between the probe and the Z piezo
B5	Z Piezo	Physik Instrumente (Germany)	Fine positional control of the probe
B6	Sample Holder	In-house	Metal holder for keeping samples stationary and flat
B7	XY Piezo	Mad City Labs (US)	Fine positional control of the sample
B8	Manual Micropositioners	Newport (UK)	Coarse manual positioning of the probe
Not pictured	Picomotor	Newport (UK)	Coarse motorized positioning of the probe
Not pictured	Lightbox	Edmund Optics (UK)	Illuminates the setup
Not pictured	Isolation Transformer	Carroll & Meynell	Cleans the mains DC signal

Chapter 3

Development of the LabVIEW Code for Scanning Probe Microscopes

> "Humans are allergic to change. They love to say, "We've always done it this way." I try to fight that. That's why I have a clock on my wall that runs counter-clockwise."
>
> Rear Admiral Grace Hopper

All of the electrochemical microscope rigs are controlled by a single codebase. LabVIEW was chosen as the programming language, it is a graphical based, inherently parallel language which was built on the basis that scientists without formal coding experience would be able to learn and use it. LabVIEW is the proprietary property of National Instruments.

Rather than line-by-line written code, LabVIEW code is a series of 'nodes' representing functions and 'wires' connecting variables between them. This intuitive system is meant to mimic physical electronic circuit boards and is referred to as the 'block diagram'. The LabVIEW coding environment is designed to generate entire usable programs and as such has a built-in user interface which is generated along with the block diagram code. The name given to this graphical interface is the 'front panel'. All objects displayed on the front panel are designed to mimic the buttons and controls on physical instruments. This gives rise to the file extension '.vi' standing for 'virtual instrument'. LabVIEW was chosen as it offers a number of advantages over tradition line-by-line coding languages. The ethos of its design, to be intuitive and to mimic physical components, allows a stream of PhD students to maintain and update the code rather than having to have an expert. It has a coding environment already equipped to handle a wide variety of hardware input-output functions, with many downloadable packages and has excellent support for the FPGA card. Crucially, LabVIEW code does not explicitly specify execution order and therefore multiple loops can be coded onto the FPGA card to run in parallel by default, this provides a massive boast in the data acquisition speeds possible, without a developer needing the programming expertise necessary to write parallel code in other languages. The downside of graphical programming is that it does not run smoothly on Subversion (SVN) programs and can not take advantage of the file merging options. This leads to potential version conflicts and loss of local changes.

The original code was written by Kim McKelvey[179] and is designed to be compatible with all (currently nine) microscopes in the group. This was achieved by using a subversion client, TortoiseSVN, to handle both the development and distribution of the LabVIEW software. Subversioning allows changes to be made and tested on the local copy on a single rig, before being committed to the server. This allowed safe testing of new functionalities with the previous versions being preserved. A full history of each version is saved even after new changes were made to the latest or 'HEAD' revision. The added benefit is that once a functionality in the code has been completed every PC

can download and use the new HEAD revision, this allowed new techniques and features to be made available to use on all microscopes.

An important element of this system is to ensure that the entire codebase is compatible with every microscope, therefore microscope computers all ran on Windows XP initially, some were later upgraded to Windows 7 after testing the compatibility of the code, which required no changes. All microscopes used LabVIEW 13.0 with a RIO0 PCIe-7852R FPGA card (National Instruments). The hardware of the microscopes varies a little, such as piezo distance range and current follower sensitivity so enough options and settings were programmed in order to account for these differences.

Since the departure of the original developer, Kim McKelvey, the codebase has been made available to his new institution, The University of Notre Dame, to another Warwick alumni working with Prof. Henry White at The University of Utah and recently to Prof. Bo Zhang's group at The University of Washington.

3.1 Field Programmable Gate Array Cards

The technology that allowed the creation of a fast, flexible and widely compatible codebase is the Field Programmable Gate Array (FPGA) card. The card is a silicon chip that contains an array of logic blocks, which can be connected and reconfigured. Using the FPGA module for LabVIEW (Xilinx, USA), a labview .vi file can be converted into a .bitfile which can be configured on the card as hardware, this file is known as the Target. The main advantages of this is the Target file can be changed and updated so the card hardware can be changed without being replaced. Another advantage is the greatly improved speed of the card compared to the PC, up to a maximum sampling rate of 750 kHz. The Target program employed herein runs two 'while' loops simultaneously. One loop handles sending predefined instructions to the outputs in order to control the hardware, while the other simultaneously records data.

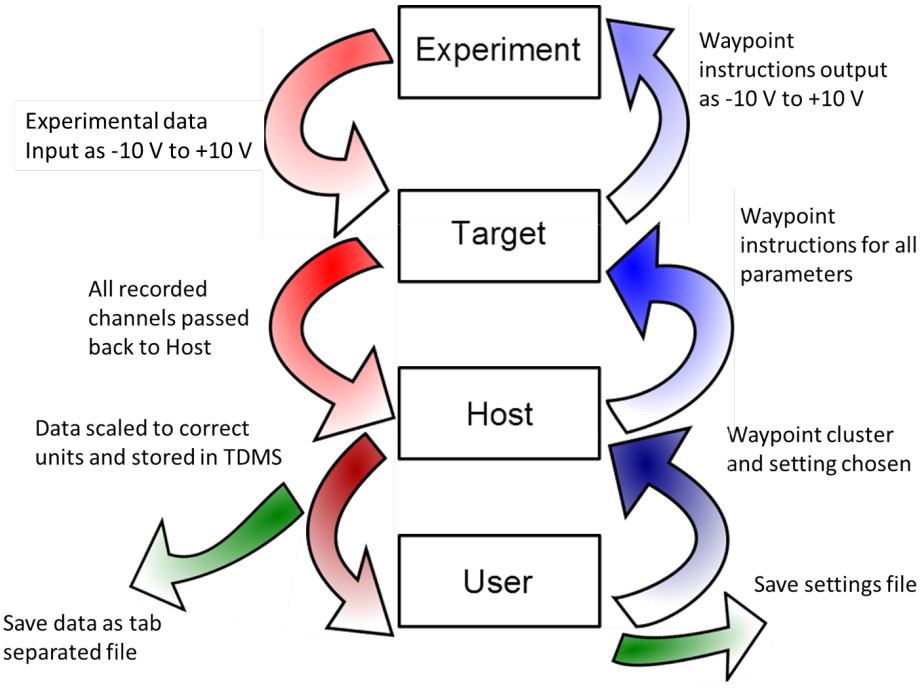

Figure 3.1: The waypoint array is constructed in the User Vi for a specific experiment and then passed to the host. The host converts the waypoints to I16 integers and sends them to the target. The target executes the instructions for each waypoint and simultaneously collects data from the experiment. That data is sent to the host and scaled to the correct units then saved in a binary file, any data needed to be viewed in real time by the user is sent to the User VI. At the end of an experiment all settings from the User VI are also saved.

3.2 Waypoint Instructions

To receive instructions from the user to the Target, there is a three level system of software, shown in Figure 3.1, firstly the user has access to one of the many User VIs. Each User VI allows the user to specify the variables needed for a specific experiment, when variables need to change that is called a 'waypoint'. A full set of variables, any that were not defined by the user are set to default values, creates a single waypoint (See Table 3.1 for the full waypoint cluster). In order to change any output channel during the experiment a new waypoint is needed, therefore the User VI calculates how many waypoints are required and creates an array of all user defined variables for each waypoint.

'X', 'Y', 'Z', 'V' and 'V2' are the applied position for the three piezos and two voltages, each of them have a variable to control their velocity when changing value, and a 'Move' boolean to indicate whether they are allowed to change value. 'Jump V' and 'Jump V2' are booleans that control whether the voltage positions change immediately to their new value, ignoring the velocity variable or ramping to the new value at the speed set in their velocity variable. The 'Hold' boolean allows or disallows the use of 'Hold Time', a value input as µs, which delays the next waypoint until the 'Hold Time' has passed. 'Hold Time' is only a minimum waypoint duration, if any movements in the waypoint take longer than the 'Hold Time' the waypoint will not stop prematurely. For simplicity, when using 'Hold Time' it is advisable to make a waypoint separate from any other movement. 'Feedback Type' controls the logic of the Z piezo position movement. These are explained in Section 3.4.1. Almost all experiments depend on a scanning probe interacting with the surface below it. A change in current 1, current 2, amplitude or phase can be used to detect when the probe has reached the surface. 'Update Position Loop Wait Time' is only used when 'Feedback Type' is set to 4 or 5 as it is the variable which controls the speed of the proportional feedback.

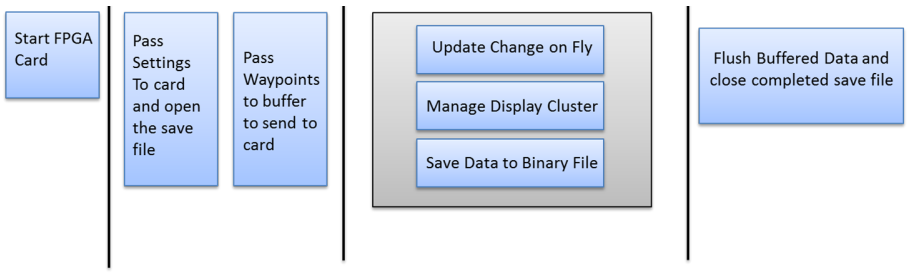

Figure 3.2: Schematic of the Host, black vertical lines represent frames in a sequence structure and the grey box represents the while loop.

3.3 The Host Program

The next stage shown in Figure 3.1 is the Host, which acts as a intermediary between the User VIs and the Target, controlling all communication between the computer and the card. The waypoint array generated in the UserVI is passed to the Host. The waypoints are scaled and converted to 16 bit signed integers (I16) and condensed into four 64 bit unsigned integers (U64) with boolean type waypoint variables taking up a single bit per variable, before being passed through the 'Host_to_FPGA' buffer, a first in first out (FIFO) buffer, to the card. The buffer allows long and complicated scans to be run without having to load all waypoints at once. The Host also draws all variables from the Settings and Advanced Settings VIs and sends a subset of these to the target. The remaining settings inform on Host level logic. For a full list of setting see Table 3.2 and Table 3.3. The codebase has grown in size and scope enough that the settings are split into two groups. The Advanced Settings hold all the setting that are needed as global variables that are not likely to change, and when they are changed it must be by an experienced user or developer. The Settings cluster holds variables even the most basic user should have an understanding of, ones that will be changed between user or during a day of experiments from one user. These are split again between the Settings VI that the user can access and the Settings cluster which moves the values to the required subVIs.

A subset of variables can be changed after the waypoints have been created, they are listed in Table 3.4, and are referred to as the 'Change on

Fly' variables. Their values are constantly updated in the Host and passed to the Target in real time. Changing a variable using the 'Change on Fly' cluster will override the value that variable was given in the Waypoint cluster.

3.4 The Target Program

The Target, as mentioned in Section 3.1, runs two parallel loops, one to send the waypoint information to the breakout box (explained in Section 2.4.2) and the other to receive data collection channels from the breakout box and send them to the Host. Figure 3.3 shows a schematic of Targets structure. Before the two loops start to run all variables for inputs and outputs from the Host are initialized. Variables are either static (do not change during the course of a single experiment) or dynamic (changes often during an experiment). These are listed in Table 3.5 and Table 3.6, respectively.

3.4.1 Waypoint Output Loop

The waypoint output loop controls movement of the X piezo, Y piezo, Z piezo, V and V2 outputs and also the Picomotors (explained in Section 3.8.4). Firstly, each waypoint is split back down from a single U64 integer to the I16s and boolean values for the separate waypoint variables. The V and V2 outputs also contain logic to accept new values if the 'Change on Fly' options are being used. The X piezo and Y piezo output are the most straightforward, they move according to waypoint details. The Z piezo output has significantly more flexibility as it has different feedback types (FT), for a list see Table 3.7. FT 1 and 2 approach the probe to a surface until a setpoint is reached, FT 1 will pause for user input and FT 2 will automatically starts the next waypoint. FT 3 moves 'Z' when it's starting position can not to predicted, this occurs when the probe needs to retract a set distance from a surface during a hopping scan. FT 4 is a proportional distance controller, it is used for maintaining constant probe to substrate separation during raster scans. The system is highly sensitive and can be controlled with three user defined variables, 'P' and 'Upper dZ limit'. The proportional factor, 'P', updates on the fly, from

an input on the UserVI, and is used to scale the change in feedback channel into an appropriate change in Z piezo position according to the equation:

$$(ExtVal - SetVal)P = dZ \tag{3.1}$$

Where $ExtVal$ is the incoming value of the channel being used for feedback. $SetVal$ is the setpoint in the signal chosen for feedback, commonly the AC signal where a certain setpoint represents a fixed height above the surface, and dZ is the change in 'Z' value in either direction and is added to the current Z piezo position after being coerced to ± 'Upper dZ limit'. The last variable used to ensure smooth feedback is 'Update Position Loop Wait Time' which forces a minimum time between movements. FT 5 performs the same function as FT 4 with the addition of storing X and Z positions in a buffer as the scan is running. FT 6 uses no feedback but precisely retraces the movements of the scan performed with FT 5. These two FTs are used for making multiple scans of the same area, to generate frames for a video of the surface. In order to increase frames per second, once the topography is known subsequent frames can be scanned at higher speeds without risking damage to the tip. FT 7 is also the proportional controller this time with the addition of a second feedback signal that will pause the movement of the tip. This FT is used for scanning over samples containing small features such as nanotubes or particles, and stopping when they are located using the second signal, Current 2 is commonly used for this purpose. FT 8 is an approach which, instead of using an absolute value as a feedback setpoint, uses a self-referencing setpoint, for more information refer to Section 3.8.3. FT 9 is used as a temporary and experimental FT, at the time of writing it is being used for a running average approach, described in detail in Section 3.8.3.

3.4.2 Data Acquisition Loop

The Target uses I16 integers to output voltages to the eight output analogue channels where 32767 outputs +10 V and -32767 outputs -10 V. When the Target outputs the first waypoint it simultaneously starts to records I16 integers from all eight input channels. The two variables in Settings 'Samples to Average' and 'Sample Time' determine the data collection rate. 'Sample

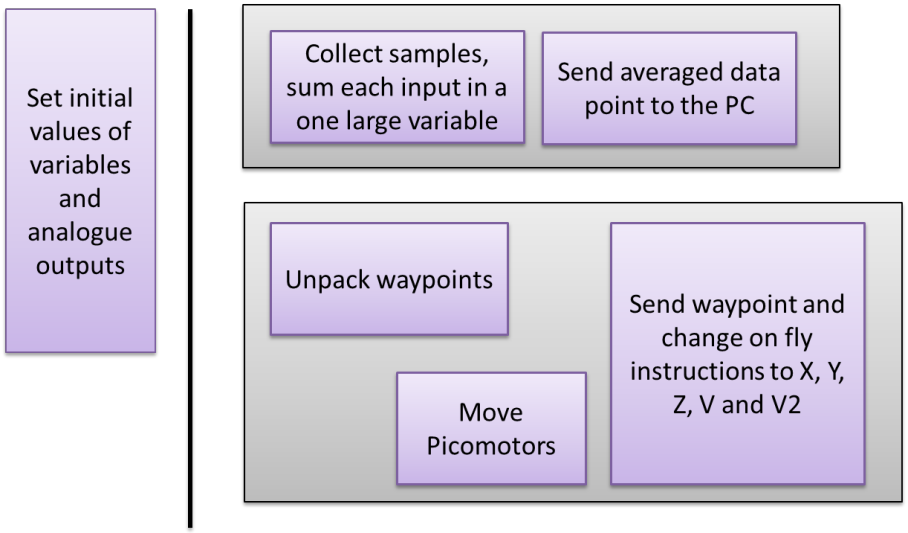

Figure 3.3: Schematic of the Target, black vertical lines represent frames in a sequence structure and the grey box represents the while loop.

Time' in microseconds is how fast the data collection loop on the Target runs, each time it runs the I16 input from the channels are added to a cumulative total for each channel. A number of samples equal to 'Samples to Average' is collected and summed together, this cumulative total is then averaged which creates one data point consisting of a value for each channel. One additional run of the data acquisition loop sends the data point to a buffer. As the Target can only handle integers 'Samples to Average' is coerced to be a power of two allowing a resource efficient bit shifting function to be used rather than a divisor and a floating point decimal. The rate of the data collection (D_r) in Hertz is calculated as follows:

$$D_r = \frac{1 \times 10^6}{(S_{avg} + 1)S_{time}} \tag{3.2}$$

where S_{avg} is 'Samples to Average' and S_{time} is 'Sample Time' in microseconds. The data collection loop runs 'Samples to Average' times to record one datapoint. In order to send that datapoint to the FPGA_To_Host_FIFO the data acquisition loop runs once more, hence the need to increment S_{avg} before converting to Hertz. The maximum speed the data collection loop can run is 1.2 µs, for simplicity the input 'Sample Time' this is coerced to a minimum of 2 µs. The minimum 'Samples to Average' can be is 8. If 'Sample to

Average' is lower than this the buffer will overflow. Therefore the maximum rate of the data collection is 55 kHz. As the samples are averaged to generate one data point a trade off is created between data collection rate and level of noise. For more averaging and lower noise it is recommended that the 'Samples to Average' be increased as there is less advantage in increasing 'Sample Time'.

Not all channels to be saved come from the external experiment via the breakout box. A single data point is defined as a set of 15 values, one from each channel that is recorded, a full list is shown in Table 3.8. Only eight channels come from the breakout box, there are seven more that are generated internally. Five of these are the XYZ piezo and voltage 1 and voltage 2 output signals, the remaining two for 'Feedback Type', which has already been discussed in Section 3.2 and lastly, 'Line Number'. 'Line Number' is used to label each waypoint in order for the data to be processed later. When a waypoint ends and another begins the 'Line Number' increases by 1. It is advisable that the minimum amount of comments in a waypoint generation program is to list the first set of 'Line Number's and what function they serve. 'Line Number' should increase linearly, however, there are three reasons that may cause 'Line Number' to skip a value. Firstly, although the 'Line Number' always sets to 1 at the start of a scan, this waypoint is normally used to initialise all the channels and therefore this 'Line Number' is often very short, perhaps only having one or two data points recorded at 'Line Number' 1 or none whatsoever. Secondly, programs that use optional hold times or CVs programs that are being used for only a LSV will 'skip' 'Line Number's because the next waypoint is identical to the previous so no channels need to move, therefore making the waypoint infinitely fast and no data points will appear as that waypoint's 'Line Number'. Lastly, despite having a waypoint with channels that move, if the movement is sufficient small and data collection rate sufficiently slow, the movement may be completed within the time the data collection rate takes to run and therefore no data points will be recorded with the 'Line Number' for that movement.

3.5 Temporary and Permanent Data Saving

Data points get sent back to the Host in blocks during the experiment and the incoming data is scaled to the appropriate units. The following channels also having options to use the available bandwidth for greater sensitivity : 'Current 1', 'Current 2', 'Current 3', 'amplitude' and 'Phase'. This data is saved into a space and time efficient binary file, specifically the Technical Data Management System (TDMS) created by National Instruments. After the experiment has finished the user is prompted to save the data to a tab delimited data file. The binary TDMS file is not easily compatible with the analysis software used in the group, such as MATLAB or Origin, without additional programming, therefore LabVIEW handles the conversion when users want to save their data. Technically, the data is already saved in the TDMS file, however this file is designed to be temporary so when another experiment calls the Host, the current TDMS file is overwritten. If the user saves the data they will be presented with the full list of channels and can save only the ones they require, in order to minimise the size of the resulting tab delimited file. In addition, options to save each channel as a separate file and to save the a named copy of the TDMS are also offered, the former to simplify the transfer and analyse of large files and the latter to ensure no data is irretrievable.

3.6 Scanning Programs

All scanning programs are based on one of two basis modes, constant distance or hopping. In constant distance mode a probe approaches the surface and moves back and forth along the X axis the entire length of the scan and then up one user-defined step in the Y axis before moving the X axis again. Most scans move forward and backward on the same line before moving in the Y axis, this generates two maps one 'forward' and one 'reverse'. These two maps should be identical and any differences can be used to identify scan artefacts. Feedback type 4 is a proportional distance controller that maintains Z piezo position at a constant setpoint in any of the four feedback channels. The variable in the Waypoint cluster, 'Update Position Loop Wait Time', defines the

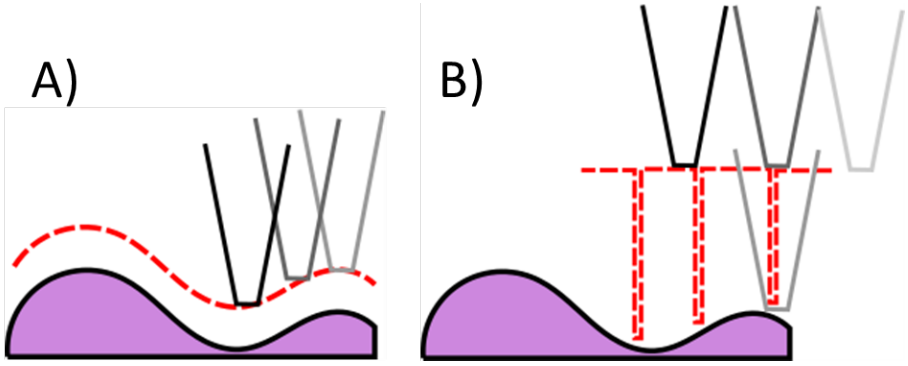

Figure 3.4: Schematic of A) Constance Distance mode and B) Hopping mode

frequency with which the Z position can change. The current value from the feedback channel is compared to the setpoint and the difference is multiplied by the proportional factor 'P' to produce the distance to move. This value is then coerced to a maximum defined with the variable 'max movement per update step' in the 'Change on Fly' cluster. A low maximum should ensure smooth movement of the Z piezo and accurate topography.

Constant distance mode has a number of drawbacks. The feedback channel must remain stable over the entire scan to avoid the probe crashing, which rules out a number of systems. The sample topography must be of a certain flatness otherwise there is a risk of the probe crashing if the feedback is not responsive enough. A solution to these problems is to use hopping mode. In hopping mode a 2D array of XY points to predetermined and the probe performs approaches to each of them. This method is considerable slower and has lower resolution so tends to be used only for samples that are too unstable for constant distance.

Experiments that require only the approach data can also be run using hopping mode. The individual hops can be far apart which makes this technique ideal for collecting many approach measurements on a single sample, automatically. The robust nature of the waypoint system results in the ability for a wide range of approach programs to be coded and run depending on the need. These options include the different feedback types on the approach, two setpoints, self referencing or running average setpoints and addition function-

ality can be included with each hop, such as a CV or current/time plot at each hop.

3.7 Example Program

As a specific example, let us consider the Approach Then CV program. The user interface is shown in Figure 3.5, it contains all the user input variables and several graphs. All UserVIs have the same look and feel as this example, but the specific variables and number of graphs are different. The block diagram is shown in Figure 3.6, section B holds the program in a continual loop until the user has set all their variables and pressed the Start button. Section C is where the program will run while the experiment is being executed using the Update Host SubVI until all the generated waypoints have been performed. Before that happens the waypoints are generated, for more complicated programs this would be hidden in a Sub VI, in a separate section. Section D simply ensures the probe is retracted from the surface and section E handles saving the data and resetting all the buttons.

The first waypoint is normally used to initialise all the parameters, in this example the Z piezo would be initialised at the top of it's range. The second waypoint would keep all parameters the same except the 'Z', 'Z vel' and 'Feedback Type'. The Z position is set to the bottom of the piezo range but the feedback type would be set to 1 so that when a user chosen threshold of one of the channels is met the movement is paused. The user can then decide if this is a false approach and unpause the program to continue descending or use the 'Stop Approach Start Scanning' button to manually move to the next waypoint and begin the CV. The third waypoint would still have the Z position set to the end of the piezo range but now the feedback type is set to '0 - No feedback', this would make the Z piezo extend to the limit of its range however, the boolean waypoint variable 'Move Z' will be set to false which results in the Z piezo being unable to move at all, keeping the probe stationary near the surface. The 'V' and 'V vel' variables control the applied voltage and the velocity the voltage will move at, respectively. Each waypoint after the second will change just the 'V' variable in order to construct the CV.

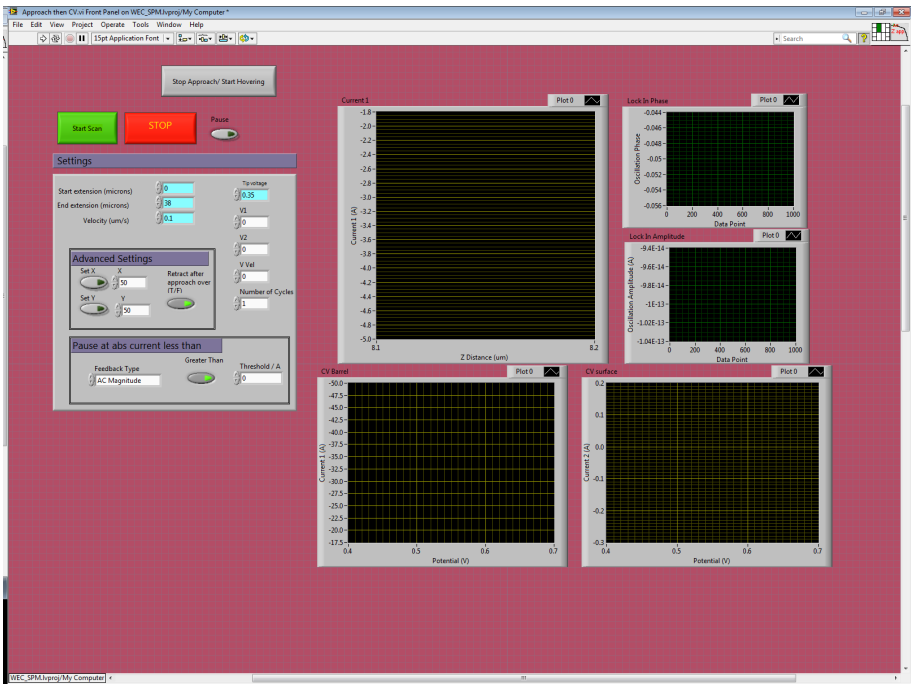

Figure 3.5: Front panel of the Approach Then CV program

3.8 Features

3.8.1 Real Time Data Viewing

During the experiment the recorded data can be viewed in real time. Due to the amount of graph options necessary to support all the possible experiments on the microscopes it is highly time consuming to handle all of them for every experiment. The solution to this problem is to use a subVI in the Host, called 'Real Time Data Viewer'. This subVI uses a stacked sequence structure to check for references for graphs in the current User VI, and only plots the ones a UserVI specifically calls for. All possible graph options can be seen in the 'Display Cluster' shown in Table 3.9. This results in time and memory efficient data plotting that can be changed for each User VI with ease. Blocks of data enter the subVI but only one point of each block of data is plotted, this misses up to thousands of data points and therefore the real time data is recommended to be used as a guide only. An exception is made of the 'Z vs t' graph, the main function of this graph is to monitor the Z piezo position

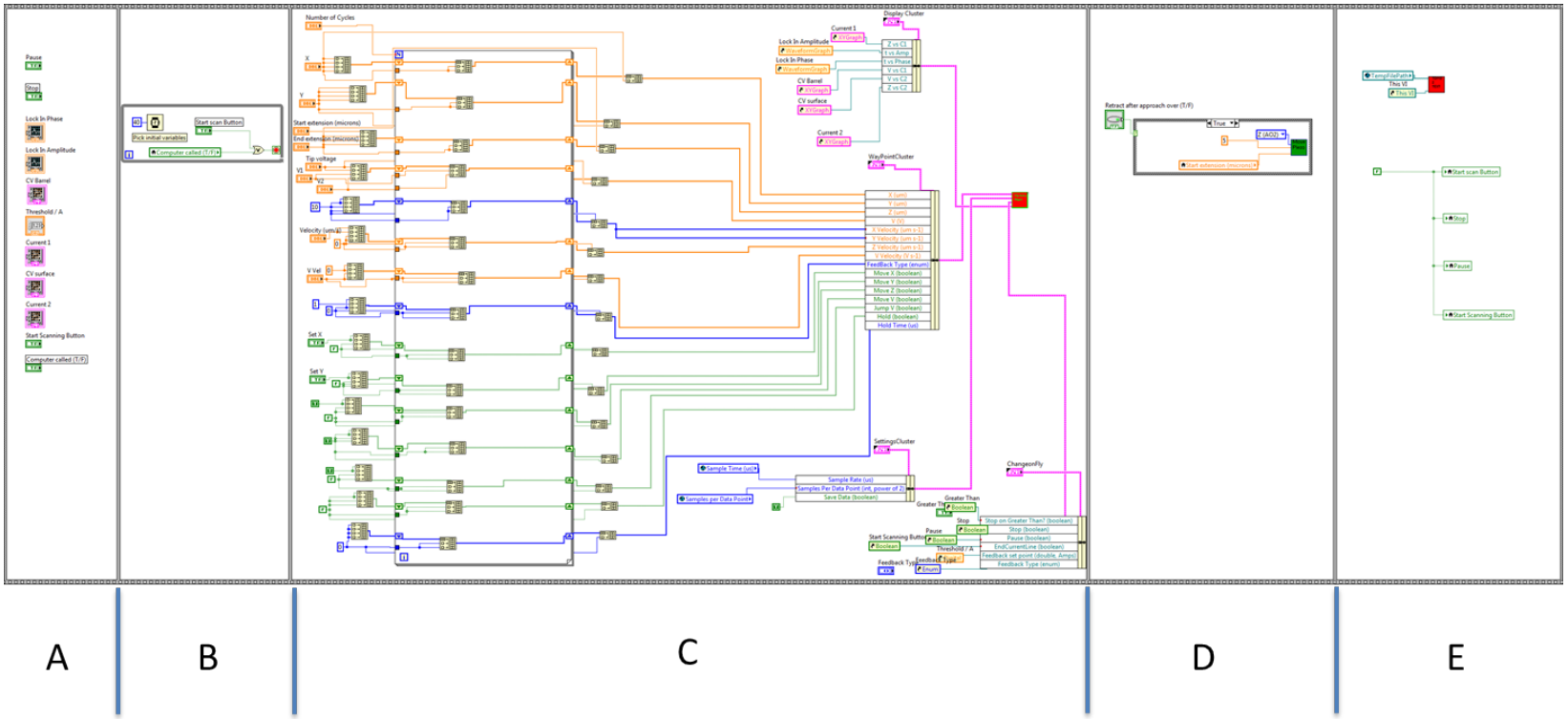

Figure 3.6: The block diagram of the Approach Then CV Program showing sections A) Initialise all the variables, B) Wait in a loop until the user has finished changing variables, C) Generate waypoints and run the experiments and D) Retract the probe E) Saves the data on the users command and resets all buttons.

modulation applied to the probe in some experiments. The data for this graph is sent to a buffer so the program will plot every data point to give an accurate view of the oscillations.

3.8.2 Ten Channel Mode

The project was designed to record all 15 channels for the entire duration of every experiment. At the standard data collection rates ('Sample Time' of 10 to 25 and 'Samples to Average' of 256 to 1024) this presented no problem as the TDMS file can expand to large sizes. However, as the projects progressed it became apparent that longer scans at high data collection rates were occasionally required. These would often cause memory issues as the TDMS overflowed and resulted in lost and corrupt data. It was found that the maximum number of data points capable of being collected was roughly 5 million data points for 15 channels (75 million double precision floating-point numbers). A number of solutions were possible, including upgrading the rig PCs. The fastest and cheapest solution was to implement a reduced channel mode. To disrupt as little of the original code as possible all the data collected on the Target and sent to the host and the real time data viewer remains unchanged. Only after the data has been displayed does the data array enter a simple boolean case structure, controlled by the 'Use 10 Channel' boolean in the Settings program, which cuts a ten channel subset of the data to reach the TDMS file. The 'Use 10 Channel' boolean is employed at the end of the host when the 'FPGA_to_Host' buffer is flushed and in the Convert Binary to TSV VI to direct the program to a new conversion options program and reduced list of channels.

The following channels were removed: Desired X, Y and Z Position, most scans do not use these channels as the real position information is available. 'Feedback Type' as most data analyse programs use 'Line Number' to divide section of data and not all users fully understand 'Feedback Type'. Finally, Voltage 2 as currently no scan qualifying for ten channel mode requires Voltage 2 to be changed during the scan. The settings file will contain the only value Voltage 2 will take during a scan. As a safe guard against accidental

use of ten channel mode a warning message has been programmed into the Host. Every single time the Host is called in ten channel mode the warning will appear regardless of UserVI. For this reason it is recommended that the ten channel mode is used only for the scan requiring reduced channels.

3.8.3 Self-Referencing Setpoint

In order to approach the probe to a surface, the user sets an absolute value as a setpoint either above or below the bulk value, then when the signal being used for the feedback crosses that setpoint value the program will stop the probe's downward movement, retract the probe and then move it to the next hop position. If you can assume a steady feedback signal, an absolute setpoint value ensures that the probe will reach the same distance away from the surface on every hop. However, in many instances a small amount of drift in the feedback signal can be observed, particularly in the phase recorded in bias modulation SICM. This results in either false approaches if the phase drifts towards the setpoint or probe crash if the phase drifts away from the setpoint. The self-referencing setpoint program provided a solution to this issue. Instead of choosing an absolute setpoint, the user chose a 'relative change' value. At the start of each hop, while the probe is fully retracted, an average value of the feedback signal is collected for this bulk environment. The 'relative change' value is then added and subtracted from the new average to generate two absolute setpoints, one higher, and one lower, with which to compare the feedback signal during the approach.

In addition to this mode of feedback, a more dynamic mode was required for certain approaches with a large amount of drift. A new feedback type which kept a running average of the feedback signal as the probe was moved towards the surface was implemented. To conserve space on the FPGA card it was preferable to avoid using buffers to hold the data to average. Instead, a variable of the sum of all data points to be averaged was kept, this average sum (A_{sum}) was updated for every new value (A_n) using the following equation,

$$A_{sum} = A_{sum} - \frac{A_{sum}}{N} + A_n \tag{3.3}$$

Where N is the number of data points to average. This approach kept down the memory used for this program, but is still accurate enough to provide stable feedback as the threshold would only register has having been broken if the new data point was significantly larger than the average of the previous N points.

3.8.4 Motorised Coarse Positioners

Advanced thermal stability hardware was added to the rigs, see Section 2.4.4 and with it the requirement to keep the Faraday cage door shut for long periods of time prior to experiments for the temperature inside to equilibrate. Repeatedly opening the Faraday cage to reposition the probe manually would disrupt the thermal stability inside. For easy repositioning on a larger range than the Z piezo every rig was retrofitted with a motorised coarse positioner. The motors used were 'Picomotors' from NewPort, UK. They consist of a screw held by two jaws and the jaws are connected to either end of a piezo. When a voltage is applied to the piezo the jaws move in opposite directions causing the screw to turn. Unfortunately, speed and distance can not be specified, only direction and activation can be controlled. The speed of the Picomotors depends on the how it was mounted and what is attached to it, therefore each Picomotor will move at a slightly different speed. To account for this, a scale factor is assigned to each Picomotor after calibration. The user can then enter the desired distance which is then multiplied by the scale factor, relative to the speed, to convert the distance to time. This is the time the Picomotor will be active for, however this is still an estimate as the scale factor is different for the up and down directions and Picomotors can drift away from their calibration. There is no feedback for the Picomotors so it is impossible to know exactly how far they have moved without recalibrating, for these reasons Picomotors are never used for scanning or precise movement.

3.8.5 Auto-Scaling Bipotentiostat

At the higher end of the sensitivity scale, the range of pico to femto amps, currents recorded in a single experiment can easier vary over many orders of magnitude. To allow a such an experiment to be recorded with a dynamic

sensitivity the auto-scaling bipots were developed by Alex Colburn. This is a piece of hardware that functions as a current follower but can change sensitivity on the fly. The sensitivity decreases once the current being recording reaches the maximum of the present setting and the sensitivity increases if the current drops to the bottom 10% of the detectable range. This ensures the current is always being recorded while using the available bandwidth most effectively. In order for the software to support this system an extra channel of information is passed from the auto-scaling bipot to the Target, then to the Host. This is the scale factor matching the sensitivity the bipot is using that changes in real time with the bipot. Once the current data reaches the Host it is divided by this scale factor to be converted to amps from whichever sensitivity was being used.

3.9 Acknowledgements

The construction of the physical rigs and the development of the codebase was a product of the effort of: Kim McKelvey, Neil Ebejer, Stanley Lai, Michael Snowden, Massimo Peruffo, Aleix Güell, Barak Aaronson, Ashley Page, Minkyung Kang, Alex Colburn, Julie Macpherson and Patrick Unwin. Funding for the development of this system has come through a number of sources including the ERC, EPSRC and MOAC DTC.

3.10 Tables

Table 3.1: Waypoint Cluster

Name	Unit	Data Type	Function
X	µm	Double	X piezo poistion
Y	µm	Double	Y piezo poistion
Z	µm	Double	Z piezo poistion
V	V	Double	V1 applied
V2	V	Double	V2 applied
X Velocity	$\mu m\,s^{-1}$	Double	Speed of X piezo movement
Y Velocity	$\mu m\,s^{-1}$	Double	Speed of Y piezo movement
Z Velocity	$\mu m\,s^{-1}$	Double	Speed of Z piezo movement
V Velocity	$V\,s^{-1}$	Double	Speed of V1 movement
V2 Velocity	$V\,s^{-1}$	Double	Speed of V2 movement
Feedback Type	na	U16	Mode of Z position control
Move X	na	Boolean	Allow X Piezo to move
Move Y	na	Boolean	Allow Y Piezo to move
Move Z	na	Boolean	Allow Z Piezo to move
Move V	na	Boolean	Allow V1 Voltage to move
Move V2	na	Boolean	Allow V2 Voltage to move
Jump V	na	Boolean	Jump V1 rather than ramp
Jump V2	na	Boolean	Jump V2 rather than ramp
Hold	na	Boolean	Allow use of Hold Time
Hold Time	µs	U32	Minimum waypoint time
Update Position Loop Wait Time (ticks)	ticks	U32	Update rate for positional control of Z
MovePicoMotorX	na	Boolean	Switch on Pico Motor X
MovePicoMotorY	na	Boolean	Switch on Pico Motor Y
MovePicoMotorZ	na	Boolean	Switch on Pico Motor Z
PicoMotor_x_direction	na	Boolean	Define direction Pico Motor X should move
PicoMotor_y_direction	na	Boolean	Define direction Pico Motor Y should move
PicoMotor_z_direction	na	Boolean	Define direction Pico Motor Z should move

Table 3.2: Settings Cluster and VI variables

Name	Data Type	Function
Settings Cluster		
Sample Rate	U32	Frequency with which the data collection loop on the Target is run
Samples Per Data Point	I16	Number of samples to average for one data point
Save Data	Boolean	Determines if the user we be presented the save data dialogue at the end of the experiment
DistanceToBulk	Double	Used in conjuction with feedback type 3 to retract the probe a set amount
Settings Vi		
Z Piezo maximum range	Double	Scales the incoming channel for the Z piezo to microns
X Piezo maximum range	Double	Scales the incoming channel for the X piezo to microns
Y Piezo maximum range	Double	Scales the incoming channel for the Y piezo to microns
Current Follower 1 (AI-3)	Enum	Scales the channel to amps, must match sensitivity of the physical current follower being used
Current Follower 2 (AI-4)	Enum	Scales the channel to amps, must match sensitivity of the physical current follower being used
Current Follower 3 (AI-6)	Enum	Scales the channel to amps, must match sensitivity of the physical current follower being used
Lockin Sensitvity	Enum	Scales the channel to amps, must match sensitivity on the physcial lockin
Expand	Enum	Scales the channel to amps, must match expand on the physical lockin
Current follower for AC?	Enum	Which current channel is being used for AC feedback
Percentage Offset	Double	Offsets the incoming Phase signal
Use 10 Channel	Boolean	Turns on 10 channel mode
Save Folder Path	File Path	Directs the data files when they are being saved

Table 3.3: Advanced Settings

Name	Data Type	Function
FPGA VI Reference	Reference	The Host can connect to the Target
FPGA Speed	I64	Variable to match the physical speed of the FPGA card
Host Path	File Path	Easily reference the Host Path
TempFilePath	File Path	Direct where the TDMS file saves to
Host to FPGA FIFO Length	I64	Defines the FIFO for passing waypoints to the Target
FIFO U64 per Waypoint	I64	Number of data points needed to specify one way-point
FIFO U64 per Sample	I64	Number of data points needed to pass a sample back from the card
FPGA RUNNING	Boolean	Indicates if the Host has successfully started the FPGA Card
Use Autoscaling Bipot on Current 2	Boolean	Turn on the autoscaling function when using the autoscaling hardware
Use Soft Piezo for AC Feedback	Boolean	Scale AC feedback to microns
Soft Piezo Range	Boolean	Range to scale AC feedback to for soft piezo
Channel Names	Array of Strings	The names the channels will be saved with
Points to Average	I16	Number of points averaged for FT 8
Picomotor ScaleFactor	Double	Scales distance to time for each Picomotor
Read 4th Current instead of Y Position	Boolean	Scales AI1 as a current rather than position
Current follower 4	Enum	Sensitivty to scale AI1 by if in Current Follower 4 mode

Table 3.4: Change on Fly Cluster

Name	Data Type	Function
Stop	Boolean	End the current experiments
Pause	Boolean	Temporarily pauses current waypoint
EndCurrentLine	Boolean	End current waypoint and move to the next
P	Float	Provide proportional feedback for constant distance scanning
max movement per update step	Integer	Limits Z movement to allow for smooth feedback in constant distance scanning
Feedback Type	Enum	Users can chose which channel to use for feedback
Feedback Type 2	Enum	Users can pick a second channel for feedback
Feedback Setpoint	Double	Programmatically activate Pause when Feedback Type channel passes this value
Feedback Setpoint 2	Double	Programmatically activate Pause when Feedback Type 2 channel passes this value
Stop on Greater Than?	Boolean	Determines the direction of Feedback Setpoint
Stop on Greater Than 2?	Boolean	Determines the direction of Feedback Setpoint 2
Voltage	Double	Update Voltage 1 output
Voltage 2	Double	Update Voltage 2 output

Table 3.5: Static Variables currently on the Target

Name	Data Type	Function
Buffer Loop Wait Time (tICKS)	U32	Update rate for data acquisition
2$\hat{}$(-n)	I16	Scaler for number of data acquisition points to average over
ExpandVelScaller X	I16	Velocity scaler for the movement in the X direction
ExpandVelScaller Y	I16	Velocity scaler for the movement in the Y direction
ExpandVelScaller Z	I16	Velocity scaler for the movement in the Z direction
ExpandVelScaller V	I16	Velocity scaler for the movement of the first potential
ExpandVelScaller V2	I16	Velocity scaler for the movement of the second potential
Change V on Fly	Boolean	Allow first voltage value to change on fly
Change V on Fly 2	Boolean	Allow second voltage value to change on fly
DistanceToBulk	I16	Distance to move when retracting the bulk
P2AvgMinus	I32	Negative number of points to average in order to divide the sum
P2AvgWhole	I32	Binary number of points to average
Host to FPGA FIFO	U64	Buffer for defining way-points, velocities and options.

Table 3.6: Dynamic variables current on the Target

Name	Data Type	Function
Upper limit of dZ	U64	Maximum movement in the Z direction for the feedback updates
P	Float	Gain for Feedback Type 4 movement
Feedback Threshold	U8	First feedback value
Feedback Threshold 2	I16	Second feedback value
Feedback Type	U8	Control to change what type of feedback signal is used for the first feedback value
Feedback Type 2	I16	Control to change what type of feedback signal is used for the second feedback value
GreaterThan	Boolean	Control to change how the feedback signal is compared to the first threshold value
GreaterThan2	Boolean	Control to change how the feedback signal is compared to the second threshold value
V on Fly	I16	First voltage value
V2 on Fly	I16	Second voltage value
EndCurrentLine	Boolean	Control for the user to end the current line
External Stop	Boolean	Command to stop the card
External Pause	Boolean	Command to pause the card

Table 3.7: Feedback Types

Label	Movement
1	Stop when setpoint threshold is reached and then pause
2	Stop when setpoint threshold is reached and then move to next waypoint
3	Move with respect to current position (mostly used for retracting)
4	Propotional feedback for constant distance control
5	Propotional feedback for constant distance control while storing positions in a buffer
6	Retrace the positions stored during feedback type 5
7	Propotional feedback for constant distance control, can also pause on secondary feedback
8	Collect an average then use feedback
9	Running average feedback
0	Move with no feedback

Table 3.8: Channel names

	Name	Connector
0	Real X position	AI0
1	Real Y position	AI1
2	Real Z position	AI2
3	Current 1	AI3
4	Desired X Position	AO0
5	Desired Y Position	AO1
6	Desired Z Position	AO2
7	Voltage 1	AO3
8	Current 2	AI4
9	FeedBack Type	na
10	LineNumber	na
11	Ampiltude	AI5
12	Phase	AI7
13	Current 3	AI6
14	Voltage 2	AO4

Table 3.9: Display Cluster

Name	Function
X	Current Value of X Piezo (AI0)
Y	Current Value of Y Piezo (AI1)
Z	Current Value of Z Piezo (AI2)
Amp	Current Value of Amplitude (AI5)
Phase	Current Value of Phase (AI7)
t vs Z	Graph of data point vs Z Piezo (AI2)
t vs C1	Graph of data point vs Currrent 1 (AI3)
t vs C2	Graph of data point vs Current 2 (AI4)
t vs C3	Graph of data point vs Current 3 Piezo (AI6)
t vs Amp	Graph of data point vs Amplitude (AI5)
t vs Phase	Graph of data point vs Phase (AI7)
t vs X	Graph of data point vs X Piezo (AI10)
t vs Y	Graph of data point vs Y Piezo (AI1)
Z vs C1	Graph of Z Piezo (AI2) vs Current 1 (AI3)
Z vs C2	Graph of Z Piezo (AI2) vs Current 2 (AI4)
Z vs C3	Graph of Z Piezo (AI2) vs Current 3 (AI6)
V vs C1	Graph of Potential 1 (AO3) vs Current 1 (AI3)
V vs C2	Graph of Potential 1 (AO3) vs Current 2 (AI4)
V vs C3	Graph of Potential 1 (AO3) vs Current 3 (AI6)
V vs Phase	Graph of Potential 1 (AO3) vs Phase (AI7)
V2 vs C1	Graph of Potential 2 (AO4) vs Current 1 (AI3)
X/Y/Z F	2D (X & Y) graph of Z Piezo (AI2) from the forward lines
X/Y/Z R	2D (X & Y) graph of Z Piezo (AI2) from the reverse lines
X/Y/C1 F	2D (X & Y) graph of Current 1 (AI3) from the forward lines
X/Y/C1 R	2D (X & Y) graph of Current 1 (AI3) from the reverse lines
X/Y/C2 F	2D (X & Y) graph of Current 2 (AI4) from the forward lines
X/Y/C2 R	2D (X & Y) graph of Current 2 (AI4) from the reverse lines
X/Y/C3 F	2D (X & Y) graph of Z Piezo (AI2) from the forward lines
X/Y/C3 R	2D (X & Y) graph of Z Piezo (AI2) from the reverse lines
Hop X/Y/Z	2D (X & Y) graph of Z Piezo (AI2) from hopping scans
Hop X/Y/C1	2D (X & Y) graph of Current 1 (AI3) from hopping scans
Hop X/Y/C2	2D (X & Y) graph of Current 2 (AI4) from hopping scans
Hop X/Y/C3	2D (X & Y) graph of Current 3 (AI) from hopping scans
NumberOfLines	Variable to define number of lines in Line Scan graphs
um Per Pixel	Variable to define resolution of Line Scan graphs
um Per Line	Variable to define distance between lines of Line Scan graphs
X Center	Variable for defining center of 2D scan graphs
X Width	Variable to define width of Line Scan graphs
Y Width	Variable to define height of Line Scan graphs
Hopping Distance	Variable to define distance between hops in Hopping Scan graphs

Chapter 4

Dual-Barrel Conductance Micropipette as a New Approach to the Study of Ionic Crystal Dissolution Kinetics

A new approach to the study of ionic crystal dissolution kinetics is described, based on the use of a dual-barrel theta conductance micropipette. The solution in the pipette is undersaturated with respect to the crystal of interest, and when the meniscus at the end of the micropipette makes contact with a selected region of the crystal surface, dissolution occurs causing the solution composition to change. This is observed, with better than 1 ms time resolution, as a change in the ion conductance current, measured across a potential bias between an electrode in each barrel of the pipette. Herein, we study the dissolution of NaCl as an example system, with dissolution induced for just a few milliseconds, and estimate a first-order heterogeneous rate constant of $(7.5 \pm 2.5) \times 10^{-5}$ $\mathrm{cm\,s^{-1}}$ *(equivalent surface dissolution flux ca. 0.5* $\mu\mathrm{mol\,cm^{-2}\,s^{-1}}$ *into a completely undersaturated solution). Ionic crystals form a huge class of materials whose dissolution properties are of considerable interest, and we thus anticipate that this new localized microscale surface approach will have considerable applicability in the future.*

4.1 Introduction

Crystal dissolution processes are of ubiquitous importance across many areas of natural science,[100,101,180] playing a key role in many practical applications, such as in oral drug delivery[103,181] and in a diverse range of industries from food[182] to construction.[105] Consequently, methods for studying crystal dissolution are hugely valuable, and considerable attention has been given to the development of techniques that can provide quantitive information on the kinetics and mechanisms.[112] Crystal dissolution rates typically depend on the degree of undersaturation at the crystal/liquid interface,[106] and this is broadly governed by two competing processes in series: (i) surface phenomena, such as surface diffusion and the detachment of ions or molecules at the crystal surface; and (ii) mass transport of material from the interfacial region to the bulk solution. Clearly, mass transport must be sufficiently high and well-defined to enable the kinetics of the surface processes to be measured. Additionally, because different surfaces of a crystal, and particular sites on a surface, may have very different dissolution characteristics[183] the most informative studies are those that target well-defined and characterizable surfaces.

The need for both well-defined mass transport and well-defined surfaces has been addressed to some extent by hydrodynamic methods, including the rotating disc[132] and channel flow cell.[120,184] These techniques deliver well-defined mass transport rates to the crystal surface and so enable intrinsic surface rates to be determined. While the rotating disc method typically follows dissolution reactions by monitoring the chemical composition of the bulk solution, the channel flow cell system allows real time electrochemical monitoring of the dissolution rate via an electrode positioned downstream of the crystal.[120] The composition of the effluent from flow cells can also be analyzed with a range of quantitative analytical techniques.[136,185] The primary limitation of these hydrodynamic systems is that, typically, they require crystalline material in the form of large flat surfaces, or samples embedded in a support material, and the measured dissolution rate is averaged over large areas of the surface, which potentially hides local intrinsic rate differences.[112]

A different approach to dissolution and growth measurements involves the use of scanning probe microscopy techniques, for example, *in-situ* atomic force microscopy (AFM),[141,150,186–188] and scanning electrochemical microscopy (SECM).[183] While *in-situ* AFM has provided major insights into dissolution processes there are some practical drawbacks. For instance, the process must be slower than the speed of the AFM scan and the probe may perturb the hydrodynamics and diffusion in AFM flow cells[189] making the description of mass transport rather difficult. In general, there are often significant differences between dissolution rates measured via AFM and other techniques for the same material and conditions,[122,189] an issue which requires further attention.

SECM studies employ an ultramicroelectrode positioned close to the surface of a crystal to induce dissolution and probe the associated fluxes.[112,155,183] Advantages of this approach, which has also been implemented in a combined SECM-AFM format,[190] are that dissolution is targeted at specific regions of a crystal surface and the dissolution time can be controlled very precisely (millisecond time resolution) by the electrode.[113,155,183] In addition, one can also study materials with a very wide range of solubilities.[113,183] However, SECM-related methods have, hitherto, largely been limited to dissolution processes that can be triggered by the oxidation/reduction of the constituents ions or molecules of the crystal. Potentiometric electrodes have also been employed in an SECM format to measure dissolution fluxes, although without quantitative analysis,[45] and with a dual-channel nanoscale SECM-scanning ion conductance microscopy (SICM) probe to permit the high level quantitative analysis of experimental topographical and chemical images.[84]

Herein, we introduce a dual-barrel theta micropipette for rapid, multiple point conductance measurements of dissolution kinetics across a crystal surface, via meniscus contact. In other applications, dual-barrel micropipette techniques have demonstrated high spatial resolution,[85,87] the possibility of measuring fast electrochemical kinetics on electrode surfaces,[93] and the ability to draw patterns on surfaces.[87,97] The meniscus at the end of the pipette creates a well-defined microconductance cell on a substrate,[87,90] without the pipette, itself, touching the surface. In general, dual pipette techniques greatly enhance the scope and information content of meniscus contact techniques for

deposition[85,97] and dissolution processes,[85] compared to single pipette-based meniscus contact methods.[67,191–193]

We demonstrate the capabilities of the technique by studying the dissolution of the ionic crystal NaCl in aqueous solution as a model system. This system is fundamentally interesting as it is characterized by high solubility (6.1 M)[194] and relatively large dissolution fluxes which makes studies with techniques that require immersion of the solid in a bulk solvent somewhat challenging.[195] NaCl dissolution is also of practical importance in relation to developing anti-caking technologies in the food industry.[104,182,196] Since conductance measurements have been widely used for dissolution studies on a macro-scale in suspensions,[197] we envisage that the dual-barreled conductance micropipette described herein could be widely adopted for the study of dissolution (and growth) processes. More generally, the work in this chapter further enhances a growing family of quantitative pipette-based imaging techniques.[64,198–203]

4.2 Experimental Section

SiO_2 substrates were cut from Si/SiO_2 wafers (IDB Technologies) and were cleaned by plasma ashing (K1050X, Emitech) immediately prior to use. The NaCl crystals were formed by evaporation in air of a droplet (∼100 µl) of saturated NaCl solution (6.1 M) deposited on a glass slide (Menzel-Gläser, Thermo Scientific). The crystals grew with a cubic morphology with the (100) faces exposed.[204] The crystal edge length was typically 300-500 µm. Data were typically recorded at 25.2 kHz. The instrumentation was operated in an air-conditioned laboratory at a temperature of 22 ± 1 °C.

4.2.1 Analytical Methodology

The current measured between the two quasi-reference counter electrodes (QRCEs) depends on the voltage applied between them, which was 0.4 V, and overall resistance of the theta pipette cell. While in air, a small meniscus is formed at the tip of the pipette (see schematic in Figure 4.1(C)(i)), resulting in high

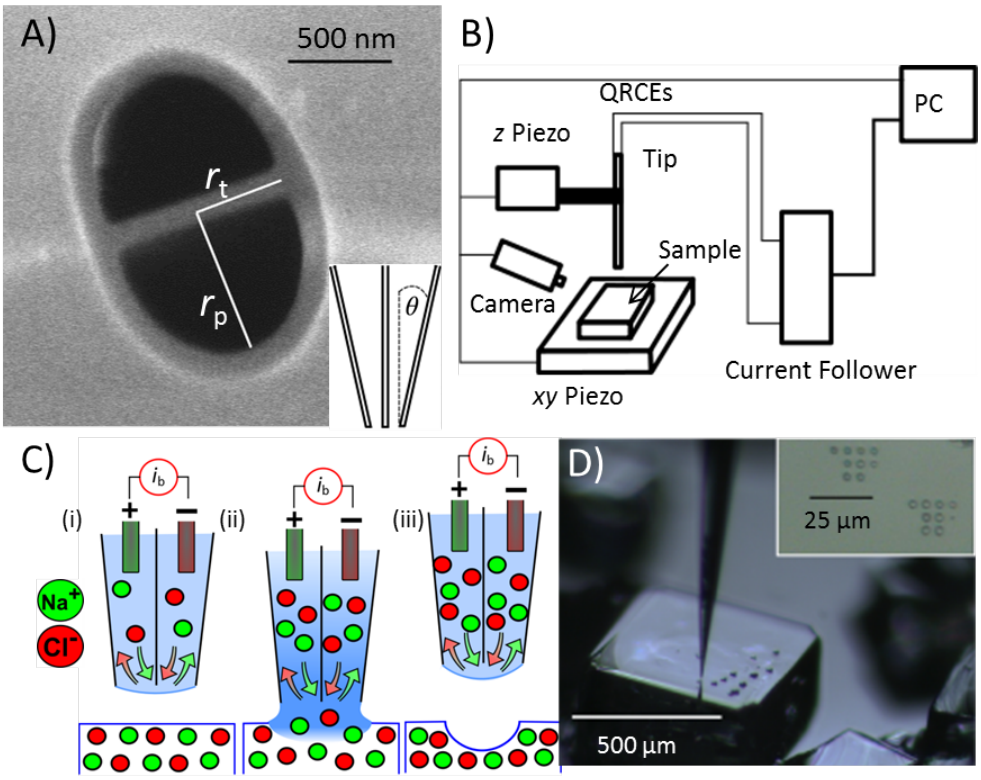

Figure 4.1: (A) FE-SEM image of the end of a typical pipette with the dimension perpendicular to the septum (r_p), and parallel to the septum (r_t) labeled. The inset is a sketch of the side view of a pipette showing the semi-angle (θ). (B) Schematic of the experimental setup. The sample is mounted on an XY piezoelectric positioner, while the pipette is on a Z piezoelectric positioner. The current is measured by a home-built current follower and all components are controlled, and data recorded, by a PC (see experimental section for details). (C) Schematic of the dissolution experimental procedure: (i) pipette held in air; (ii) dissolution occurs upon contact of the meniscus with the crystal for a defined short period; (iii) pipette is retracted, breaking meniscus contact with the surface. (D) An optical microscope image taken *in-situ* from a side-mounted camera of a dual-barrel conductance micropipette aligned above a NaCl microcrystal where a series of dissolution pits can be seen. Inset: optical microscope image of two arrays of NaCl dissolution pits.

resistance, and consequently only a small current is detected (*vide infra*).[85] The experimental procedure was to approach the pipette towards the surface at a speed of 0.1 µm s^{-1} until the meniscus at the end of the pipette wetted the substrate surface, without the pipette itself making contact. This phenomenon was readily detected, because when the meniscus wets the surface its thickness increases, resulting in the meniscus resistance decreasing, as manifested by a sharp increase in the ion conductance current (Figure 4.1(C)(ii)). The abrupt change in conductance current (due to a jump to contact of the meniscus with the surface)[90] was sensed and used to automatically stop the motion of the pipette, which was then held in a fixed position for a predefined etch time (*vide infra*).

Dissolution was promoted by the use of a greatly undersaturated sodium chloride solution in the pipette. The resulting ionic dissolution flux from the crystal surface into the solution in the meniscus and pipette further decreased the resistance between the two QRCEs and hence increased the current over time. In fact, as we show below, the barrel current-time response is related to the flux of ions from the crystal surface. Once the pre-defined dissolution time had elapsed, the pipette was withdrawn at a speed of 100 µm s^{-1} to ensure that contact between the meniscus and substrate was broken abruptly (Figure 4.1(C)(iii)). Repeat measurements were performed by laterally repositioning (typically by 5 µm) the pipette over a new section of the microcrystal surface. Figure 4.1(D) shows an image taken *in-situ* during a typical experiment using a camera in which the pipette and a series of dissolution pits can be seen. The pits formed using this procedure were characterized by optical microscopy (BH-2, Olympus), as shown in the inset of Figure 4.1(D), and AFM (Veeco BioScope Catalyst Atomic Force Microscope, Bruker) in Scan Asyst mode with a Nanoscope V controller (Veeco), using Sb doped Si tips (SNL-10, Veeco).

4.2.2 Finite Element Method Modeling

The commercial finite element method (FEM) simulation package Comsol Multiphysics (v4.3, Comsol AB) with LiveLink for Matlab (R2011a, Mathworks) was used for all simulations. Simulations were performed using a 3D geomet-

ric domain of the meniscus and tip of the pipette, similar to that described previously,[90] and shown in Figure 4.2. The variation of the ionic conductance current with respect to time, due to the dissolution process, was calculated in 2 stages. In stage 1, the time-dependent Na^+ and Cl^- concentrations were determined from a diffusion-only simulation.

In stage 2, the corresponding steady-state electric field at each time step was determined and from this the conductance current between the barrels, i_b, was calculated. The diffusion-only mass transport of Na^+ and Cl^- was reasonable for the experimental conditions of interest because the applied bias was relatively small.[90] Moreover, we focus on short time measurements (<15 ms) where concentration gradients are relatively large in the region of interest (vicinity of the meniscus and pipette tip), and the impact of the electric field in this region is rapidly diminished by the flood of ions from the crystal surface due to dissolution. Focusing on the short time behaviour also allowed us to reasonably assume a static surface, although moving boundaries could be incorporated in the future, as we have shown for recent microscale dissolution studies by other methods.[155] The time-dependent concentration profiles, within the pipette tip, are determined by solving Fick's second law:

$$\frac{dc}{dt} = D_B \nabla^2 c \tag{4.1}$$

where t, c, and D_B are the time, concentration and diffusion coefficient, respectively. Because dissolution is stoichiometric and the solution has to be electroneutral, we considered a one species problem, with the mean diffusion coefficient of Na^+ and Cl^- (16.83 x 10^{-6} cm^2 s^{-1}).[205] The upper faces of the pipette barrels (boundaries 1 and 2 in Figure 4.2(B)), representing bulk solution, were defined by,

$$c = c^* \tag{4.2}$$

where c* was the starting concentration of the NaCl solution (5 mM). The rate of dissolution at the substrate surface (boundary 5) was assumed to be first-order with respect to the degree of undersaturation at the crystal solution interface,

$$\mathbf{n}.\mathbf{N} = k(c_{sat} c) \tag{4.3}$$

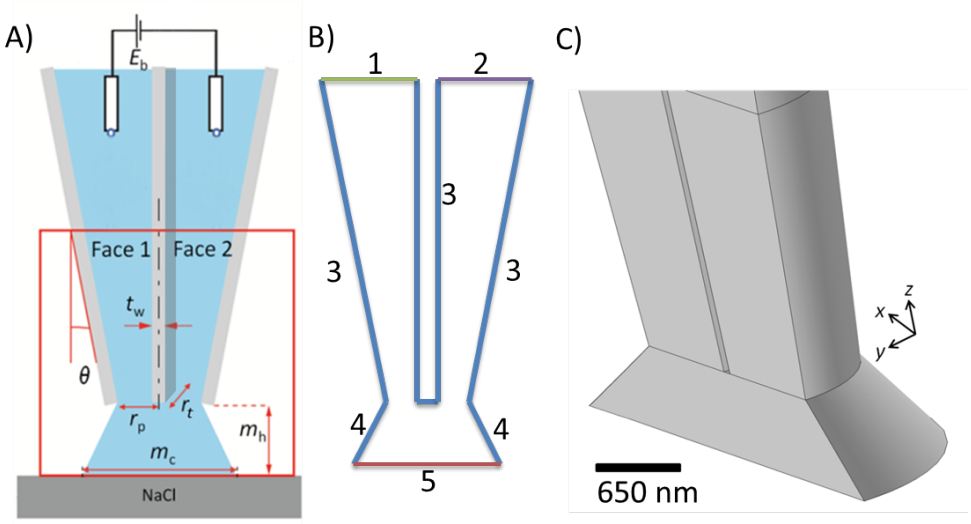

Figure 4.2: A) Schematic of a pipette in contact with a NaCl crystal via a meniscus. The red box is the simulation domain with key parameters being the potential difference between the barrels (E_b), the septum width (t_w), semi-angle (θ), pipette radius (r_p), meniscus contact diameter (m_c) and meniscus height (m_h). B) 2D sketch of the simulation domain where boundaries 1 and 2 have an applied potential imposed together with bulk concentrations, 3 and 4 are boundaries with no normal flux and 5 has a flux boundary condition, as it represents the crystal surface. C) 3D representation of the simulation domain.

where $\mathbf{n}$ is the inward unit vector normal to the surface, $\mathbf{N}$ is the flux vector, k is a first-order dissolution rate constant (cm s^{-1}) and c_{sat} was the saturation concentration (6.1 M).[194] In fact, as shown herein, c_{sat} is extremely large compared to c near the interface, so that we essentially measure the flux as kc_{sat}. The pipette walls (boundary 3 in Figure 4.2(B)) and the meniscus/air interface (boundary 4) were considered to have no flux.

Concentration profiles were output every 0.1 ms from $t = 0$ s to $t = 15$ ms, and each concentration profile was subsequently used as a basis to calculate the electric field, and therefore the corresponding conductance current in stage 2. The potential field within the pipette and meniscus was determined at each time step by solving the governing equation for a steady-state electric field:

$$\mathbf{J} = \sigma \nabla \phi \tag{4.4}$$

where **J** is the current density vector, σ is the conductivity and ϕ is the potential, while ensuring the conservation of current within the simulation domain:

$$\nabla \mathbf{J} = 0 \tag{4.5}$$

The conductivity of the solution within the pipette and meniscus was determined from:[206]

$$\sigma = (z_{Na^+}^2 u_{Na^+} c + z_{Cl^-}^2 u_{Cl^-} c) \tag{4.6}$$

where z_i is the charge and u_i is the ionic conductivity of species i, ($u_{Na^+} = 76.31$ S cm^2 mol^{-1} and $u_{Cl^-} = 50.08$ S cm^2 mol^{-1}). The conductance current (i_b) can be calculated from the current density vector (**J**) by taking the surface integral across a cross-section of one of the barrels. For the electric field calculations, the upper faces of the pipette barrels (boundaries 1 and 2 in Figure 4.2(B)) have an applied bias between them, mimicking the experimental conditions.

4.3 Results and Discussion

4.3.1 Ion Conductance Measurements

The localized dissolution of NaCl crystals was carried out using a pipette, with dimensions defined in Figure 4.1(A), containing NaCl solution (5 mM). A typical experimental conductance current-time trace is shown in Figure 4.3(A), with the corresponding pipette position below, shown schematically, with respect to the crystal surface. Figure 4.3(B) shows traces for 4 dissolution times of 3, 10, 15 and 18 ms. For each meniscus contact time there are multiple overlaid current-time traces (between 2 and 12 runs for each etch time) and each trace was recorded in a separate region of the surface. These data serve to highlight the high reproducibility of meniscus landing and localized crystal dissolution. It should be noted that between dissolution experiments the current decays back to the original value. When the pipette was in air, t <0, the conductance current, i_b, had a low value *ca.* 0.1 nA, because the meniscus at the end of the pipette was rather thin, causing high resistance.[90]

During this period the pipette was moving towards the surface at a speed of 0.1 µm s^{-1} as illustrated in Figure 4.3(A)(i). The liquid meniscus

contact with the NaCl surface at $t = 0$ is observed as a jump to contact wetting of the surface causing the current to abruptly increase by approximately 1 order of magnitude. This is due to the decreased resistance from the larger meniscus as illustrated in Figure 4.3(A)(ii), and manifested in the conductance current-time traces at $t = 0$ in Figure 4.3(B). This phenomenon has been documented for other systems studied by the related SECCM technique.[85,90] The increase in current was detected by the control program and used to stop the pipette approach, leaving the meniscus stationary on the surface, as illustrated by the constant height of the vertical position of the pipette, shown in Figure 4.3(A)(ii). After the initial current jump there was a gradual increase in the conductance current with time, attributed to the release of ions from the NaCl crystal into the meniscus. After a predefined time, the pipette was moved away from the NaCl surface at a speed of 100 $\mu m\,s^{-1}$, which broke the meniscus contact with the crystal and caused the current to fall rapidly as the meniscus shrank in size when detached from the surface (Figure 4.3(A)(iii)).

As explained above, there was a large degree of reproducibility in the currents recorded in different spots of the crystal, as the curves for a particular time overlap to a high degree. In addition, the traces at different times overlap up until the point at which meniscus contact with the crystal surface was broken (Figure 4.3(B)). Before these current-time traces were analyzed, the current response associated with initial contact of the meniscus with the surface, and the establishment of a stable meniscus contact was assessed. This was done by comparing the response for meniscus contact to a NaCl crystal to that for an inert SiO_2 surface, as shown in Figure 4.4. On SiO_2 the rise time (defined as the time for the current to change from 10% to 90% of the maximum current signal) was 0.3 ms. This time is an order of magnitude longer than the rise time of the current follower used for the measurement and so this rise time was essentially associated with the meniscus stabilizing on the surface. This meniscus stabilization time is also at least an order of magnitude shorter than the dissolution periods considered.

In order to compare the conductance current of NaCl dissolution to the simulation results, it was necessary to account for the effect of meniscus stabilization. This was reasonably accomplished by subtracting the current

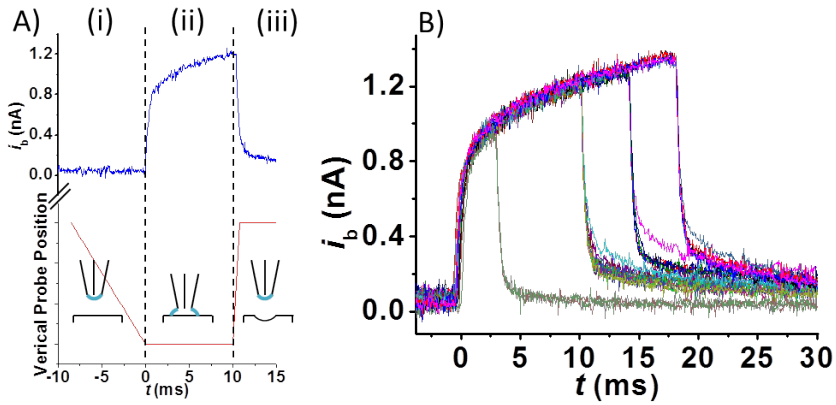

Figure 4.3: A) Plot of barrel conductance current - time above a schematic of the corresponding vertical pipette position during a dissolution experiment. (i) The pipette is moving down toward the surface in air and the barrel current is small, due to a tiny meniscus. (ii) The meniscus lands as a jump to contact and the pipette stops moving. The crystal dissolves causing a further increase in the barrel current. (iii) The pipette is drawn up quickly, breaking the meniscus contact and causing the current to drop as the meniscus returns to its original shape. B) Current - time plots of multiple repeat measurements of dissolution pits at different spots on NaCl. The dissolution times are 3 ms (2 repeats), 10 ms (12 repeats), 15 ms (12 repeats) and 18 ms (6 repeats)

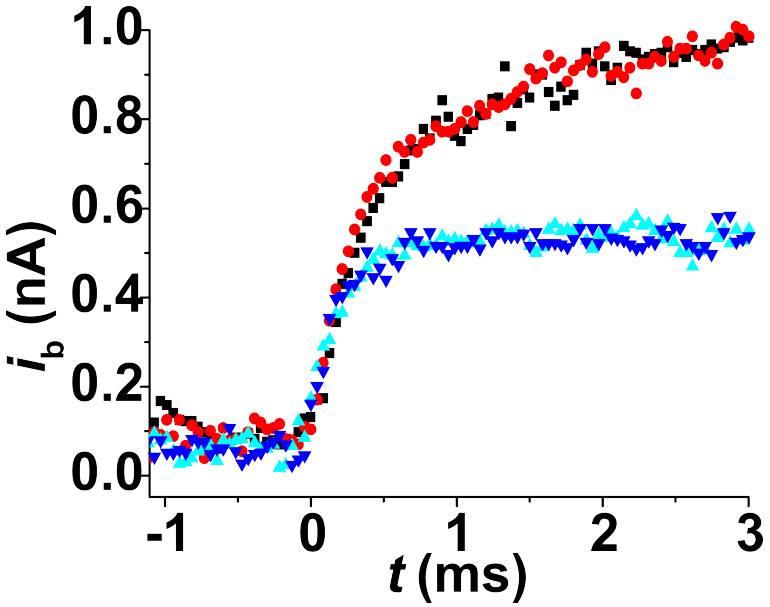

Figure 4.4: Conductance current-time plot of the meniscus landing on SiO_2 for two runs (dark blue ▼ and light blue ▲)and two for NaCl (red • and ■). Time $t = 0$ s is defined as the time when the meniscus lands on the surface of the crystal.

response on SiO_2 from the response on NaCl, thereby leaving only the change in current with time that was a direct result of crystal dissolution. Both substrates are expected to have similar wettabilities by water, and we have shown that the degree of wetting of a substrate by the meniscus from a micropipette is similar on quite a wide range of substrates, because this is controlled not only by the substrate but also by the pipette outer wall, which is silanized.[85,90,93,97]

4.3.2 Simulations and Modeling

To deduce dissolution kinetics and fluxes, we used the model outlined in Section 4.2.2. Typical simulated concentration maps are shown in Figure 4.5 for a pipette of dimensions: $m_h = 300$ nm, $r_p = 0.65$ µm, $r_t = 0.4$ µm, $\theta = 8°$, $k = 5 \times 10^{-5}$cm s^{-1} and $m_c = 3.2$ µm. The mensicus contact area, m_c, was determined from measurement of dissolution pit dimensions by AFM and represents a reasonable upper limit on the effective contact area of the meniscus with the crystal surface due to further dissolution occurring after the pipette has been withdrawn. The concentration profile, shown in Figure 4.5(A), shows that at t

= 0 s the pipette is filled homogenously with the bulk solution (5 mM). At t = 5 ms the dissolution of NaCl leads to an appreciable increase of the concentration of Na^+ and Cl^- ions in the meniscus and the mouth of the pipette, leading to an increase in conductance current (vide supra) and corresponding smaller electric field gradient in this region of the pipette seen in Figure 4.5(B). At t = 10 ms further dissolution has occurred, with ions pumped into the meniscus and transported into the pipette. The concentration profile of Na^+ and Cl^- ions extends further up the pipette as time increases which results in a further increase in the conductance current and concomitant change in the electric field. However, even for the longest dissolution time considered, the concentration in the meniscus near the crystal surface reaches a maximum of <1% of the saturated value. This highlights that, with these parameters, typically representative of experiments, the dissolution process is essentially under surface kinetic control. The simulations were run for a wide range of dissolution rate constants; see Figure 4.6. As the dissolution rate constant increases, the magnitude of the conductance current, as a function of time, increases.

It can be seen that the technique is sensitive to a wide range of dissolution rate constants with values of k up to *ca.* 0.1 $cm\,s^{-1}$ reasonably accessible, above which it is difficult to distinguish the surface rate constants from the mass transport limit. The relatively high rate constant amenable to characterization is a consequence of the intrinsically high mass transport rates inherent in the tapered micropipette design.[90,198] Figure 4.6 shows background subtracted experimental current-time curves for two runs along with a range of simulated currents for different dissolution rates. The experimental data were typical of more than 20 traces run (see Figure 4.3(B)). There was reasonably good agreement between the experimental data and the simulated data with a fit to $k = 5 \times 10^{-5}$ $cm\,s^{-1}$ for longer times and $k = 1 \times 10^{-4}$ $cm\,s^{-1}$ at t <3 ms.

For this system we can now assign a value of intrinsic dissolution rate of $(7.5 \pm 2.5) \times 10^{-5}$ $cm\,s^{-1}$ and an intrinsic surface-controlled dissolution flux (kc_{sat}) of *ca.* 0.5 $\mu mol\,cm^{-2}\,s^{-1}$. The kinetic constant and flux is of the same order as found in a previous study (10×10^{-5} $cm\,s^{-1}$) for compacted disk samples[119] confirming the validity of the technique. Other ionic crystals have

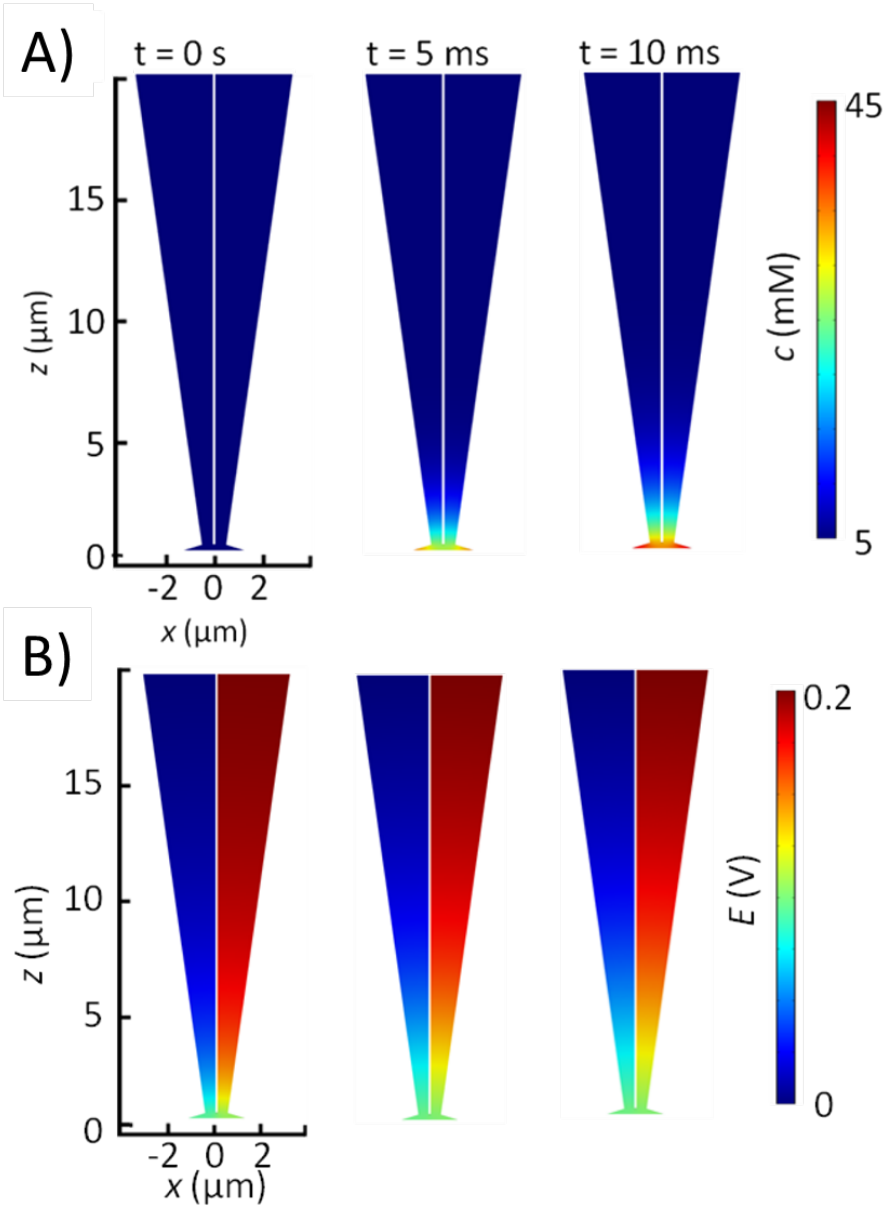

Figure 4.5: FEM model results showing (A) the concentration of NaCl and (B) within a dual-barrel conductance micropipette at time steps:(A) 0, 5 and 10 ms for a tip of dimensions: $m_h = 300$ nm, $r_p = 0.65$ µm, $r_t = 0.4$ µm, $\theta = 8°$, $k = 5 \times 10^{-5}$ cm s^{-1} and $m_c = 3.2$ µm.

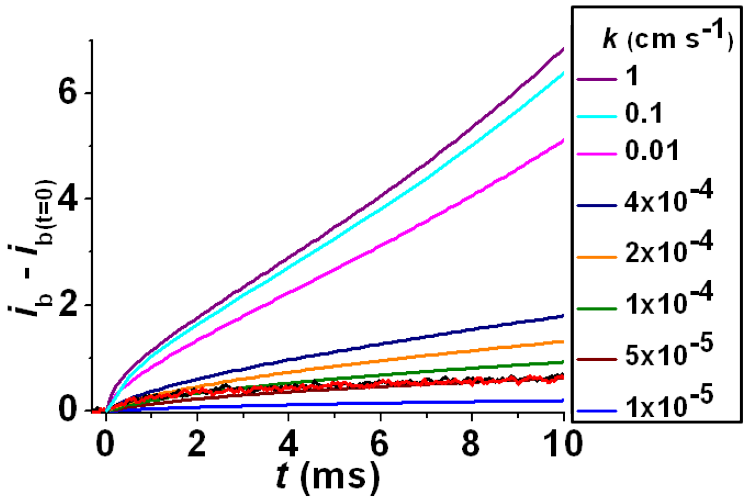

Figure 4.6: Simulated conductance current-time plots for a pipettes of identical dimensions as (A) on a NaCl substrate with a range of k values. For comparison, 2 sets of typical experimental data for shown (red and black) matching $k = 1 \times 10^{-4}$cm s^{-1} <3 ms and $k = 5 \times 10^{-5}$cm s^{-1}

a wide range of dissolution rates, including KF which has a reported rate constant of 3×10^{-8} cm s^{-1} [207] and $CaSO_3$ which, in its common form of gypsum, has a dissolution rate of 6×10^{-4} cm s^{-1}.[185] We assumed a meniscus height of 300 nm, as deduced from a control measurement on SiO_2 and guided by previous related SECCM studies.[45,84,85,87,90,93,97] However, we investigated the impact of the meniscus height on the current response through further simulations, and found it to be negligible over a reasonable range of values, as shown in Figure 4.7. This meniscus height insensitivity arises from the fact that the concentration gradient of Na^+ and Cl^- extends up into the barrels, (see Figure 4.6(A)) resulting in the meniscus height from the surface representing only a small percentage of the overall distance of the diffusion profile. This demonstrates that the important geometric parameters in the model are the footprint of the meniscus on the surface, the size and shape of which are easily determined from SEM. The meniscus contact area was determined from the AFM of the dissolution pits (Figure 4.8), but given some redistribution of material in the droplet left on the surface, this represents an upper limit for the meniscus contact area, and thus a lower limit on the intrinsic dissolution rate.

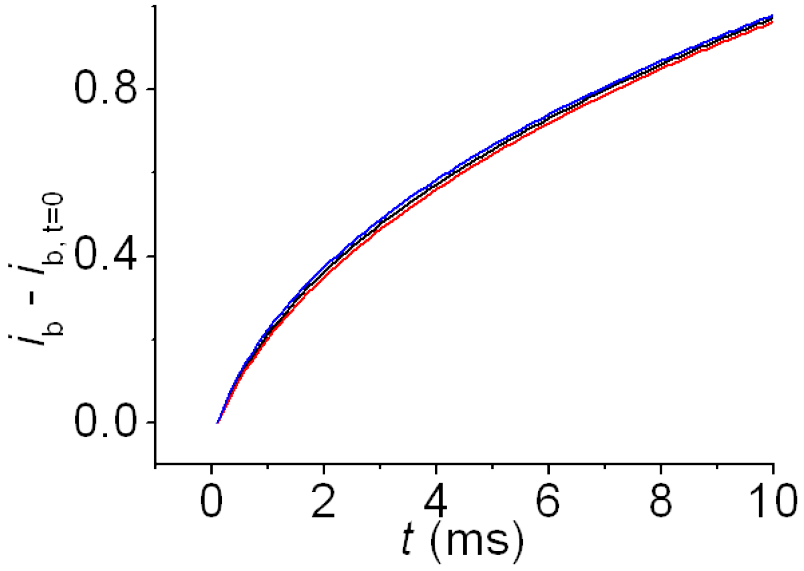

Figure 4.7: Current-time plots of a range of meniscus heights(m_h) compared for a tip of dimensions: $m_h = 300$ nm, $r_p = 0.65$ µm, $r_t = 0.4$ µm, $\theta = 8°$, $k = 5 \times 10^{-5}$cm s^{-1} and $m_c = 3.2$ µm 0.5µm(blue line), 0.4 µm (black line) and 0.3 µm (red line). The results show a minimal change in the current-time plots.

4.3.3 Dissolution Pit Morphology Measurements

AFM measurements were performed prior to and after dissolution experiments to characterize the crystal surface, and the size and shape of pits formed by dissolution. AFM images were analyzed using SPIP 6.0.10 (Image Metrology). Prior to dissolution, the NaCl crystals showed no major features and had a surface roughness of ∼10 nm. After dissolution, pit features were clearly visible, and AFM was used to measure the morphology and dimensions. Figure 4.8 shows an AFM image of nine typical pits, each produced with a dissolution time of 10.0 ± 0.2 ms. Dissolution pits were circular and had an average diameter of 3.2 ± 0.1 µm at 10 ms. The diameter did not change significantly with dissolution time, with a diameter of 3.10 ± 0.05 µm at 3 ms and 3.3 ± 0.1 at 15 ms. Furthermore, the depths of the pits showed a relatively minor dependence on etch time, with depths (edge to base), of 105 nm (3 ms), 131 nm (10 ms), 136 nm (15 ms).

This insensitivity of the pit geometry to dissolution time suggests that the pits are a consequence of the solution left behind when the meniscus detaches, as used deliberately in some nanocrystal growth studies,[208] as discussed below. It is interesting to compare the dissolution pit depths to the values that might be expected based on the conductance measurements. A surface-controlled dissolution flux *ca.* 0.5 µmol $\mathrm{cm}^{-2}\,\mathrm{s}^{-1}$ suggests that the pit depths should be much smaller than seen *ca.* 0.4 nm (3 ms), 1.3 nm (10 ms), 2.0 nm (15 ms) using the known density of NaCl of 2.17 $\mathrm{g\,cm}^{-3}$ (and formula mass, 58.44 $\mathrm{g\,mol}^{-1}$.[205] Closer inspection of the pits in Figure 4.8 indicates that not only has much more substantial dissolution occurred, but also that there is reprecipitation of material around the top surface of the pit. A reasonable explanation for this morphology and the much deeper pits than expected is that solution is retained on the locally dissolving crystal surface as meniscus contact is broken and dissolution continues in the highly undersaturated solution (*videsupra*) along with evaporation of the droplet. For the present study this is advantageous as it marks the likely (maximum) surface area covered by the droplet. There may be some lateral dissolution of the surface by the retained droplet, but the extent of this would be of the order of the final pit depth (*ca.*

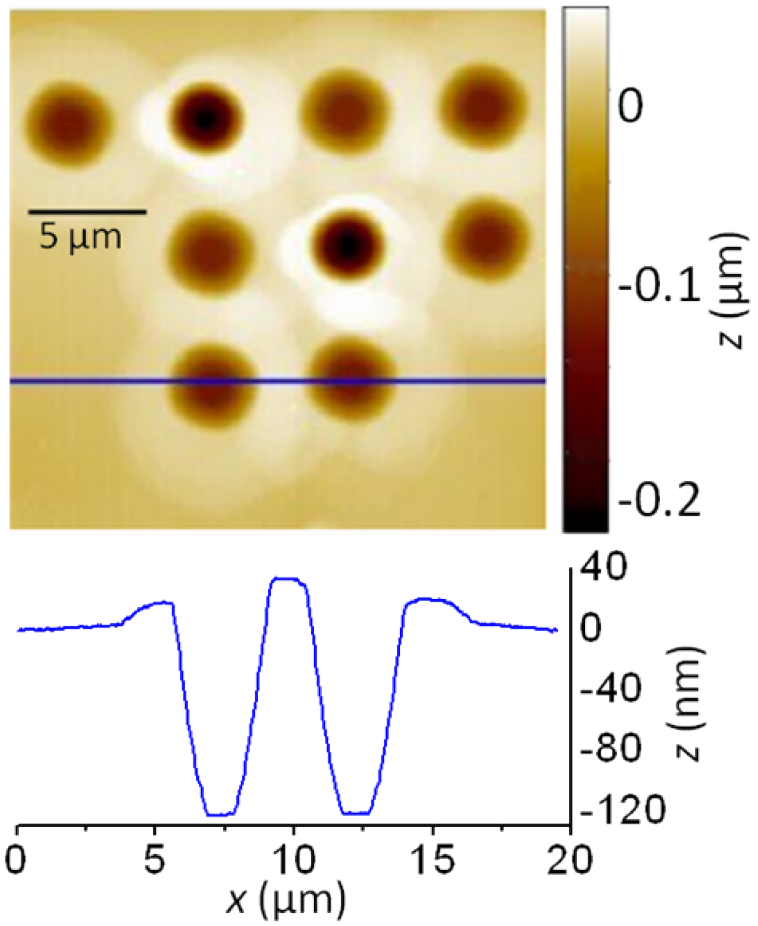

Figure 4.8: AFM image of typical dissolution pits on a NaCl microcrystal for a contact time of 10 ms. The profile is across the area marked by the blue line.

100 nm, *vide supra*) and so is essentially negligible compared to the estimated wetting area. It is important to note that the dissolution by a small retained volume of solution is exacerbated for this particular system because the solution in the meniscus is highly undersaturated with respect to the highly soluble NaCl. For less soluble materials characterized by fast kinetics such effects would be negligible, and it would be possible to elucidate dissolution kinetics by the measurement of pit depths and/or conductance currents.

4.4 Conclusions

We have presented the first use of a dual-barrel conductance micropipette as a new method for studying ionic crystal dissolution kinetics. Multiple conductance measurements across a crystal surface produce highly reproducible current-time measurements with high temporal resolution that are sensitive to the rate of dissolution of the surface. A key feature of the technique is that the sample is only exposed to the solution where the meniscus makes contact, and that measurements can be made with sub-millisecond time resolution, opening up the possibility of studying materials with a wide range of solubilities and particularly highly soluble crystals. The study of the NaCl crystals provided a first-order rate constant for dissolution of $(7.5 \pm 2.5) \times 10^{-5}$ cm s^{-1} (or equivalent intrinsic dissolution flux *ca.* 0.5 µmol cm^{-2} s^{-1}) determined by comparing FEM simulations to experimental conductance current data. These values are in good agreement with earlier measurements, serving to validate the technique.[67,192,193,200,207]

A further strength of the technique is that it is amenable to a high level quantitative description of mass transport and surface kinetics. Simulations demonstrate dissolution kinetics with rate constants, k, up to *ca.* 0.1 cm s^{-1}, assuming a first order process in interfacial undersaturation, which is larger than any reported ionic crystal dissolution rate should be measureable. The simulation could, if required, incorporate more complex dissolution kinetics and so be applicable to a wide range of materials.

In the future, it should be possible to use the micropipette (or even a nanopipette) to scan over a surface, providing an opportunity to study the impact of surface heterogeneities on dissolution kinetics at a quantitative level with high spatial resolution.[85] Moreover, there should also be scope for determining kinetics through the analysis of the local etch features produced. This was not possible in the present study of NaCl due owing to its very high solubility, and relatively low rate constant, leading to the continued dissolution and reprecipitation of material by a small amount of solution retained on the crystal surface.

4.5 Acknowledgements

We thank the European Research Council for providing funding for S.L.K, M.E.S, M.P, K.M and P.R.U. though the European Community's (EC's) Seventh Framework Programme (FP7/2007-2013)/ERC-2009-AdG2471143-QUANTIF and the EPSRC for a MOAC/DTC studentship for K.M. We also acknowledge the support of Advantage West Midlands Science City Advanced Materials Project and the European Regional Development Fund for providing some of the equipment used in this work.

Chapter 5

Targeted Dissolution of Calcite on the Microscale using the Dual-Barrel Conductance Micropipette Technique: Kinetics and Patterning

Calcite dissolution is studied with the dual-barrel conductance micropipette technique combined with AFM measurements. A dual barrel micropipette, equipped with two quasi-reference counter electrodes and filled with electrolyte solution (HCl in KCl) forms a conductimetric cell that can be brought into meniscus contact with a sample. This methodology can be used to rapidly create many etch pits on a pristine calcite (104) surface. AFM is then used to analyse the morphology of pits dissolved for different meniscus contact times. The flux determined from the AFM data ($(1.9 \pm 0.2) \times 10^{-8}$ $\mathrm{mol\,cm^{-2}\,s^{-1}}$*) is used to inform a finite element method model which allows the extraction of the heterogeneous rate constant, k_0, (*0.14 ± 0.07 $\mathrm{cm\,s^{-1}}$*) for the H^+ induced dissolution of calcite, defined by $j_{Ca^{2+}} = k_0[H^+]$; where $j_{Ca^{2+}}$ is the calculated flux and $[H^+]$ is the instantaneous proton concentration. The dual-barrel conductance micropipette is used for etch patterning, where the meniscus is translated laterally while in contact with the calcite surface. This reveals that dissolution*

has a strong dependence on the direction of micropipette movement. This can be rationalised based on the crystallographic directional dependents of calcite dissolution. Lastly, the versatility of this single technique is shown by using the micropipette to write on a calcite surface.

5.1 Introduction

The precipitation and dissolution of calcite ($CaCO_3$) is of scientific and industrial importance. Chemical processes involving calcite play a major role in the carbon cycle,[209–211] and calcite is used in the agricultural and construction industry.[212,213] For these reasons, and others, calcite dissolution has been extensively researched. There are many facets to the study of calcite dissolution due to its high sensitivity to solution composition. Previous studies have showed dependence on pH,[128,214] electrolyte concentration[215,216] and other additives, such as metal ions,[217] and organics.[134,148] A challenge when studying fast dissolution processes is to achieve high enough mass transport rates that the dissolution is at least partly surface-kinetically controlled. This is particularly true of calcite dissolution by acid attack, which was long-considered to be controlled by H^+ transport to the calcite/aqueous interface, as studied by techniques such as the rotating disc method and other methods.[132,218]

The advent of techniques with high mass transport rates, such as the fast flow channel electrode[219] and scanning electrochemical microscopy (SECM),[155] have allowed the kinetics of acid attack to be measured. These two techniques do have drawbacks, the channel flow technique measures the average dissolution for a macroscopic surface and SECM, while allowing high resolution, targeted measurements, requires that a reagent (H^+) can be generated electrochemically, which limits its applications.

The micropipette based method used herein represents an advance in dissolution methodology by offering high mass transport rates, the chance to include a wide range of reagents into the solution and confining dissolution to a well-defined micron scale. Additionally, spatial control of the micropipette opens up the possibility of etch-patterning, as well as revealing important information on crystallographic effects on dissolution rates, as we show herein.

Dual-barrel ion conductance probes have been used in a variety of ways in the past few years. In essence, a dual-barrel theta capillary is pulled to a sharp tip at one end that can have an opening as small as ∼90 nm in radius.[94,95] These probes are filled with a solution of interest to create a meniscus that protrudes from the tip of the probe. This is then lowered onto a surface of interest, and a variety of experiments and measurements can be performed with the liquid meniscus (not the solid probe) making contact with the surface. These uses include imaging conductive and nonconductive surfaces,[85] studying the reactivity of single nanoparticles,[96] patterning surfaces with multiple substances[87,97] and crystal dissolution studies.[84,88] We apply the principles of dual barrel conductance microscopy to investigate the dissolution rate of calcite under acid attack. In contact with a solution containing a strong acid the dissolution of calcite proceeds as such:

$$\mathrm{CaCO_{3(s)} + H^{+}_{(aq)} \rightarrow Ca^{2+}_{(aq)} + HCO^{-}_{3(aq)}} \tag{5.1}$$

The barrels are filled with solution containing a low concentration of both 1 mM KCl as an inert electrolyte to create a measurable current in the system, and 1 mM HCl as an acidic species. The resulting acidic solution (pH 3.3) dissolves the calcite, via proton attack, only when the meniscus is in contact with the surface. This technique can be used to extract rate information in two ways. Firstly, the etch pits created during dissolution can be measured and characterised using AFM. The shape and volume of the pits can be measured against dissolution time, which, in this case, is the amount of time the meniscus spends on the surface before the probe is retracted. Temporal resolution of the technique is 1 ms or better.[88] Secondly, in principle, the conductance current between the QCREs can be recorded during the dissolution.[88] The conductance current is dependent on the ion concentration in solution, but also on the most resistive section of the circuit and in the case of the dual barrel pipette, this part is the meniscus at the bottom of the tip. The composition of the meniscus has a strong influence on the ion current, as H^{+} attacks the surface, $HCO_3{}^{-}$ and $Ca_2{}^{+}$ are produced changing the resistivity of the meniscus and therefore the ion current could register a proportional change. To analyse the recorded conductance currents and etch pits, a com-

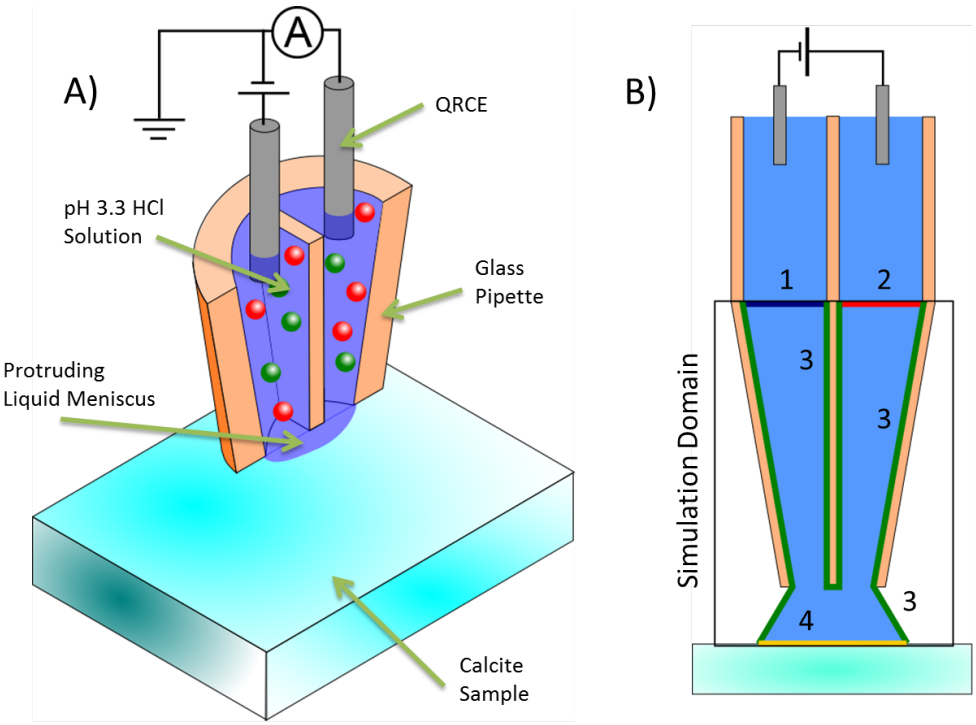

Figure 5.1: A) Diagram of the setup, the borosilicate glass pipet is held above the crystal sample. The two barrels are filled with a dilute HCl (in KCl) solution resulting in a meniscus forming out of the bottom of the pipet. Two QRCE are placed in the barrels to form a complete electrochemical cell. B) Diagram of the simulation, showing the simulation domain in relation to the entire pipette and sample. Boundaries 1 and 2 have an applied potential and are set to the bulk concentrations of all species, boundary 3 has no normal flux and boundary 4 has flux conditions for the relevant species.

plementary finite element method (FEM) model is implemented. Finally, line scans and patterning of calcite while scanning a meniscus laterally over the calcite surface reveals information on direction-specific dissolution rates.

5.2 Experimental

5.2.1 Materials and Solutions

Milli-Q reagent grade water (resistivity *ca.* 18.2 MΩ cm at 25 °C) was used for all solutions. SECCM probes were filled with 1 mM KCl and 1 mM HCl for acidic solutions. Solutions were made fresh each day. Calcite samples were

cleaved with a sharp, flat razor blade from naturally occurring single crystals of Iceland Spar (Richard Tayler Minerals, UK) to create clean (104) faces. New samples were cleaved immediately before use and secured to a glass slide. Dual-barrel conductance micropipettes were fabricated from borosilicate theta pipettes (30-0114, Harvard Apparatus) pulled to a sharp point using a laser puller (P-2000, Sutter Instruments). The pulling parameters used for the 1 µm probes are as follows: Heat 550, Fil 4, Vel 30, Del 120, Pul 28. All pipettes used for experiments were 1.0 ± 0.2 µm in diameter as determined by field emission scanning electron microscopy (FE-SEM) (Supra 55-VP, Zeiss).

5.2.2 Instrumentation

The experimental setup was similar to that of the SECCM technique.[90,96,97] A schematic of the system is shown in Figure 5.1(A). The sample is mounted on a XY piezoelectric positioning stage (Nano-Bio300, MadCityLabs) and the pipette was mounted on a Z piezoelectric positioning stage (P-753.3CD, Physik Instrumente). A bespoke current follower, constructed in-house, was used to record the current between the two QRCEs. All elements of the system were controlled by a field programmable gate array (FPGA) card running a LabVIEW program (11.0, National Instruments).

5.2.3 Methodology

The most resistive part of the circuit within the dual barrel conductance micropipette is the small liquid meniscus that forms at the bottom connecting the two barrels, and so changes to the meniscus shape and size can be seen as a change in current. In air, the meniscus is small and highly resistive which results in a proportionally small current (*ca.* 0.1- 0.2 nA) herein. Upon reaching the calcite surface the meniscus jumps to contact with the crystal, which increases its size and decreases the resistance inducing sharp increase in current. Two experimental procedures were used to study calcite dissolution: 1) Hopping and 2) Raster Scans.

The hopping procedure used the Z piezoelectric positioner to land the meniscus on the surface without the pipette touching the surface; this was achieved by programming the Z piezoelectric positioner to stop once a selected

threshold in DC current was reached. The pipette was held stationary for a pre-set length of time while dissolution took place and then the pipette was withdrawn vertically away from the surface. Many repeat measurements could be made quickly and easily on a fresh section of crystal every time. This was done by laterally repositioning the pipette while away from the surface and then starting another approach with the same DC threshold. The time between approaches (seconds) was long compared to the time required for the meniscus composition to re-establish initial conditions ($\ll$ 1 s).[88]

The raster scan procedure used the same landing method during the approach, but then the pipette was kept in contact with the surface and was moved laterally across the substrate surface at a speed of 1 µm s^{-1}. For each raster scan, 40 µm length scan lines were generated with alternating scan direction, and were 10 µm apart. To maintain a constant height, from the end of the pipette to the crystal surface, an AC feedback system was used. A lockin amplifier generated a sine wave that was applied to the Z piezoelectric positioner which, in turn, oscillated the probe to generate an AC ion current. Once the meniscus was in contact, the AC signal increased significantly due to periodic deformation of the meniscus. The AC signal is sensitive to pipette-surface separation distance, so when the probe is moved laterally the Z position is constantly making subtle adjustments in order to maintain the same AC signal, and therefore the same pipette-surface distance.

The dissolution pits resulting from hopping experiments and dissolution trenches resulting from raster scans were imaged using AFM (Catalyst, Bruker-Nano), and subsequently analysed using the Scanning Probe Image Processor program (SPIP 6.0.14, Image Metrology).

5.2.4 Finite Element Method Model

All simulations were performed on the commercial finite element method (FEM) simulation package Comsol Multiphysics (v5.0, Comsol AB). Simulations were performed using a 3D geometric domain of the meniscus and the end of the pipette, similar to that described previously,[90] as shown in Figure 5.1(B). Solution composition inside the pipette were calculated using MINEQL+ (chemical equilibrium modelling software, version 4.6), along with the activity corrected

dissociation and equilibrium constants. Two types of studies were used herein: 1) A time dependent study for the calcite acid induced dissolution was implemented to monitor the ion current change due to dissolution. 2) A stationary study was implemented to obtain steady state solution for acid induced dissolution A 3D FEM model was constructed to mimic the geometry of the end of a 500 nm major radius, 400 nm minor radius, 7° half-cone angle theta pipette and with the pipette at 300 nm distance from the surface, as shown in Figure 5.1(B). Due to the presents of a plane symmetry perpendicular to the septum of the theta pipette only half the domain need be simulated. The solution inside the probe contained 1 mM KCl and 1 mM HCl, at pH = 3.3. Simulations were constructed using the "transport of diluted species", "chemical reaction engineering" and "electric current" modules. At low pH values the dissolution of calcite is dominated by the process in Equation 1. The concentration of all species in the pipette solution are governed by the equilibria summarised in Table 5.1. The contribution of diffusion inside the pipette for the steady state simulation was determined from Fick's first law:

$$j = -D_B \nabla [B] \tag{5.2}$$

where j, [B] and D_B are the diffusional flux, concentration of the diffusing species and diffusion coefficient of species [B], respectively. For the time dependent model, Ficks second law was used:

$$\frac{\partial [B]}{\partial t} = D_B \nabla^2 [B] \tag{5.3}$$

Boundaries 1-2 in Figure 5.1(B) represent the end of the simulated probe domain, boundaries labelled 3 denote the unreactive pipette walls and the meniscus/air boundary and boundary 4 is the active top surface of the calcite microcrystal. The boundary conditions for the model are listed in Table 5.2,

5.2.5 Crystallography

A Laue X-ray crystallography Photonic-Science camera system was used to ascertain the crystal orientation of the calcite samples used in the raster scan-

Table 5.1: Equilibria data for the calcite-H_2O system open to the atmosphere.[205]

Reaction	pK_a/pK_{eq}
$CO_2 + H_2O \rightleftharpoons H_2CO_3$	1.466
$H_2CO_3 \rightleftharpoons H^+ + HCO_3^-$	6.351
$HCO_3^- \rightleftharpoons H^+ + CO_3^{2-}$	10.33
$CaCO_3(aq) \rightleftharpoons Ca_2^+ + CO_3^{2-}$	3.2
$H_2O \rightleftharpoons H^+ + OH^-$	13.997

Table 5.2: Boundary conditions applied in the model of calcite acid induced dissolution.

Boundary	Condition
1	V = 0.2 V $c_i = c_{0,j}$
2	V = -0.2 V $c_i = c_{0,j}$
3	$J_i = 0$
4	$J_{Ca^{2+}} = k_0[H^+]$ $J_{HCO_3^-} = k_0[H^+]$ $J_{H^+} = -k_0[H^+]$

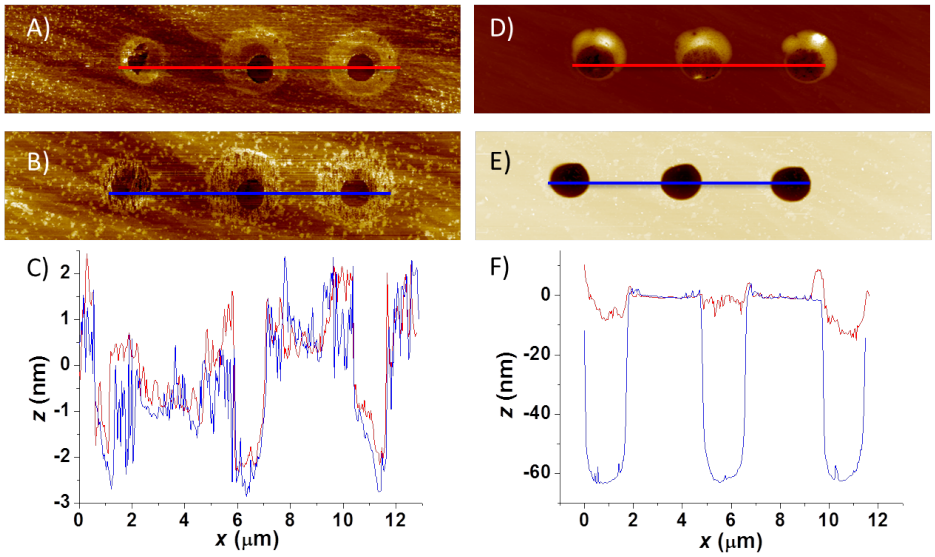

Figure 5.2: A set of three dissolution pits created with a 0.2 s etch time, A) before and B) after washing. C) The line profiles from A and B. A set of three dissolution pits with a 5 s etch time, D) before and E) after washing. F) The line profiles from D and E.

ning experiments. Micrographs were analysed using CrystalMaker (version 9.1.0) single crystal Laue X-ray diffraction simulation.

5.3 Results and Discussion

5.3.1 AFM Measurements of Etch Pits

All the etch pits created in this study were imaged using AFM before and after being rinsed briefly with Milli-Q water. It is possible that a tiny droplet of solution could remain on the surface after the tip is withdrawn.[208] The solution evaporates rapidly leaving mostly the electrolyte salt KCl. With a solubility that is three orders of magnitude higher than calcite, this was washed away by a small jet of water during the rinsing step. Any $CaCO_3$ left on the surface will precipitate into an amorphous form and also be washed away. The morphology of the pits does not change during this washing process, as evident from Figure 5.2. AFM images of before and after washing were compared for dissolution times of 0.2 s and 5 s. The subtle features of the pits seen in the

0.2 s dissolution time image are preserved after washing, demonstrating that only a precipitated material is removed. In contrast, the 5 s dissolution time image shows a great difference before and after the wash, this can, therefore, be attributed solely to removal of precipitated material.

The etch pits can be used to calculate a rate by comparing the change in morphology with respect to dissolution time. Figure 5.3 shows typical AFM images for a set of nine pits created with an etch time of A) 10 s and B) 2 s. The increasing etch pit volume is visibly evident between these two etch times and a full graph of etch pit volume by etch time is shown in Figure 5.4(A), this gives an pit volume increase of 0.021 $\mu m^3\,s^{-1}$. Figure 5.4(B) gives the pit depth as 8.9 $nm\,s^{-1}$. Using the density of calcite, 2.71 $g\,cm^{-3}$,[205] and the diameter of the etch pits, this can be converted to give a flux of $(1.9 \pm 0.2) \times 10^{-8}$ $mol\,cm^{-2}\,s^{-1}$. The diameter and surface flux was seen to remains roughly constant as shown in Figure 5.4(C and D). There may be an induction time before the start of dissolution which would be roughly constant, thus experiments lasting $\leqslant 1$ s may be affected by this induction time as its percentage of total etch time will be larger. This would act to lower the calculated flux for those experiments, which is shown in the data.

5.3.2 Simulations

When the meniscus spreads out onto the surface of the calcite and begins to dissolve the crystal a number of processes take place. Protons in the meniscus are depleted, the ion mobility of protons (3.62×10^{-7} $m^2\,s^{-1}\,V^{-1}$) is much higher than either $Ca_2{}^+$ or $HCO_3{}^-$ (6.2×10^{-8} and 4.6×10^{-8} $m^2\,s^{-1}\,V^{-1}$) respectively)[109,125] but the stoichiometry adds complexity. In fact, taking account of these factors, the FEM time dependent model shows that the ion current remains close to constant with a decrease below the level of detection of the current follower used. This affect is shown in Figure 5.5.

Typical profiles of H^+ and $Ca_2{}^+$ concentration and the electric field from the steady state simulation are shown in Figure 5.6. A set of dissolution rate constants, k_0, were used in the simulation to generate a working curve for different meniscus wetting areas (see Figure 5.7). Subsequently, the dissolution

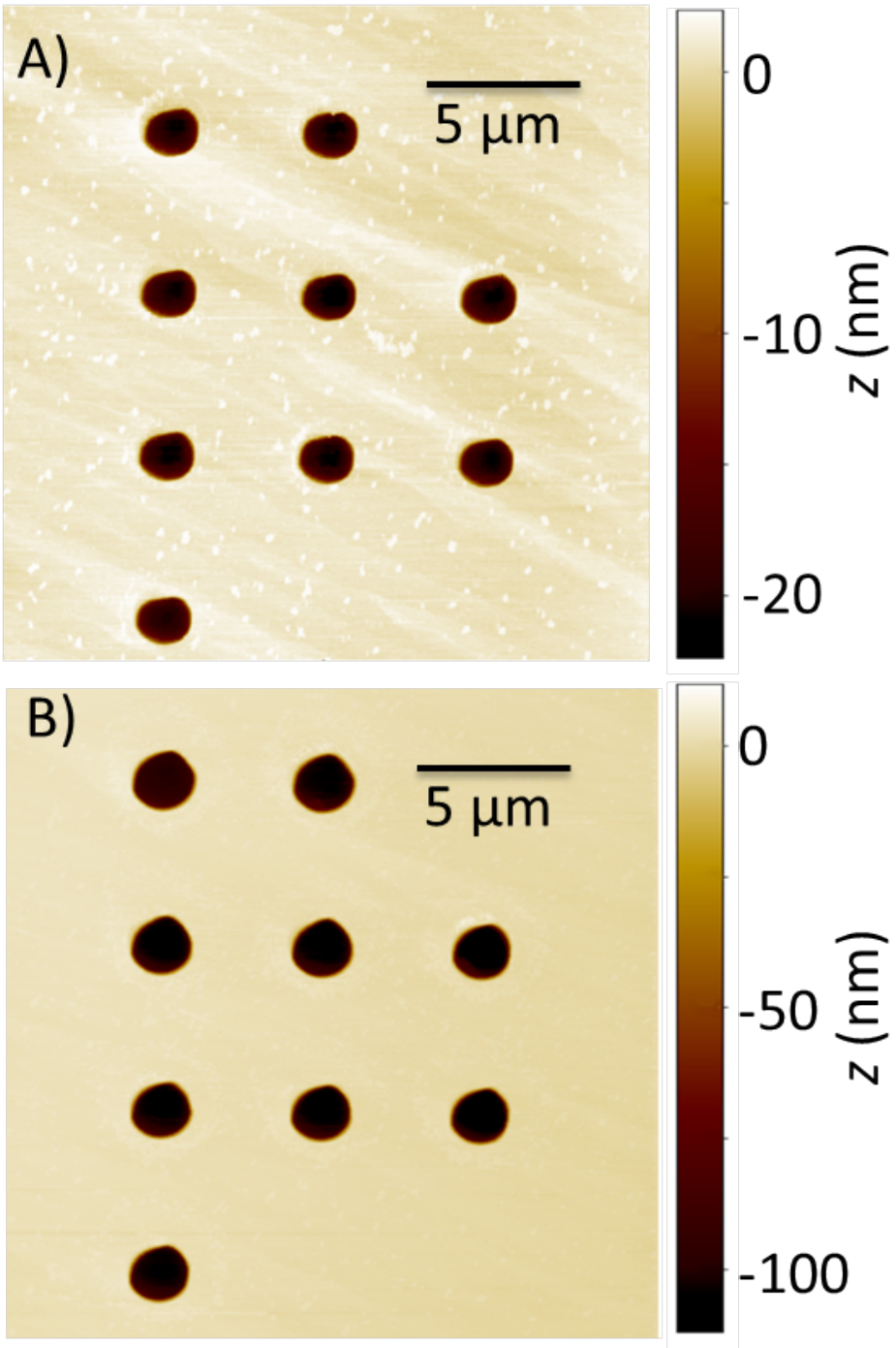

Figure 5.3: AFM image of a set of etch pits made with the dual barrel conductance probe. The meniscus was in contact with the crystal for A) 2 s and B) 10 s.

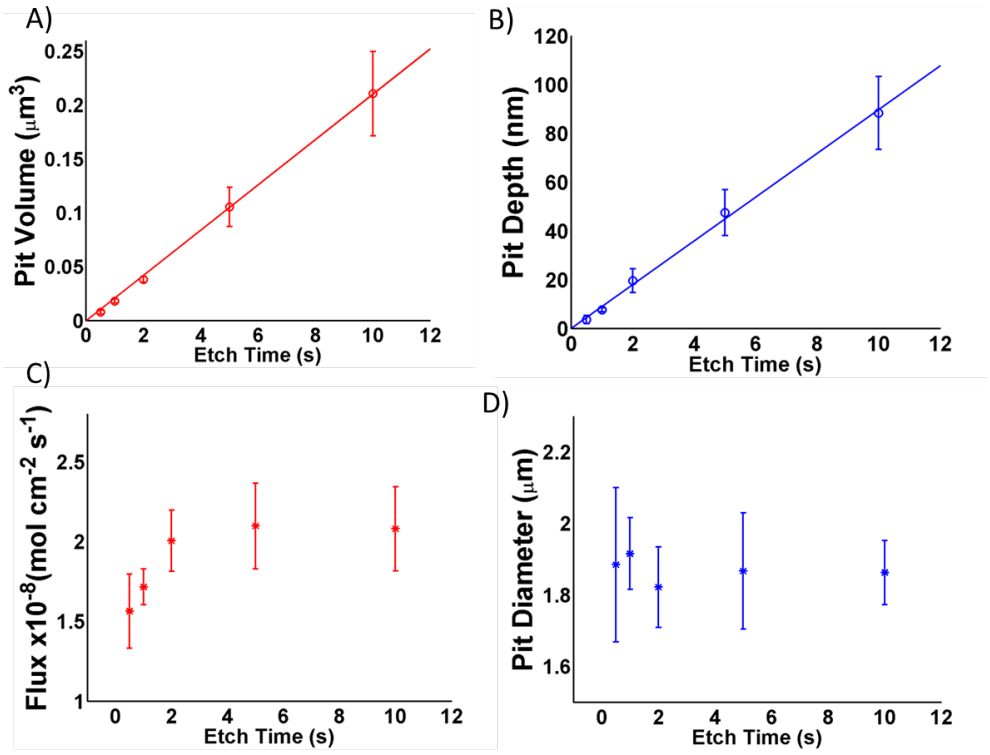

Figure 5.4: Graphs of etch time vs A) pit volume, B) pit depth, C) pit diameter and D) flux. Each circle represents the average of 36 etch pits analysed from AFM. A least squares regression line of best fit is shown as well as error bars showing the standard deviation.

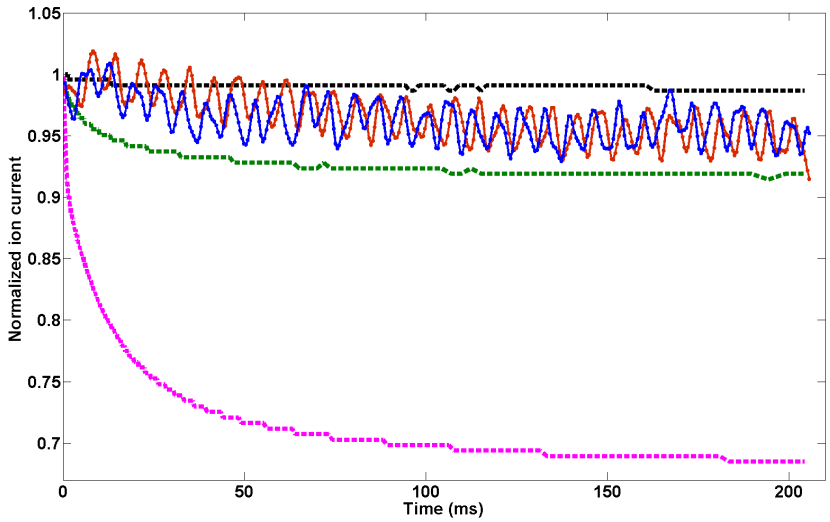

Figure 5.5: The change in the DC ionic current for 0.2 s landing that is obtained from time dependent FEM simulation (dotted lines), with k_0 values in $\mathrm{cm\,s^{-1}}$ of 0.001 (black), 0.01 (green) and 0.1 (pink) and typical experimentally obtained values (solid lines, red and blue).

flux value of $(1.9 \pm 0.2) \times 10^{-8}$ $\mathrm{mol\,cm^{-2}\,s^{-1}}$, that was calculated from the AFM etch pit analysis was used to match the simulated surface fluxes, and thus predict the dissolution rate constant for calcite. This value was found to be 0.14 ± 0.07 $\mathrm{cm\,s^{-1}}$. At high k_0 values, the surfaces flux reaches a plateau. This represents where the system becomes mass transport controlled. The reported value for calcite dissolution rate constant is significantly below this threshold and therefore is largely under kinetic control.

5.3.3 Raster Scanning

The raster scanning experiments clearly showed two distinct trench morphologies on the calcite that were found to be dependent on scan direction. Figure 5.9(A) shows a representative AFM image of the trenches created during a raster scan. The histogram in Figure 5.9(B) illustrates the difference in morphologies for the dissolution trenches in different directions. The crystal direction for the scanned sample were extracted through Laue X-ray analysis. An example of Laue micrograph and a superimposed simulation fit from Crys-

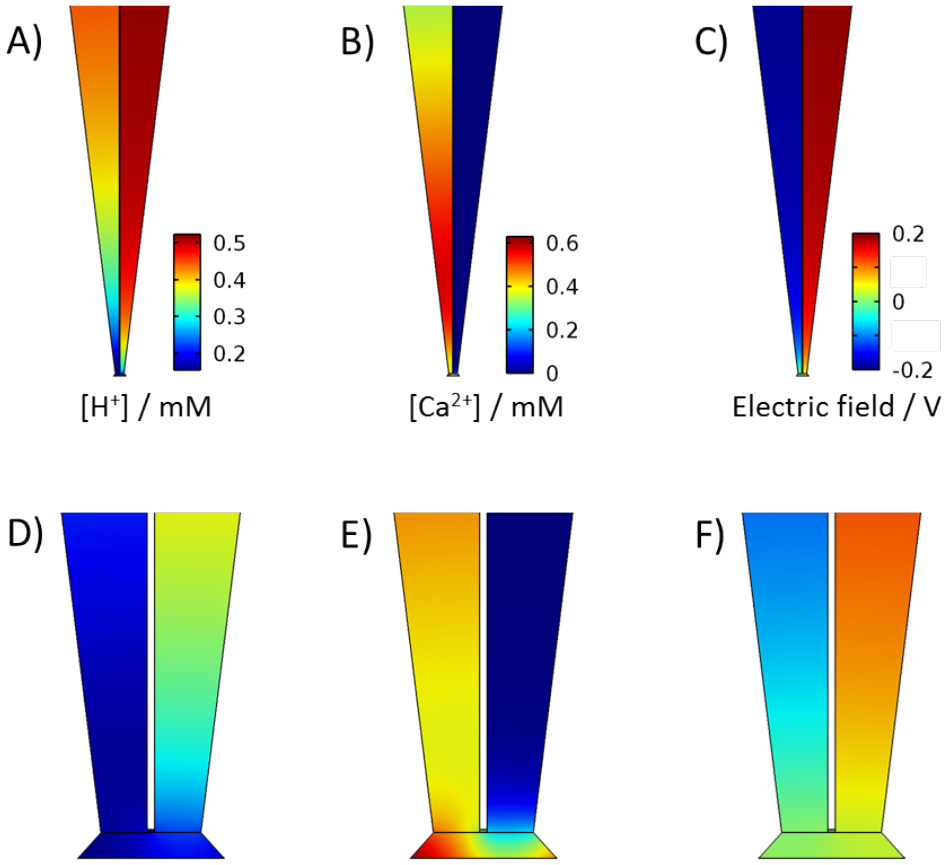

Figure 5.6: Profiles of A) $[H^+]$ and B) $[Ca^{2+}]$ and C) electric potential, for the meniscus and 50 µm of the probe, for the steady state model a k_0 of 0.1 $cm\,s^{-1}$. D, E and F show profiles of the same variables, respectively, for 3 µm from the base of the meniscus.

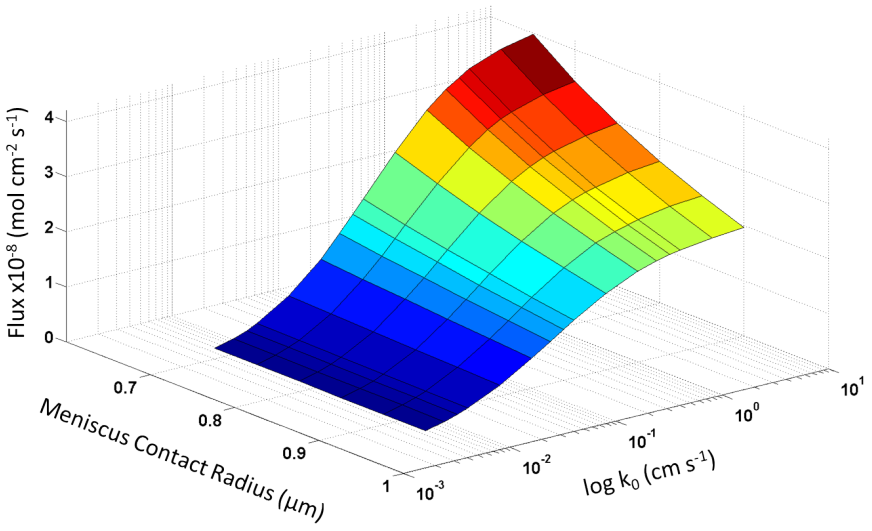

Figure 5.7: Working curve generated from the FEM model showing the dependence of the surface flux on both the dissolution constant rate, k_0, and the meniscus contact radius.

talMaker are shown in Figure 5.8, along with the CrystalMaker image of the crystal surface.

When the probe was translated in the $[48\bar{1}]_+$ and $[\bar{4}41]_+$ (positive) directions the resulting trenches are wide and shallow, while the $[48\bar{1}]_-$ and $[\bar{4}41]_-$ (negative) directions produced narrow and deep trenches, illustrated in Figure 5.10(C). This phenomenon could be attributed to the rhombohedral crystal structure. The step edges for the positive and negative steps are not equivalent.[121,220,221] In the positive direction an obtuse angle of 102° between the terrace and the basal plane is formed, while for the negative direction the atoms on the upper terrace overhangs with an acute angle of 78°. Previous work on calcite dissolution established that the positive steps dissolve faster than the negative steps.[220,221] During the raster scan, two types of moving steps would result once the probe makes contact with the crystal surface, acute and obtuse. Thus, the protons are quickly consumed, resulting in lateral dissolution by both positive steps. This produces the wide, shallow trenches. Conversely, when the probe is moved towards a negative direction ($[48\bar{1}]_-$ and $[\bar{4}41]_-$) only one obtuse step is in contact with the meniscus, see Figure 5.10(A). If the probe moved laterally towards the positive ($[48\bar{1}]_+$ and

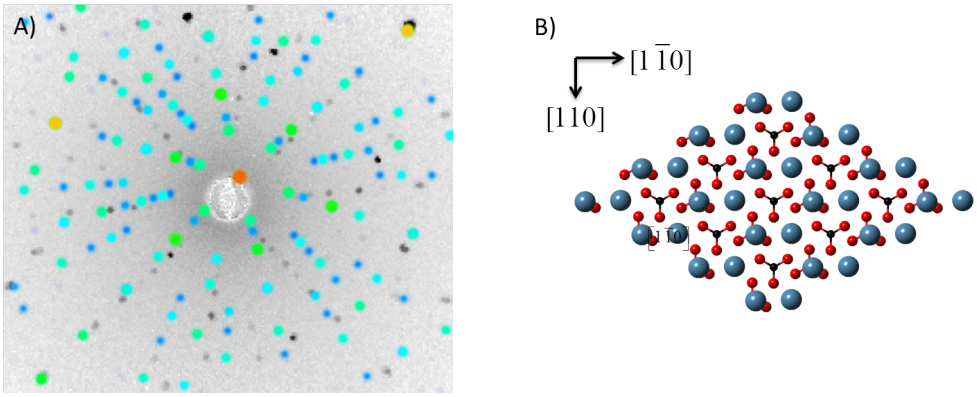

Figure 5.8: A) Laue X-ray micrograph of a typical calcite sample, superimposed with the CrystalMaker simulated pattern. B) The structure of the (104) face of calcite, generated from CrystalMaker.

$[\bar{4}41]_+$) directions the trenches would consist of two adjacent obtuse steps and one acute step at the leading edge, see Figure 5.10(B). This constricts lateral dissolution and promotes vertical dissolution, resulting in the deep, narrow trenches. The possibility of the electric field within the probe being responsible for this phenomenon was explored by running two scans with the same probe in close proximity to each other. Both scans followed an identical pattern. The probe was aligned so that the septum was perpendicular to the major scan direction. The QRCE of the leading barrel was negatively charged during the first scan and the polarity was reversed for the second scan. Although the morphology of the pits still varied with direction, these variations were closely similar in both scans thus ruling out any effect of probe alignment.

5.3.4 Patterning

An upshot of having a high level of spatial control for dissolution is that patterns of any shape can be etched into the crystal. The probe can be programmed to move between any given set of co-ordinates. For the directional dissolution studies these were a very simple line scan pattern. After this, more complicated patterns were tested. Figure 5.11 shows the result of one such complex pattern, as a proof of concept the word CALCITE has been written in 12 µm tall letters. Due to restrictions of the software only straight lines can be drawn. Curves can be achieved by increasing the number of points the

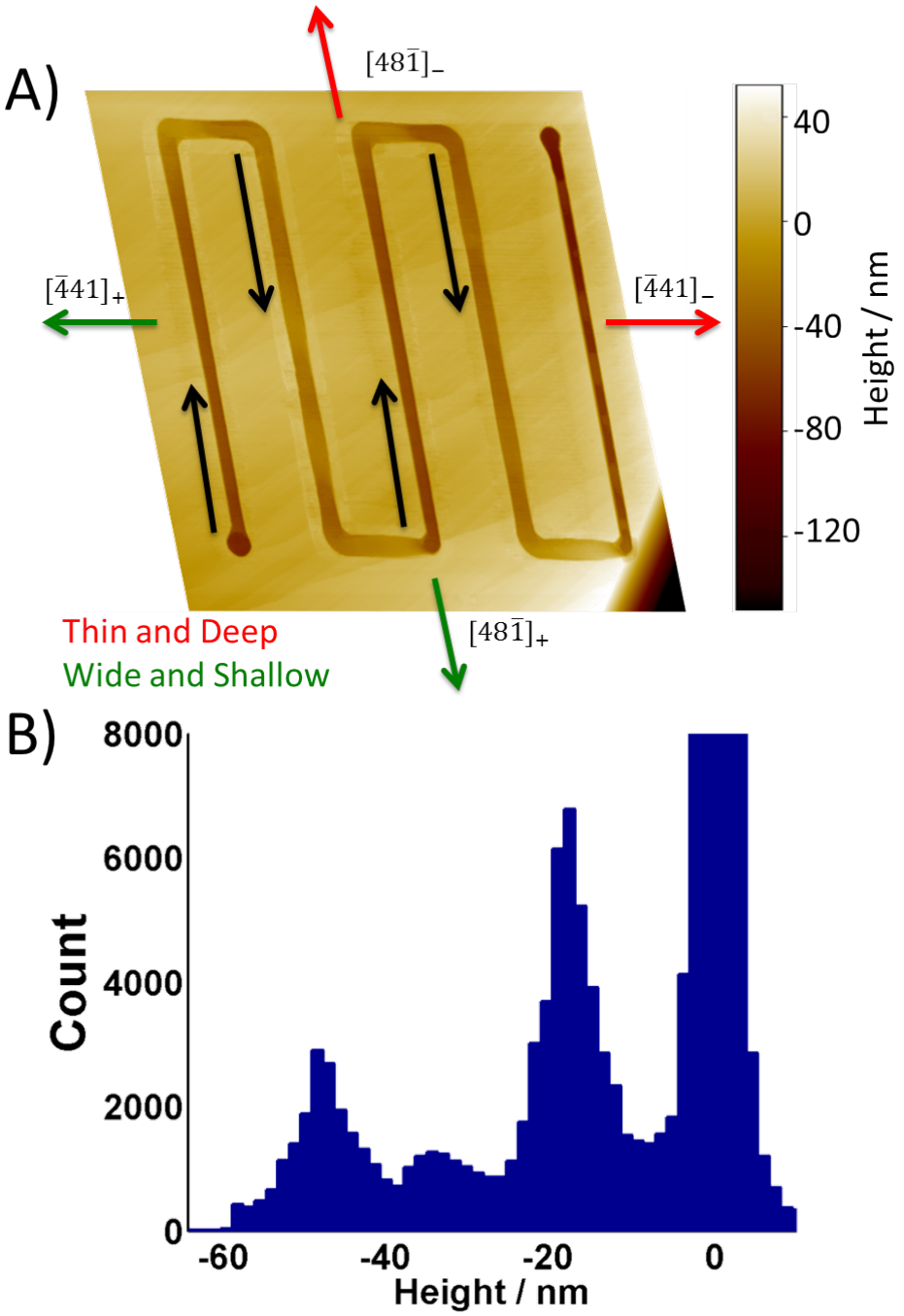

Figure 5.9: A) A representative AFM image of a raster scan showing the directional dependence of the dissolution in the trenches created. B) A section of a representative histogram of a raster scan, showing separate distributions for each direction.

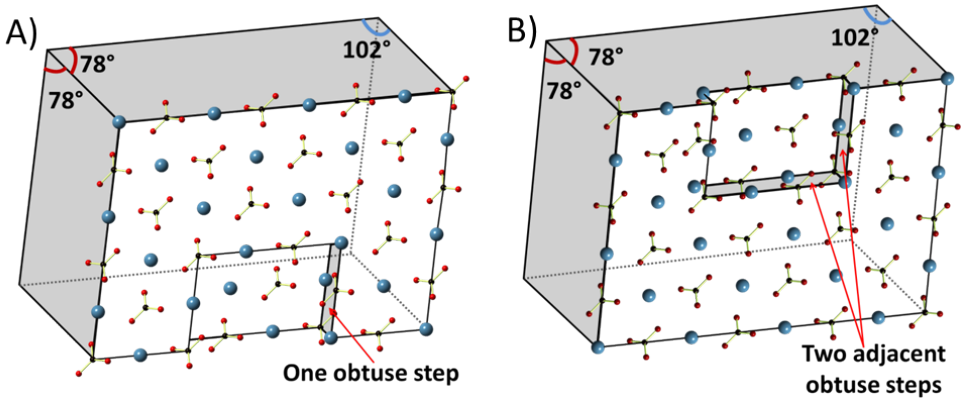

Figure 5.10: Top view of the (104) face where A) shows the two exposed obtuse steps, moving the probe in these directions results in wide, shallow pits. B) shows the acute step adjacent to only one obtuse step, moving the probe towards the acute steps results in constricted dissolution and narrow deep pits.

probe passes through to create a curve effect, this could be easily automated with a CAD program. The writing of text onto crystals is somewhat of a novelty, the real strength of this technique could be found in patterning crystals in order to control further growth or for identification of microscale samples.

Figure 5.11: AFM image of the word CALCITE etched into the crystal.

5.4 Conclusion

This work has shown that the dual-barrel conductance micropipette can be used in conjunction with AFM to study the dissolution of calcite and benefits from the advantages of both. These include excellent spatial and temporal resolution from the micropipette and the ability to make many measurements on the same surface at short timescales. Accurate morphology measurements of the etch pits can be obtained through AFM imaging. These data can then be used to analyse the dissolution. The morphology of the pits is correlated to a rate constant via a detailed FEM model. Since the calcite sample is held in air it has been possible to study directional dissolution whereas most other techniques dissolve the entire crystal surface. By translating the probe laterally during dissolution, the reactivity of different steps can be seen. In this case, moving the probe towards obtuse steps resulted in wide shallow pits while acute steps resulted in narrow deep pits. With such a high level of spatial control it has been possible to make detailed patterns on the surface of the crystal. For now this ability has been demonstrated as possible by writing the word CALCITE but in the future we predict this technique will be useful for a range of tasks on any crystal. These tasks include marking and subsequent identification of an area of interest on a crystal, controlling crystal growth. This technique could be used on appropriate substrates for the fabrications of microfluidic channels.

5.5 Acknowledgements

We extend our thanks to the European Research Council for funding through the European Community's (EC's) Seventh Framework Programme (FP7/2007-2013)/ERC-2009-AdG2471143-QUANTIF. We are grateful to Alex Colburn (University of Warwick) for custom built electronics and to Dr. Monica Ciomaga Hatnean for Laue X-ray crystallography and fruitful discussions.

Chapter 6

Surface Charge Mapping with a Nanopipette

Nanopipettes are emerging as simple but powerful tools for probing chemistry at the nanoscale. In this chapter the use of nanopipettes for simultaneous surface charge mapping and topographical imaging is demonstrated, using a scanning ion conductance microscopy (SICM) format. When a nanopipette is positioned close to a surface in electrolyte solution the direct ion current (DC), driven by an applied bias between a quasi-reference counter electrode (QRCE) in the nanopipette and a second QRCE in the bulk solution is sensitive to surface charge. The charge sensitivity arises because the diffuse double layers at the nanopipette and the surface interact, creating a perm-selective region which becomes increasingly significant at low ionic strengths (10 mM 1:1 aqueous electrolyte herein). This leads to a polarity-dependent ion current and surface-induced rectification *as the bias is varied. Using distance-modulated SICM, which induces an alternating ion current component (AC) by periodically modulating the distance between the nanopipette and the surface, the effect of surface charge on the DC and AC is explored and rationalized. The impact of surface charge on the AC phase (with respect to the driving sinusoidal signal) is highlighted in particular; this quantity shows a shift that is highly sensitive to interfacial charge and provides the basis for visualizing charge simultaneously with topography. The studies herein highlight the use of nanopipettes for functional imaging, they also provide a framework for the design of SICM ex-*

periments, which may be convoluted by topographical and surface charge effects, especially for small nanopipettes.

6.1 Introduction

Electrochemical measurements using nanopipettes filled with electrolyte solution provide a platform for nanoscience with myriad applications. These include analytical science,[203,222–225] materials characterization[226–229] and live cell studies.[67] Nanopipettes used as the probe in scanning ion conductance microscopy (SICM) are particularly powerful as a means of imaging the local topography of substrates.[64,66,67,172] A bias is applied between a quasi-reference counter electrode (QRCE) in the nanopipette and another in the bulk of the solution to induce a direct ion current (DC) through the end of the nanopipette, as illustrated schematically in Figure 6.1. As the nanopipette-surface distance decreases, the solution resistance in the nanopipette-surface gap increases which, in turn, reduces the ion current. This decrease in ion current is used as a non-contact signal to sense the nanopipette-surface distance and ultimately for topographical imaging,[171,230,231] proving particularly effective for soft samples.[67,232]

SICM is typically operated in aqueous solutions with relatively high ionic strength. Under these conditions the diffuse double layer (DDL) that forms at interfaces in solution is compressed (usually down to a (sub-) nanometer level),[233] ensuring that the nanopipette current is relatively insensitive to surface charge effects and that the substrate topography is faithfully reproduced.[234] However, at lower electrolyte concentrations, the DDL characteristic length increases up to the several nanometer scale (in aqueous solutions), leading to surface charge effects such as ion current rectification (ICR) due to a polarity (bias) dependent conductivity of the nanopipette, as seen in simple nanopipette studies of bulk solutions.[174,175,235,236] At small separation distances between a nanopipette and a charged substrate, the interaction of the respective DDLs similarly leads to changes in the ion current signal (surface-induced rectification)[237] opening up the prospect of surface charge mapping using SICM, as described herein. This is an important advance because there

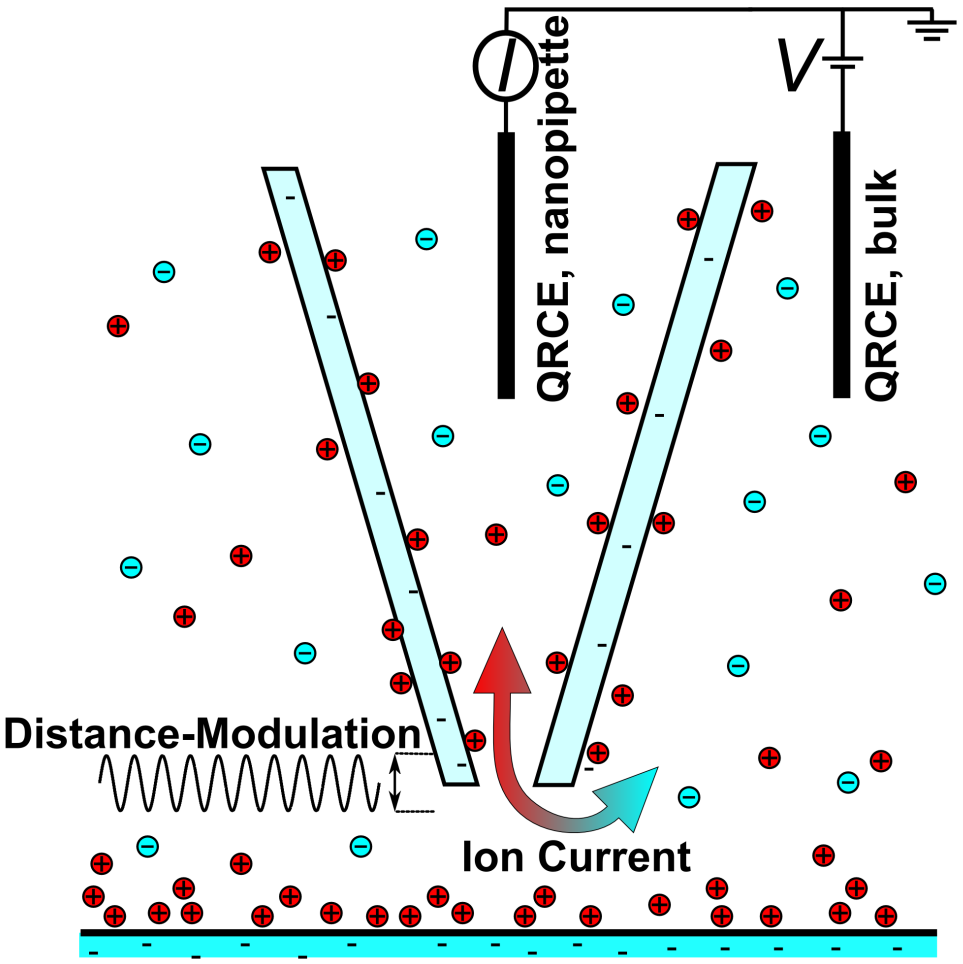

Figure 6.1: Schematic of an SICM probe, with one QRCE in a nanopipette and another in the bulk of the solution. A bias (V) is applied to the bulk QRCE and the ion current (I) is measured at the QRCE in the nanopipette. A distance-modulated technique is used where a sinusoidal modulation is applied to the position of the nanopipette.

are relatively few techniques for probing and visualizing charge at interfaces. Although atomic force microscopy (AFM) can be used,[238–241] it employs a tip of (nominally) fixed charge that may change during a scan (*e.g.* by contamination or tip wear), and the force-distance characteristics are influenced by electrostatic forces as well as several other forces. In contrast, as we highlight herein, the ion current through a nanopipette depends directly on the DDL at a charged surface and the applied potential can be tuned to optimize the response.

We use a nanopipette to investigate charged surfaces in electrolyte solutions at moderate aqueous ionic strength (10 mM 1:1 salt). We also take advantage of distance-modulated SICM,[76,242] where the nanopipette-surface distance is oscillated with a small amplitude at a particular frequency to produce an alternating component (AC) in the ion current. We show that the ion current response (both DC and AC) is significantly affected by both substrate surface charge and the applied potential through approach curve measurements towards materials with different surface charge characteristics, namely glass, polystyrene and (3-aminopropyl)triethoxysilane (APTES). In particular, we highlight that the *AC phase*, which has largely been overlooked in the SICM community, can give considerable information on the charge state of the surface. Experimental data are shown to be well represented with theoretical (finite element method) simulations. We use distance-modulated SICM to map the *topography and surface charge simultaneously* at model surfaces (polystyrene film with pinholes deposited on glass) and show that the phase signal, as well as the DC current, can distinguish between the two materials. We also demonstrate surface charge mapping of a soft positively charged polymer feature (poly-l-lysine), deposited as a small patch on a glass substrate. These model examples serve to illustrate the exciting possibility of using a nanopipette to map interfacial properties other than topography. We anticipate widespread applications in surface and interfacial science where knowledge of local surface charge would be hugely valuable for understanding interfacial processes.

6.2 Methods

6.2.1 Substrates

Glass bottomed petri dishes with detachable cover slips (3512, WillcoWells) were used. Before use, the detachable cover slip was sonicated in acetone for 10 minutes followed by sonication in water for 10 minutes and plasma ashing for 1 minute at 100 W in oxygen. These were then used immediately as glass samples or functionalized with either polystyrene or APTES. The polystyrene samples were either thick films prepared by evaporation of a solution of polystyrene in chloroform onto the glass, used for the nanopipette approach curve measurements, or dip coated for 30 seconds in a less concentrated polystyrene solution (see above), to produce a heterogeneous thin film with holes that exposed the glass in small regions. This created a surface of both neutral polystyrene and slightly negatively charged glass under the condition of the measurements (aerated, unbuffered, 10 mM KCl).[175,236,237,243] Silanized substrates were fabricated from glass coverslips immersed in the APTES/toluene solution for 30 minutes and then sonicated in chloroform to form a monolayer.[244] A substrate containing patches of positively charged PLL on a glass sample was created by taking a clean glass petri dish and depositing a spot of PLL for 3 minutes from a liquid meniscus formed in air at the end of a 5 µm diameter dual barreled-pipette, using the fabrication capabilities of scanning electrochemical cell microscopy.[97] This sample was then washed with water and dried under ambient conditions.

6.2.2 Instrumentation

The basic instrumentation has been described previously.[84,98] Briefly, the SICM probe was mounted on a 38 µm piezoelectric positioning stage (P-753-3CD, Physik Intrumente) for movement normal to the substrate (Z direction), while the sample was mounted on a two axis piezoelectric positioner system (Nano-BioS300, Mad City Labs Inc.) for lateral movement. The current was measured using a custom current-to-voltage converter. A lockin amplifier (SR830, Stanford Research Systems) was used to generate the driving signal for the oscillation of the probe position and to determine the magnitude

and phase of the AC ion current. Data recording, as well as the probe position and voltage output control, were performed using a LabVIEW (2013, National Instruments) based program through a FPGA card (7852R, National Instruments). The lockin amplifier phase calculation does not take into account the sign of the input signal, resulting in a 180° offset for negative current values compared to positive current values. Therefore, the phase at negative currents was translated by 180°, allowing phases at both positive and negative currents to be compared.

The nanopipette probe was filled with KCl solution, and an Ag/AgCl quasi-reference counter electrode (QRCE) was inserted. This was comprised of an AgCl-coated Ag wire.[90] The end of the nanopipette was placed close to the surface of interest that was immersed in KCl solution. A second Ag/AgCl QRCE was placed in the bulk of the solution. The QRCE in the bulk solution was biased with respect to the QRCE in the nanopipette, and the resulting ion current was measured at the QRCE in the nanopipette. All potentials quoted herein refer to *the potential of the QRCE in the nanopipette with respect to the bulk QRCE.*

6.2.3 SICM Approach Curves

The ion current, as a function of the nanopipette-substrate distance, was measured at different potential difference. To achieve this, the nanopipette was oscillated at 288 Hz with 10 nm peak-to-peak amplitude and approached at 10 nm s^{-1} towards the surface of interest with a bias of -0.2 V ($V_{QRCE,nanopipette}$ - $V_{QRCE,bulk}$). Once the surface had been detected, through an increase in the AC current magnitude to 7 pA, the potential was switched to the potential of interest and the nanopipette held stationary for 30 seconds for the ion current to stabilize. During this time the nanopipette-surface distance can change due to thermal expansion or retraction of the piezoelectric positioners (an effect called thermal drift).[245] However, as shown in Figure 6.2, repeated landings in the same location and with the same feedback setpoint showed that thermal drift is minimal for our experimental configuration (representing only 5 nm over 30 seconds) and so does not significantly affect the experimental results. The ion current response as the nanopipette was moved away from the surface

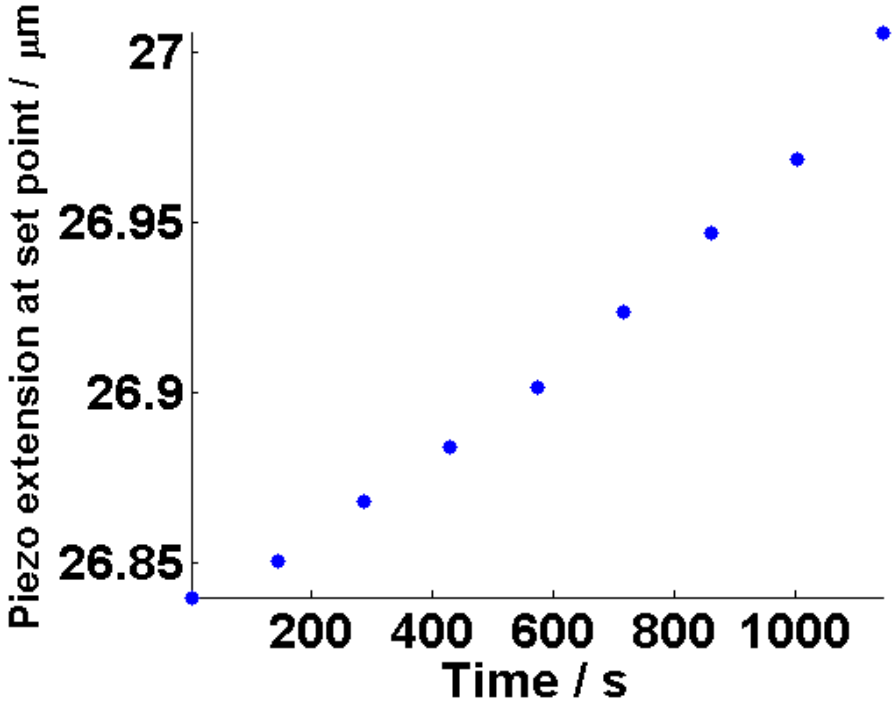

Figure 6.2: Peizoelectric positioner extension (Z piezoelectric position) at the point the AC ion current increase to 4 pA, for nine sequential approach curves to the same point.

at 10 nm s^{-1} was then recorded. For some approach curves over glass the nanopipette (biased positively) was approached further towards the substrate, with the current observed to fall monotonically to low values before crashing into the substrate.

6.2.4 SICM Maps

Two dimensional maps of a surface were generated in a hopping mode.[172,201,233] The SICM probe was approached, at 300 nm s^{-1}, to the surface of interest until the surface was detected, as an increase in the AC ion current magnitude to 4 pA, at multiple different lateral positions over the sample. The ion current and Z piezoelectric position was recorded during these hops and the values at the closest approach to the surface were used to construct two dimensional maps.

6.2.5 Atomic Force Microscopy

The height of the polystyrene/glass samples as revealed by SICM was compared to a section of the same sample imaged with atomic force microscopy (AFM) (Catalyst, Bruker-Nano) in contact mode using silicon tips on nitride lever (SNL-10, Veeco). AFM images were processed using the Scanning Probe Image Processor program (SPIP 6.0.14, Image Metrology).

6.2.6 Simulations

Two-dimensional finite element method (FEM) simulations of the end of a 60 nm radius, 3° half cone angle nanopipette in the bulk and close to a charged surface were constructed to understand the theoretical basis of the ion current response. Simulations were constructed in Comsol Multiphysics using the Nernst-Plank and electrostatics modules.

6.3 Results and Discussion

The current-potential characteristics of a typical 60 nm radius nanopipette in the bulk aqueous 10 mM KCl solution are shown in Figure 6.3. As expected, these nanopipettes show slight ICR due to the negative surface charge at the walls of the nanopipette,[175,236] with the current magnitude at positive values of the applied potential ($V_{QRCE,nanopipette}$ - $V_{QRCE,bulk}$) being less than the current magnitude at negative potential values, as discussed in some detail in the literature,[174,235,236,246,247] and briefly below. The additional effect of a charged surface on the DC and AC ion currents in SICM is investigated herein.

6.3.1 Approach Curves

The nanopipettes, operated in distance-modulation mode, were translated towards various surfaces in 10 mM KCl. The procedure outlined in the section Section 6.2.3 ensured that the nanopipette-surface distance was consistent at different potentials on a particular surface, with sets of curves obtained with one nanopipette. It should be noted, however, that the closest nanopipette-surface distance is not the same for different surfaces due to the intrinsic charge

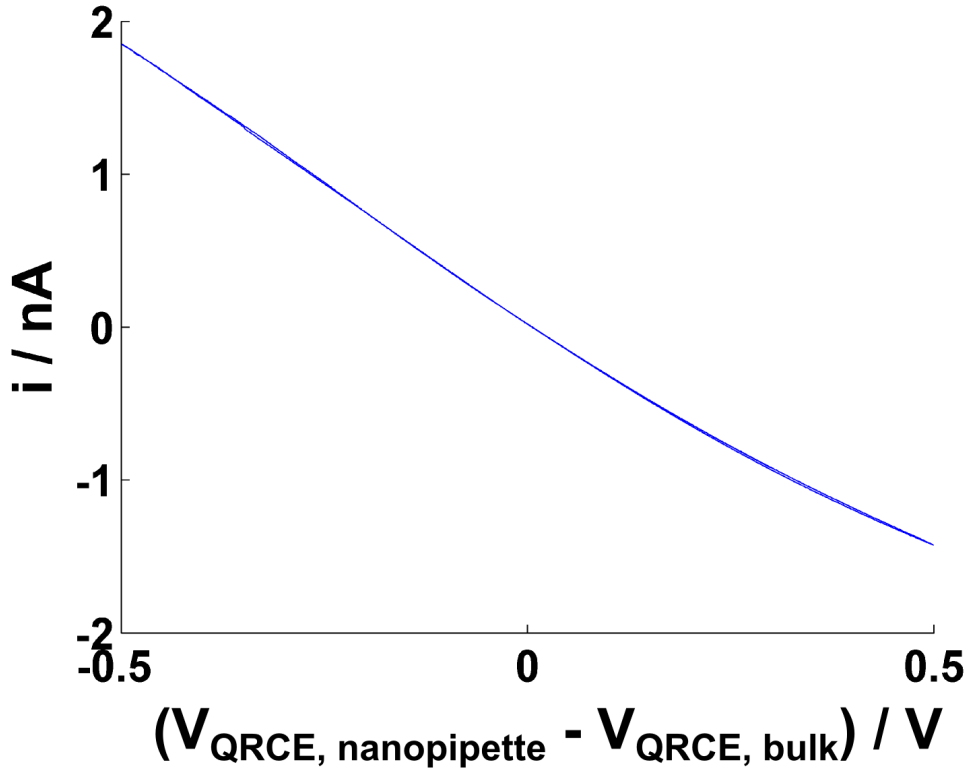

Figure 6.3: Typical current-potential response of a nanopipette of 60 nm radius in a 10 mM KCl solution.

characteristics of samples (*vide infra*). For convenience, nanopipette-surface distances are assigned with respect to the point of closest approach, which can reasonably be expected to be within tens of nanometers of the surface itself, for all surfaces, as the ion current changes predominantly within a distance of a probe diameter from the substrate.[248] As could be expected, at a very small nanopipette-surface separation (data not shown) the drop of the ionic current was observed regardless the nature of the substrate. The ion current, normalized with respect to the ion current in the bulk, for approach curves towards glass, polystyrene and APTES are shown in Figure 6.4 (A)-(C), respectively. The glass provides a negatively charged surface (typically *ca.* -1 mC m^{-2} in 10 mM KCl, or -6×10^{-3} e nm^{-2}, where e is the electric charge of a proton),[175,237,249] the polystyrene acts as a neutral surface and APTES a positively charged surface.[250] Absolute values of a surface charge density depend on a number of factors: the particular type of substrate (*e.g.* different

types of glass), the surface pretreatment protocol employed, surface cleanliness, sample ageing with time and the surface environment (*e.g.* electrolyte concentration, pH, etc.).

In this work a moderate (and typical) surface charge among a wide range reported is chosen. On negatively charged glass (Figure 6.4 (A)) the ion current shows an increase in magnitude as a function of decreasing nanopipette-surface distance at negative potential differences ($V_{QRCE,nanopipette}$ - $V_{QRCE,bulk}$) while there is a decrease in current with smaller nanopipette-surface distance at positive potential differences. This pattern is similar on the polystyrene surfaces (Figure 6.4 (B)), although the changes in the ion current with distance are greatly diminished compared to the behavior seen with the glass surface. Conversely, over the positively charged APTES surface (Figure 6.4 (C)) an increase in ion current with decreasing nanopipette-surface distance is observed at positive ($V_{QRCE,nanopipette}$ - $V_{QRCE,bulk}$) potentials, while there is a decrease in ion current with nanopipette-surface distance at negative potentials. Thus, the trend in the current-distance curves with respect to potential is opposite to that seen with the negatively charged glass surface and neutral polystyrene-covered surface. The general observation is that the SICM ion current over charged interfaces depends on the bias polarity between the two QRCEs and the charge on the substrate, as recently reported, primarily through nanopore simulations.[237] In this contribution we describe *surface-induced rectification* at nanopipettes with a primary emphasis on high resolution scanning to probe and map surface charge effects with high sensitivity using both the DC and AC components of ion current.

The origin of the surface-induced polarity-dependent ion current is the interaction between the DDL at the nanopipette and the DDL at the substrate, combined with the asymmetry of mass transport inside and outside the nanopipette. In the case of a negatively charged glass or quartz nanopipette in the bulk solution, the interaction of the DDLs formed at the side walls of the nanopipette create a perm-selective region at the end on the nanopipette in which the migration and diffusion of cations dominates. Mass transport inside the

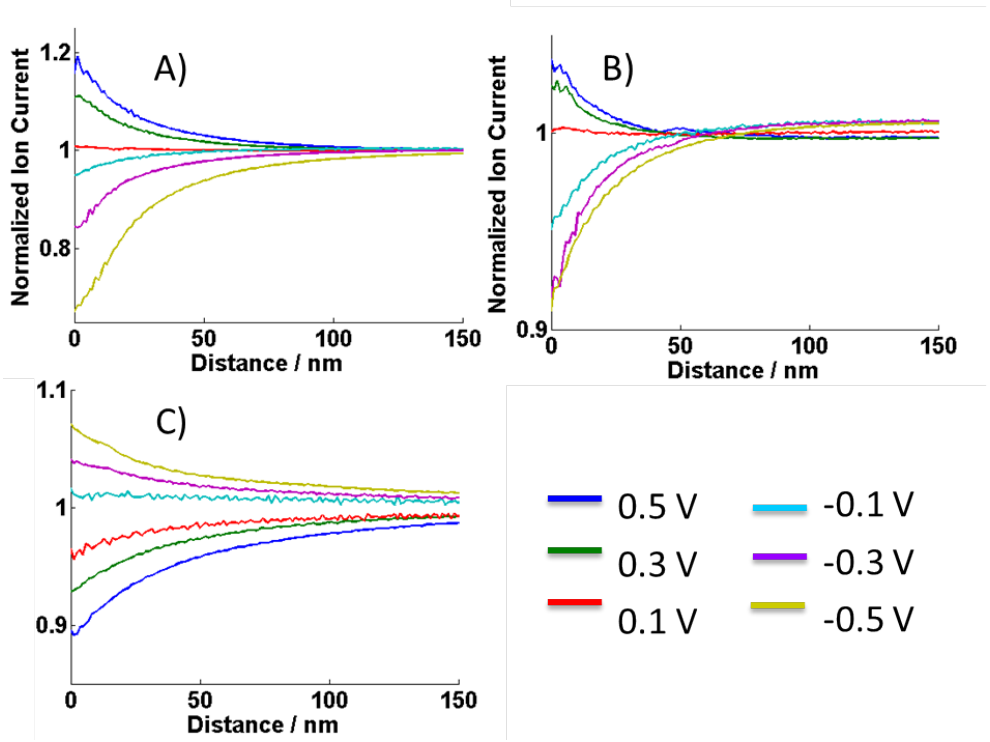

Figure 6.4: Normalized ion current as a function of nanopipette-surface distance at different potentials over (A) glass, (B) APTES and (C) polystyrene recorded in a 10 mM KCl solution with a 60 nm radius nanopipette, with an oscillation amplitude of 10 nm at 288 Hz.

nanopipette is limited by the conical geometry, while the outer space near the tip provides a much faster transport due to a larger access angle. At a positive bias cations are pushed from the nanopipette and the faster mass-transport rate outside the tip opening leads to the depletion of ion concentration inside the nanopipette (as shown from FEM simulation results in Figure 6.5(A)) giving rise to a low-conductance state and diminished ion current magnitude. At the opposite (negative) bias cations are pushed towards the nanopipette at higher rates than they are transported inside, resulting in ion accumulation within the nanopipette yielding a high-conductance state and an enhancement of the ion current magnitude (Figure 6.5). This effect is subtle with this size nanopipette with 10 mM KCl, yet detectable (Figure 6.3).

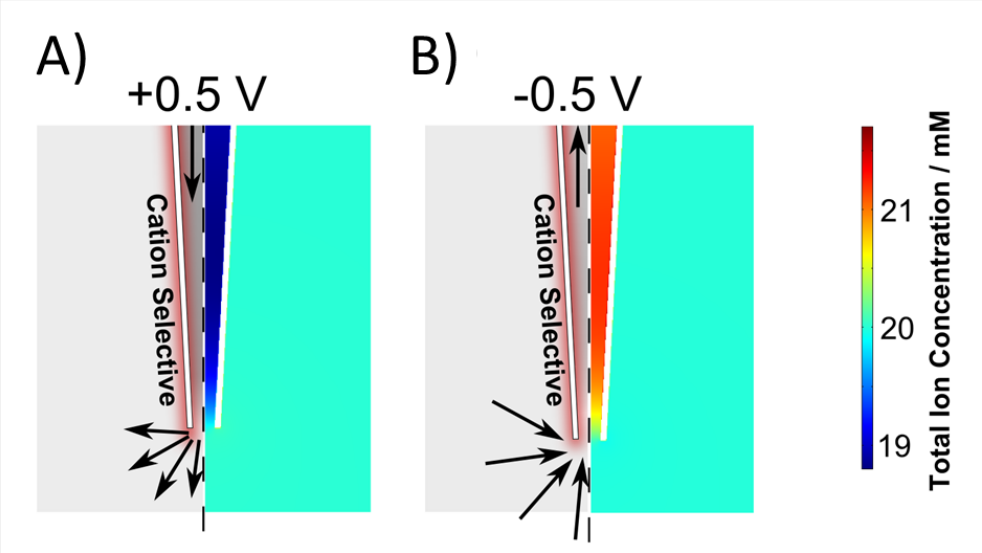

Figure 6.5: Schematic of the DDL and direction of cation transport (on the left of each subsection, mass-transport of cations is denoted with arrows) and FEM simulation total ion concentration profile (on the right of each subsection) showing the low (A, bias of +0.5 V) and high (B, bias of -0.5 V) conductance states of a nanopipette in a bulk solution of 10 mM KCl (total ion concentration 20 mM).

With a nanopipette approaching the charged surface, the rectifying scenarios are seriously affected by the presence of DDLs at the substrate, which exhibit perm-selective behavior towards cations or anions depending on the sign of the surface charge. It is therefore important to consider two coupled perm-selective regions: the one inside the nanopipette as in classical rectification and the one between the surface and the end of the nanopipette. When the DDLs at the nanopipette and the surface consist of similar counter-ions (*e.g.* both the nanopipette and the substrate are negatively charged, Figure 6.6 (A)-(B)), both the nanopipette and surface have similar perm-selective properties. In this case, cation-selectivity of the interface gives rise to a build-up of high- and low-conductance states in the nanopipette, at negative and positive nanopipette bias, in a very similar way to a classical ICR, but the accumulation/depletion of ions occurs not only inside the nanopipette but also in a perm-selective zone between the end of the nanopipette and the interface. Thus, ion concentration enhancement/depletion giving rise to the ICR effect is magnified (compare Figure 6.5 with Figure 6.6). As a consequence, and as

shown by the simulations, a surface-mediated enhancement of local ion concentration (and hence ion current) occurs at negative bias (Figure 6.6 (B)), and a surface-mediated decrease of ion current is expected at positive bias on the basis of the ion concentration profile in Figure 6.6 (A) for the glass nanopipette approaching a glass substrate.

Over uncharged substrates there is a similar effect, but of smaller magnitude. With charge solely on the nanopipette, there is only a weak cation-selective region between the nanopipette and the substrate. As shown by FEM simulations, this causes the formation of low-conductance (Figure 6.6 (C)) and high-conductance (Figure 6.6 (D)) states inside the nanopipette and between the nanopipette and the surface, but the intensity of the effect is significantly smaller (less perturbation of the total ion concentration from the bulk value) compared to a negatively charged interface.

The significant influence of the surface charge for determining the rectifying characteristics in SICM is demonstrated on Figure 6.6 (E) and (F), for the case of the nanopipette tip in the vicinity of a positively charged interface. This case is especially interesting because the nanopipette and the interface exhibit the opposite perm-selective behavior, *i.e.* cation selectivity inside the nanopipette versus an anion selective DDL at the surface. The inversion of rectifying properties with bias seen in Figure 6.4, can evidently be attributed to the inversion of the low- and high-conductance states in the nanopipette with respect to nanopipette polarity. The anion-selective region at the surface plays the key role in this effect at this charge density (5 mC m^{-2}). The simulation results (Figure 6.6) are in a good agreement with experimental results depicted on Figure 6.4 and with recent theoretical studies of surface-induced rectification which employed a simpler geometry and lower electrolyte concentration.[237] The agreement between experiment and the model is important because another recent report observing a polarity-dependent ion current signal over charged surfaces attributed the rectifying properties to the emergence of an electro-osmotic flow separation phenomenon.[251] The latter report described the surface-induced ion current enhancement at much higher electrolyte concentrations (150 mM NaCl), and even though the nanopipettes were smaller (15 nm radius) they would exhibit much weaker perm-selective prop-

erties. Our results (in electrolyte solutions of relatively low ionic strength) demonstrate that rectification is due to the presence of a surface charge and diffusion/electromigration effects, which are sufficient to explain the experimental observations.

Our studies now turn to the AC ion current components, induced by the oscillating nanopipette, recorded in parallel with the ion current shown in Figure 6.4. As highlighted earlier, although distance modulated SICM is becoming a widely used technique,[67] these parameters (especially the phase) have not been studied or analyzed in detail previously, but provide rich information on interfacial properties (*videinfra*). Irrespective of the surface, the AC current amplitude increases as the nanopipette-surface distance decreases (Figure 6.7). The AC ion current magnitude at a particular distance represents the absolute change in ion current as the nanopipette-surface distance is modulated (by 10 nm herein) at that distance, and is therefore related to the magnitude of the slope of the DC ion current, with respect to distance. The AC magnitude thus tends to increase as the nanopipette approaches a surface. This signal is typically used as a means of the nanopipette detecting a surface,[67] and any surface charge effects are evidently obscured. However, the phase of the AC ion current can also be recorded and we now show that this signal can be used to detect the surface charge with high sensitivity.

The periodic (time, t) change in the nanopipette-surface distance, z (with amplitude A and frequency f) with respect to the interface,

$$z = Asin(2\pi ft) \tag{6.1}$$

leads to a harmonic oscillation in the ionic current, I_{AC}, (under the assumption of a small amplitude of distance modulation)

$$I_{AC} = \alpha Asin(2\pi ft + \varphi) \tag{6.2}$$

where α is the slope of the current-distance curve. Hence, the harmonic ion current signal would be expected to be in-phase with the driving vertical position oscillation (phase shift $\varphi = 0°$) at positive α (DC ion current drops

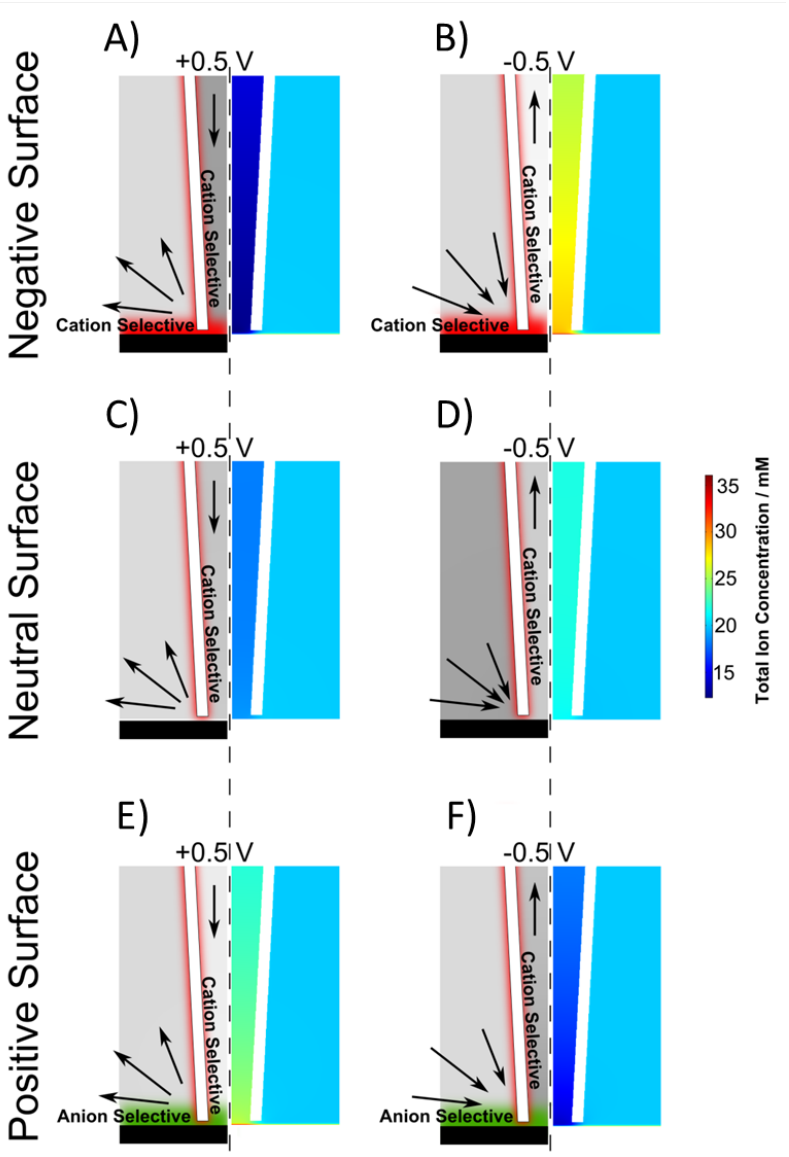

Figure 6.6: Schematics of cation mass transport flux (indicated by the arrows) and perm-selective regions (red, cation selective; green, anion selective) at the negatively charged nanopipette, and substrates of different charge (on the left of each part) and FEM simulation results (on the right of each part) of the resulting ion concentrations near the end of a nanopipette at surfaces. The nanopipette walls were 30 nm thick, and the nanopipette was 10 nm from the surface. Data are for a negatively charged surface (5 mC m^{-2}) at applied potentials of (A) 0.5 V and (B) 0.5 V, inside the nanopipette with respect to the bulk; a neutral surface at (C) 0.5 V and (D) 0.5 V, inside the nanopipette with respect to the bulk; a positively charged (+5 mC m^{-2}) surface at (E) 0.5 V and (F) 0.5 V, inside the nanopipette with respect to the bulk.

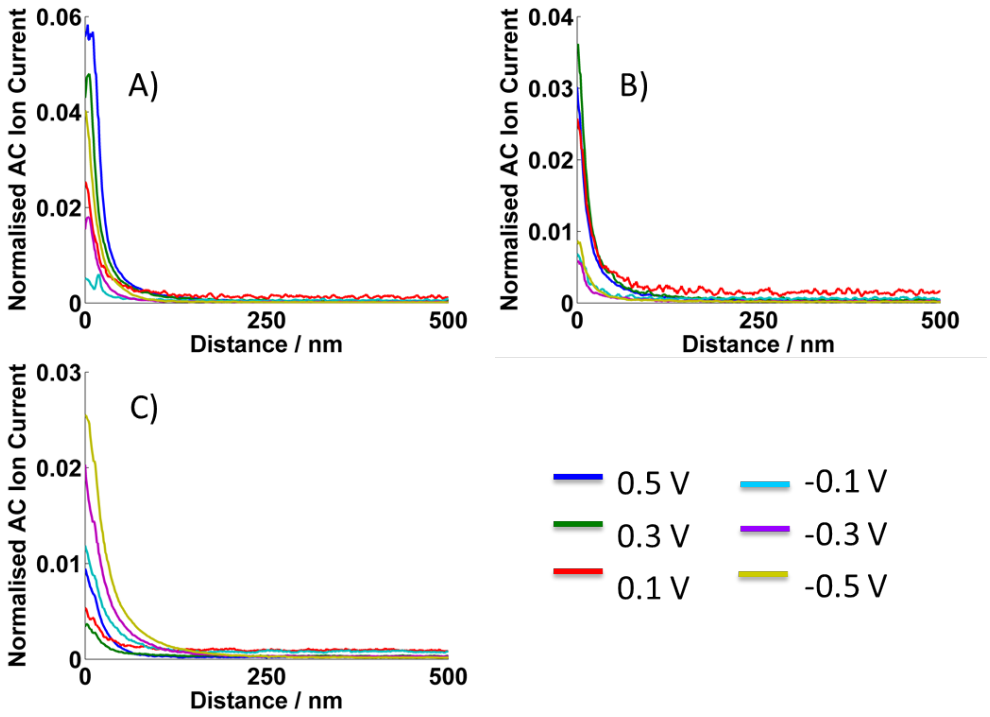

Figure 6.7: Normalized AC ion current magnitude (normalized with respect to the DC ion current, as a function of nanopipette-surface distance and potential, recorded concurrently with the data in Figure 6.4, over (A) glass, (B) polystyrene and (C) APTES, recorded in a 10 mM KCl solution with a 60 nm radius nanopipette oscillated 10 nm at 288 Hz.

in the vicinity of the substrate) or counterphase ($\varphi = 180°$) at negative α (ion current increase near the substrate), while at large separation distance, $\alpha = 0$, *i.e.* there is no AC amplitude or phase shift. However, the experimental phase shifts measured in parallel with the DC and AC ion currents for glass, polystyrene and APTES (as summarized in the polar plots in Figure 6.8 (A)-(C)) are never strictly in-phase or counterphase with respect to the driving oscillation and take intermediate values between 0° and 180°. Within the polar plots in Figure 6.8 (D)-(F) each data point from an approach curve is displayed at a coordinate with its radius defined by the normalized AC ion current magnitude (the larger the current value, the closer the nanopipette is to the surface), and the angle with respect to the positive horizontal axis defines the phase shift, φ. These features are labelled in Figure 6.8.

At relatively large nanopipette-to-substrate distances the AC ion current was negligible and so the traces were centered close to the origin (and largely contained experimental noise). Interestingly, at closer nanopipette-surface distances, where an appreciable AC ion current was generated, the phase shift over each of the three surfaces correlates with the respective ICR behavior. Over all surfaces the phase was smallest (*ca.* 10° over glass and polystyrene, and *ca.* 30° over APTES) when the ion current magnitude decreased with decreasing nanopipette-surface distance ($V_{QRCE,nanopipette}$ - $V_{QRCE,bulk}$) = 0.5 V over glass and polystyrene and at -0.5 V over APTES), while the highest φ values were associated with ion current enhancements at close nanopipette-surface distances, ($V_{QRCE,nanopipette}$ - $V_{QRCE,bulk}$)= -0.5 V over glass and polystyrene, and 0.5 V over APTES).

These experimental findings indicate that the phase shift is intrinsically sensitive to the interfacial charge and therefore ionic transport properties at selective biases. When the pipette approaches towards a charged surface, the mass-transport inside and immediately outside the pipette tip may be significantly affected by the double layer at the interface. Under conditions where the surface acts to strengthen a low-conductance zone inside and immediately outside the pipette, the electrical resistance within these regions increases due to ionic depletion. If the concentration depletion can respond on the timescale of the perturbation (i.e. the ionic redistribution is fast enough compared to

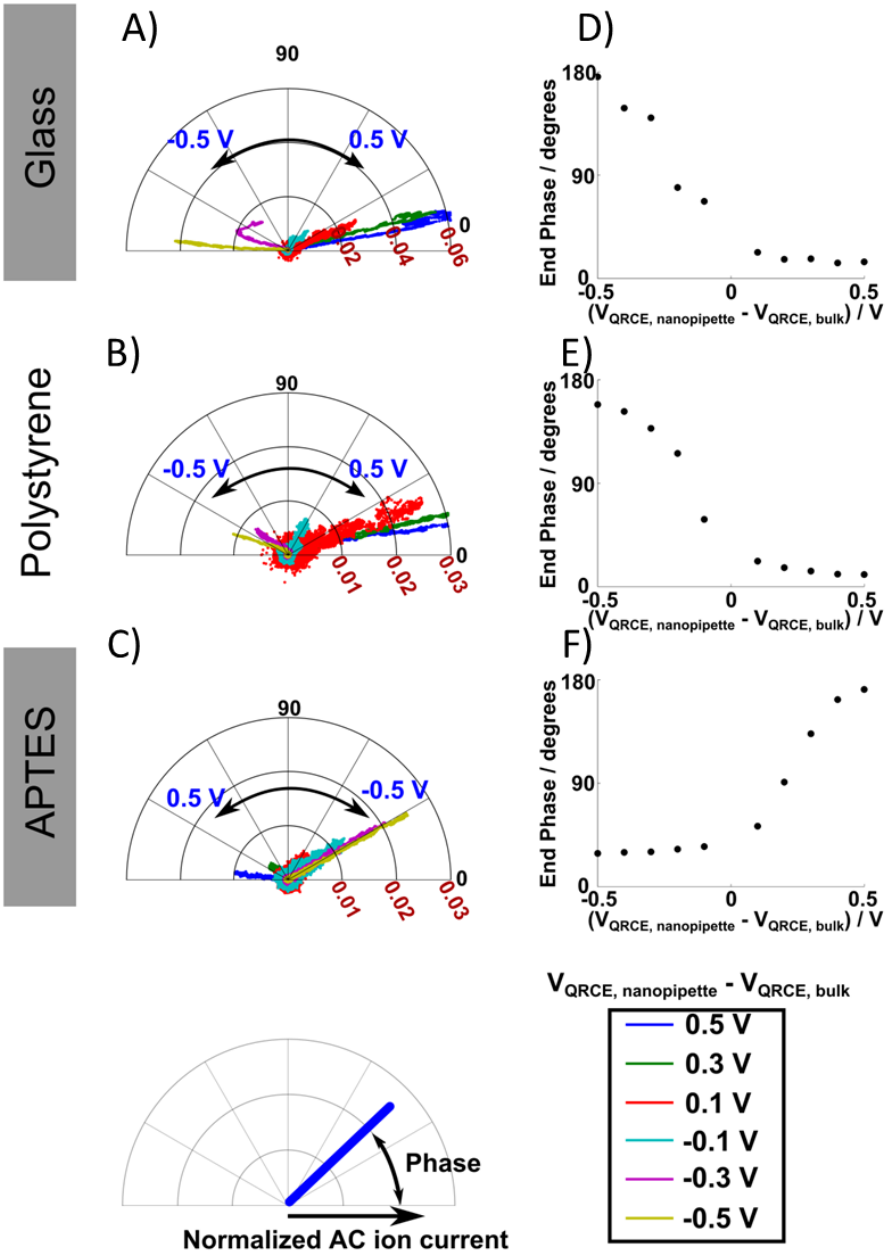

Figure 6.8: Polar plots, with the distance from the origin defined by the AC ion current magnitude normalized by the bulk DC ion current and angle defined by the ion current phase (as shown in the insert diagram at the bottom left) of the AC ion current over (A) glass, (B) polystyrene and (C) APTES substrates. Data obtained in 10 mM KCl solution with a 60 nm radius nanopipette oscillated with an amplitude of 10 nm at 288 Hz. The phase value at the smallest nanopipette-surface distance with respect to the applied bias on (D) glass, (E) polystyrene and (F) APTES.

the nanopipette oscillation rate), then the resulting ionic current would be in-phase with the pipette movement. It has recently been reported, by experiment and simulation of the bias-scan rate dependent ion current in a nanopore in the bulk solution,[252,253] that the high- and low-conductance states take 1-10 ms to build up (for nanopipettes and conditions similar those herein). If the ionic redistribution is slow compared to the timescale of the oscillation, then the ion depletion zones have insufficient time to adjust upon nanopipette approach to (or retract from) the substrate. In this case, the electrical resistance in the nanopipette-substrate gap would still increase upon approach but in a way more similar to classical SICM (due to a hindered mass-transport in the vicinity from a surface). Therefore, the resulting currents are still in-phase with the vertical pipette movement. In contrast to the surface-induced low-conductance (above), where the AC current will always tend towards a 0° phase shift, a surface-enhancement of mass-transport (conductance) can have a different effect on the AC phase shift depending on the experimental conditions and, in fact, is very sensitive to surface charge properties. Under these conditions, the phase shift response can vary from in-phase (φ= 0°), when the ion current redistribution is slow compared to the nanopipette oscillations (for the reasons described just above), to counter-phase (φ= 180°), when the ion redistribution occurs much faster than the nanopipette movement and thus electrical conductivity inside and near the nanopipette tip is always close to a steady-state. When the ion redistribution rate is similar to the rate of nanopipette movement then the phase of AC ion current takes intermediate values between 0° and 180°. This hypothesis is in a good agreement with phase data presented in Figure 6.8.

The phase AC components of ionic current strongly depend on surface-induced rectification: over all three surfaces bearing negative, neutral and positive surface charge, the phase is minimal under conditions leading to a surface-induced ion depletion and ionic current decrease with decreasing nanopipette to substrate distance (see also approach curve data on Figure 6.4), while the ion current enhancement at surfaces always leads to a phase increase up to *ca.* 180° (a counter-phase phase shift responses). Therefore, the AC ion currents are always dependent on a few effects: the surface charge sign, charge magnitude, the applied bias, and the resulting time constant of ion redistribution that

can be the function of the aforementioned factors. With the analysis herein, experiments can be tuned (nanopipette bias, frequency, nanopipette-substrate distance, electrolyte concentration, etc.) to be sensitive to surface charge and/or topography. Based on the results in Figure 6.3 (discussed above), this would tend to give rise to a periodic change in the conductance strength inside the nanopipette, and in the nanopipette-substrate region. The phase shift is then closely related to the time constant of ionic mass-transport required to change the conductance strength and vary bias sensitive.

6.3.2 Surface Charge Mapping

To demonstrate the newfound capabilities of distance-modulated SICM for high-resolution interfacial charge imaging, a surface consisting of a thin polystyrene film with holes revealing the glass substrate underneath was mapped in a hopping mode.[67,172] The nanopipette was repeatedly approached to the surface of the sample using the AC ion current amplitude with a set point of 4 pA (for positional feedback). Once the set point was reached, the nanopipette was retracted and then laterally moved by 250 nm to the next point, in this way forming a 5 µm by 5 µm image. The ion current (both DC and AC) was measured as a function of nanopipette vertical position during each approach and the last data point (closest to the surface) of each was used to construct two-dimensional maps. As shown above (Figure 6.4) both the glass and polystyrene substrates cause DC ion current enhancement at the same polarity (negative values of $V_{QRCE,nanopipette}$ - $V_{QRCE,bulk}$). Therefore, for imaging purposes, a fixed potential of -0.3 V was applied to the nanopipette, where the phase shift would be most sensitive to interfacial charge (*vide infra*).

Figure 6.9 (A)-(C) shows typical results: a normalized DC ion current map, a phase map, and topography map (determined from the position at which the surface was detected) recorded simultaneously. The normalized ion current reveals the glass exposed by a pore in the film due to the subtle difference in the response of the ion current during the approaches to the two materials, with the glass producing slightly higher surface ion currents compared to the polystyrene, as expected based on the approach curves and simulations in Figure 6.4 and Figure 6.6. The phase map (Figure 6.9 (B)) also

clearly reveals the glass spot but having much higher contrast compared to the DC ion current components. The phase shift tends towards 100° over glass, and is surrounded by the polystyrene, where the phase value is lower. This indicates higher negative surface charge density on the bare glass compared to the polystyrene-coated areas and demonstrates the efficiency of this approach to distinguish subtle surface charge heterogeneities at the nanoscale. A phase difference of >20° between the glass and polystyrene surfaces represents about 1 $\mathrm{mC\,m^{-2}}$ with the surface charges assumed in this work. Given that phase shift can be detected with a resolution of at least 1 degree (and that this could be further improved), this gives an indication of the sensitivity with which surface charge can be detected via phase detection. Moreover, the phase image exhibits similar spatial resolution to the topography image. Any ICR effect seen over the polystyrene is due to the double layer on the glass nanopipette alone, while for the glass there is a surface-induced contribution leading to a noticeably higher phase.

The topography, shown in Figure 6.9 (C), shows the flat glass surface surrounded by an area of polystyrene. This topography was confirmed by AFM (Figure 6.9 (D)) which is seen to be in good agreement. Taken together, the data in Figure 6.9 illustrate that substrate topography and charge can be visualized simultaneously. This is because, as a function of nanopipette-surface distance, the AC magnitude (used as a set point) is surface independent, relative to the scale of the topographical features in Figure 6.9. The ability to deconvolve surface charge and topography involves an interplay between the thickness of the double layer and the tip size. With a decreasing tip size or ion concentration, as well as for substrates with extremely high surface charge density, the contribution of surface charge to the AC magnitude becomes more significant, resulting in a convolution of surface charge and topography. With a trend towards higher resolution imagining in SICM,[172,230,233] this is an effect that needs careful consideration if SICM is to measure true surface topography.

The approach in this paper provides a framework for such an analysis and allows conditions to be identified where surface charge and topography can be resolved. Finally, we mapped a soft polymeric spot with positive charge on a negatively charged background (glass with a 5 m diameter spot of PLL) in

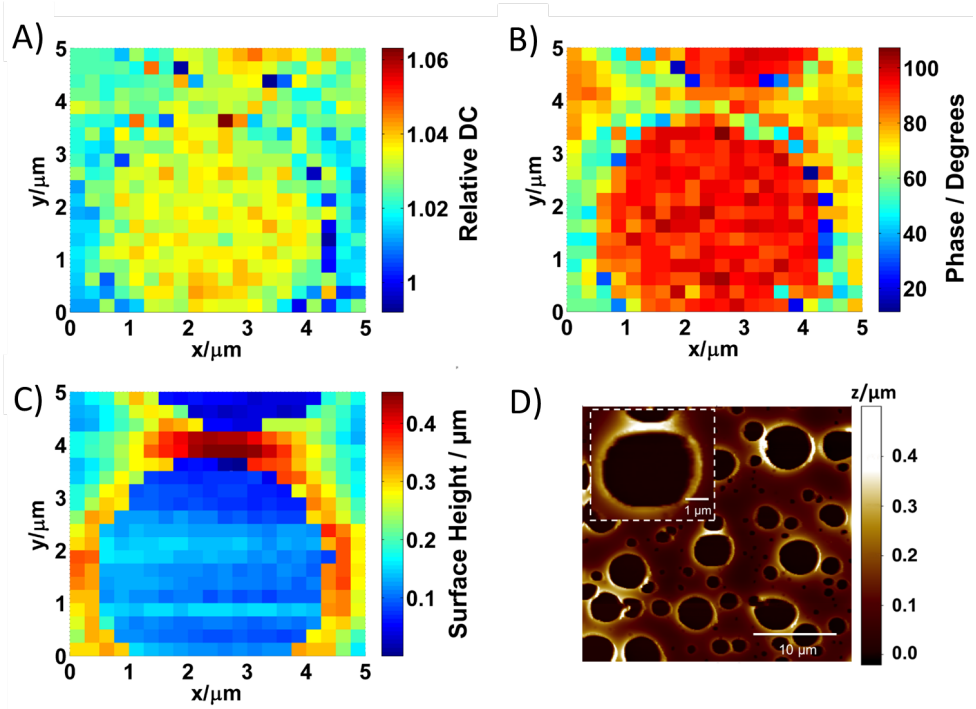

Figure 6.9: Two-dimensional hopping mode SICM images of a glass substrate partially covered with a thin polystyrene film. The images display the following ion current components recorded simultaneously, with an applied bias of 0.3 V: (A) normalized (with respect to the bulk) DC ion current; (B) phase; (C) topography. A topographical image of a typical surface as determined by AFM is shown in (D).

a hopping mode, with a step size of 1 m. Imaging was carried out twice with the same nanopipette, first with a potential ($V_{QRCE,nanopipette}$ - $V_{QRCE,bulk}$) of 0.2 V and then with a potential of -0.2 V. Figure 6.10 shows the results of the two maps, with the PLL spot on a glass surface apparent in both the normalized ion current ((A) and (E)), phase ((C) and (G)) and topography ((D) and (H)) maps. Similar to the charge mapping above, the AC ion current magnitude (4 pA), not shown, was used as the feedback parameter to detect the surface. The normalized ion current, Figure 6.10 (A) and (E) for 0.2 V and -0.2 V, respectively, both reveal the PLL spot. At 0.2 V ($V_{QRCE,nanopipette}$ - $V_{QRCE,bulk}$) the DC ion current is higher over the PLL spot than the glass, but at -0.2 V this is reversed, as expected due to the polarity dependence of the ion current response over the positively charged PLL and negatively charged glass surface. Typical approach curves over the PLL spot, and over

the glass, at the two bias values are shown in Figure 6.10 (B) and (F). These approaches were taken at the marked positions in Figure 6.10 (A) and (E). At a bias of 0.2 V ($V_{QRCE,nanopipette}$ - $V_{QRCE,bulk}$) the approaches over both glass and PLL decrease, but over PLL the current is higher. In contrast at -0.2 V ($V_{QRCE,nanopipette}$ - $V_{QRCE,bulk}$) the ion current is higher over glass.

The phase shift of the ion current also shows the PLL spot very clearly. The difference in AC phase over the positively charged spot, compared to the surrounding negatively charged glass, is *ca.* 20° in both maps, but the sign of the change is bias-dependent. This makes the AC phase an especially sensitive and useful parameter for nanoscale surface charge measurements. The topography, determined from the position that the surface was detected, is largely consistent at each bias (Figure 6.10 (D) and (F)). This reveals that the PLL has deposited from the 5 µm diameter droplet in a coffee ring format.[254] The consistency of the topography at difference bias, together with the bias dependent phase (in particular) and ion current response, again highlights the capabilities of SICM for simultaneous topographical and charge mapping.

6.4 Conclusions

In solutions of moderate to low electrolyte concentration, the ion current (and alternating ion current) through a nanopipette is surface and potential dependent. This is primarily due to the creation of a perm-selective region between the nanopipette and the surface due to the interactions of the diffuse double layers at the substrate and the nanopipette, coupled with an asymmetry in mass-transport rates inside and outside the nanopipette. The ion current depends on the polarity. Indeed, the ion current can increase as the nanopipette-surface distance decreases: at negative biases ($V_{QRCE,nanopipette}$ - $V_{QRCE,bulk}$ <0) over negatively charged substrates and at positive biases ($V_{QRCE,nanopipette}$ - $V_{QRCE,bulk}$ <0) over positively charged substrates. For distance-modulation SICM there is a significant phase shift of the AC ion current component, which is highly sensitive to the diffuse double layer of the substrate surface. Aided by these findings, we have shown that nanopipettes can be used to map the charge at solid-liquid interfaces in electrolyte solutions with the possibil-

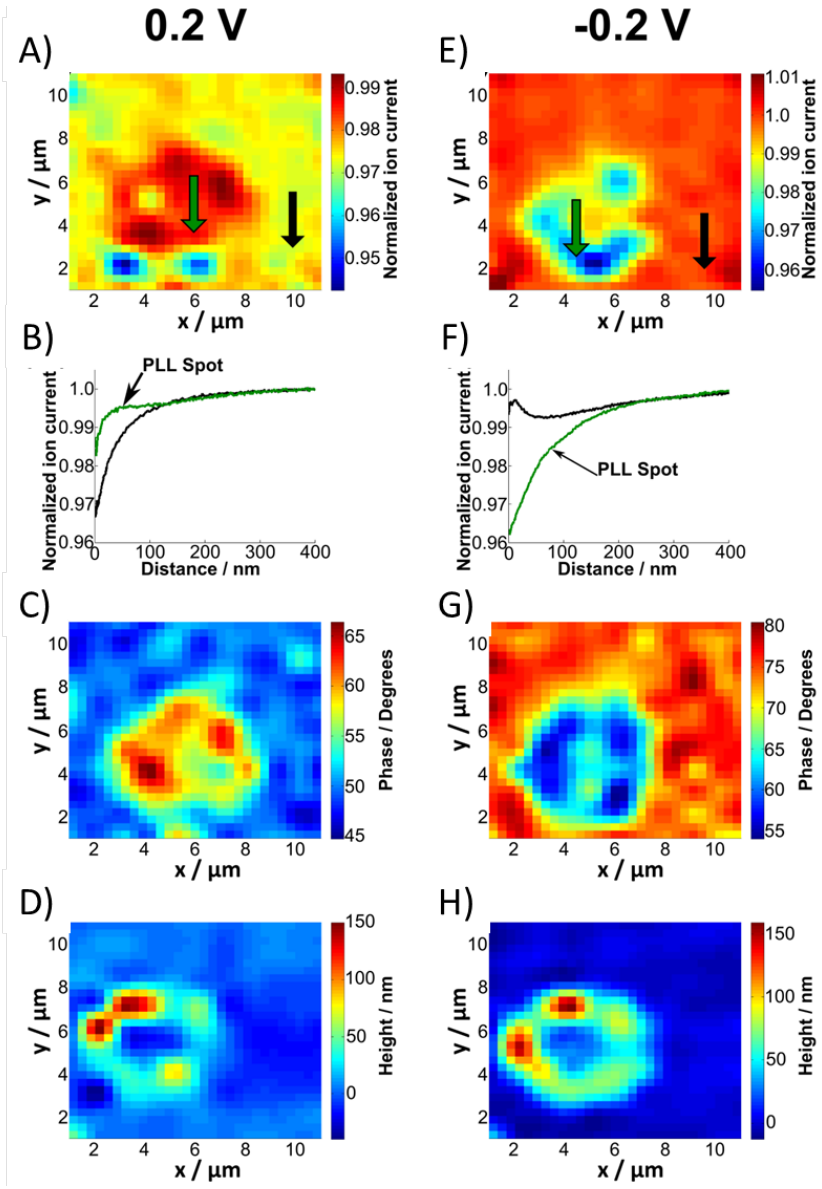

Figure 6.10: Hopping mode images, with 1 µm resolution, of a PLL spot (positively charged) on a glass substrate (negatively charged) with a bias of 0.2 V (left) and -0.2 V (right), applied to the QRCE in a 60 nm radius nanopipette with respect to a bulk QRCE in 10 mM KCl. The normalized ion current at the 2 different applied potentials is shown in (A) and (E). Typical approach curves, at each potential, over the PLL spot (green) and over glass (black) are shown in (B) and (F). Phase maps are shown in (C) and (G). The surface topography, determined from the position that the surface was detected, are shown in (D) and (H). Note that the 2D images are interpolated.

ity of performing topographical and functional (surface charge heterogeneity) analysis simultaneously. This expands SICM beyond its main application of non-contact mapping of substrate topography and brings new multifunctional capability.

In addition, our work has the implications for the capability of SICM to map true surface topography, especially with very small nanopipettes. This analysis of the technique provides a guide for the design and execution of optimal SICM experiments, depending on the application and information sought. We have highlighted the ability of a nanopipette to detect surface charge variations semi-quantitatively for surfaces and interfaces with rather modest charge densities. With further simulations it should be possible to extract quantitative surface charge values with good precision and further optimize the technique. Practically, an important feature of the approach described is that the nanopipette in the bulk solution can be checked regularly during a scan (especially in hopping mode where pixel level calibration is possible). The ability to check the nanopipette and measure its charge characteristics in this way is particularly advantageous compared to other techniques for surface charge mapping such as AFM.

6.5 Acknowledgements

We thank the European Research Council (ERC-2009-AdG247143-QUANTIF) and the EPSRC (through the MOAC DTC) for funding. We are also grateful to Alex W. Colburn (University of Warwick) for custom built electronics.

Chapter 7

Dynamic Nanoscale Surface Charge Mapping at Ultramicroelectrodes

Bias modulated-scanning ion conductance microscopy (BM-SICM) was used to probe the diffuse double layer (DDL) at the liquid-liquid interface between a Hg ultramicroelectrode (UME) and an aqueous solution. In this work, we report the detection of surface charge densities as low as 1 $\mu C\,cm^{-2}$ *via a three-electrode setup in which the potential applied to the substrate (and thus the charge of that substrate) can be varied with negligible contribution to the current measured in the nanopipette. It is shown that it is possible to detect changes in the surface charge density in real time as the bias between the UME and a reference electrode in bulk solution is swept in a cyclic voltammogram regime. The technique is shown to be responsive to changes in surface charge for both simple (Hg droplet electrode) and complex (self-assembled monolayers on Pt) systems.*

7.1 Introduction

The surface charge at interfaces is of great importance in fields as diverse as colloidal science[255–258], mineralogy[259–262] and proteomics[258,263,264]. Yet it is often overlooked, in part due to the lack of robust techniques to probe the sur-

face charge. Most electrochemical measurement work under the assumption that the diffuse double layer (DDL) at the interface is of negligible thickness due to a large concentration of supporting electrolyte. However, the recent rise of nanoscale electrical devices, batteries[265] and supercapacitors[266,267] does not allow consideration of the DDL to be omitted, due to the ever decreasing size of the structures used in such devices. The work of White *et al.*[268] has showed that these systems are more complicated than once thought, demonstrating the effect of the double layer on ion transport in nanogap electrochemical cells.[269] It is clear that the charge density on conducting surfaces is not yet fully understood, particularly in the case of an applied voltage. A better understanding of double layer effects in these systems would facilitate design of more efficient devices in the future. It has recently been shown that bias modulation-scanning ion conductance microscopy (BM-SICM) employed in low concentration electrolytes (<10 mM) is a powerful tool for nanoscale probing of the DDL, and thus the surface charge, at an interface.[270] Only interfaces with a fixed chemical surface charge have thus far been probed, showing clearly that it is possible to distinguish between positive and negatively charged surfaces and probe acid-base equilibria.[270,271] In this report we investigate the effect of changing the applied voltage on the double layer of an ultramicroelectrode (UME) substrate, thus developing a semi-quantitative technique for dynamically measuring the surface charge density at an interface. We demonstrate this concept on an ideally polarizable hemispherical Hg electrode[163,164,272], showing real time resolution of the changing surface charge, and also apply the technique to more complex substrates, namely a self-assembled monolayer (SAM) coated Pt UME.

7.2 Experimental

7.2.1 Electrodes

Pt UMEs were fabricated according to the method previously described.[176] Briefly, a 25 µm diameter Pt wire was sealed in a borosilicate capillary (OD 2.0 mm. ID 1.16 mm, Harvard Apparatus) and then polished to give a disk-in-disk geometry before use. For experiments with Hg, a droplet of Hg was formed on

top of the Pt UME by electrodeposition from the solution described above.[273] The Pt UME was polished directly prior to deposition, it was suspended in the deposition solution with a Ag wire acting as a counter electrode. A voltage of +0.3 V was applied to the UME until the current had increased in magnitude by a factor of $\pi/2$, the difference between planar and hemispherical diffusion. For experiments on functionalised Pt, a methyl-terminated SAM was formed on top of the Pt UME via suspension in an isopropyl alcohol solution of 200 mM 1-dodecanethiol for a minimum of 24 hours.[274] Prior to functionalization, UMEs were cleaned by cycling their potential in a perchloric acid solution (0.5 M) for 15 minutes.[8] Ag|AgCl Quasi-reference counter electrodes (QRCE) were fabricated by chlorodizing a length of Ag wire.

7.2.2 Nanopipettes

All nanopipettes used in this work were fabricated from borosilicate capillaries (Harvard Apparatus), containing a filament to aid filling them with aqueous solution. The capillaries were pulled to a sharp tip using a laser puller (P-2000, Sutter Instruments, using a two line program. Pulling parameters for both lines: Heat 350/350, Fil 3/3, Vel 30/40, Del 220/180, Pul -/120). The probe dimensions were investigated by transmission electron microscopy (JEOL 2000FX) and the radius of the probes was found to be 90 ± 5 nm (Figure 7.1(C)).

7.2.3 Bias Modulated-Scanning Ion Conductance Microscopy Instrumentation

The experimental setup builds on recent work using BM-SICM.[98] The UME is mounted, upside down, in a bath of the desired electrolyte. Lateral movement of the substrate is controlled using a two-axis piezoelectric positioning system with a range of 300 µm (Mad City Labs Inc.) The probe moved in the Z axis only, using a piezoelectric positioning system with range of 38 µm (Physik Instrumente) The bottom of the UME is sealed with wax to prevent leaks. A novel three-electrode setup was used as shown in Figure 7.1(A). This allowed the probe to sense only the double layer without contribution to the current from the UME. The probe is held at ground with respect to the reference elec-

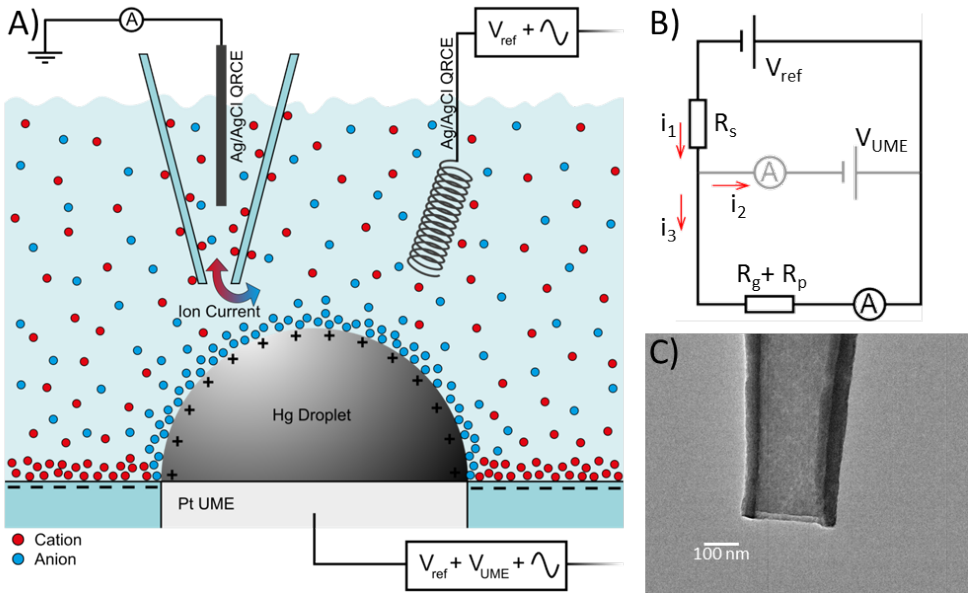

Figure 7.1: A) The three-electrode setup used during the experiments. A droplet of Hg is deposited on a Pt UME and used as a substrate. V_{UME} applies oscillating bias between the reference and UME. V_{ref} offsets both the UME and reference with respect to the probe. SICM probe approaches the surface, simultaneously measuring the response in ion current and AC phase. B) A schematic of the system, where i_1 is the total current through the reference electrode, i_3 is the current between the probe and the reference and i_2 the current between the UME and the reference. The resistance of the solution (R_S) is negligibly small in comparison to that of the probe opening (R_p) and the gap between the probe and the substrate (R_g). C) TEM image of a typical probe used in the experiments.

trode and the UME is held at 0 V with respect to the reference electrode and can be offset using V_{UME}. An oscillating bias is added to V_{ref}, this is the bias between the probe and the reference. The result is that $V_{ref-probe} = V_{ref}$ + Modulation and $V_{ref-UME} = V_{UME} + V_{ref}$ + Modulation. A lockin amplifier (SR830, Stanford Research Systems) was used to generate the oscillating signal for BM-SICM approaches and to extract the phase and amplitude of the AC ion current, while a custom built current-to-voltage converter was used to measure currents. It was found that the noise in the AC phase is greatly reduced if the potential applied to the UME is modulated to match the reference electrode. The frequency of the modulation was 270 Hz. This value was chosen as previous work showed that this frequency is most sensitive to surface charge when using BM-SICM for mapping surface charge on non-conductive surfaces.

The equivalent circuit diagram in Figure 7.1(B) suggests that i_3 has a dependence on V_{UME}. However, the QRCE in the bulk solution (V_{ref}) is several orders of magnitude larger in area than the UME and therefore the UME has a minor contribution to the nanopipette current, represented by the gray line in Figure 7.1(B). With negligible current contribution from V_{UME} the equivalent circuit resembles that of standard SICM, represented by the black lines in Figure 7.1. From this we can conclude that i_3 measured within the detection limits of the experiment will be given mainly by the bias value.

7.2.4 Impedance

All impedance data were collected on a Gamry FAS2 Femtostat. Firstly, a set of potentiostatic electrochemical impedance spectroscopy (EIS) measurements were made to identify a frequency at which to make the Mott-Schotty measurements. The phase measured in a potentiostatic EIS experiment is dependent on the frequency, and by the components in the circuit. The frequency was swept from 1 Hz to 10 kHz. The signal will move into phase, towards 90°or 0°at the point where the phase was only influenced by the capacitance of the double layer and not the resistant in the circuit. With the frequency at which the phase is only dependent on capacitance identified, a number of Mott-Schotty tests were performed. In these experiments, the frequency is now fixed and

the voltage is swept. The minimum of the double layer capacitance should occur at the potential of zero charge.

7.2.5 Experimental Methodologies

For the vertical approaches, an oscillating bias (14 mV rms amplitude, 278 Hz) was applied between the probe and reference QRCE about a mean bias ranging from -0.4 V to 0.4 V. All potentials quoted herein refer to the potential of the QRCE inside of the nanopipette with respect to the reference QRCE in the bulk solution. Nanopipettes were translated towards the Hg hemisphere UME at 300 nm s^{-1} and the DC, AC phase and AC amplitude of the ionic current were recorded simultaneously. The dynamic maps were generated using an 'approach then surface CV' regime, a setpoint in the AC phase was used to find the point of closest approach before a cyclic voltammogram (CV) (0.2 V s^{-1}) was applied to the UME. The scans presented in this work were produced via a hopping mode in which each pixel is an 'approach then surface CV'.

7.3 Results and Discussion

7.3.1 Approach Curves and CVs

SICM has predominantly been used as a topographical technique in relatively high concentrations of electrolyte.[171,231] However, when that concentration is lowered ($\leqslant$ 10 mM), the characteristic Debye length of the double layer in the probe increases, and a non-linear current voltage response is observed as a result of ion current rectification (ICR).[7,235] Furthermore, when the probe-substrate separation is small enough, typically less than one probe diameter, the polarity of the surface can result in current enhancement/diminution, thanks to the double layer regulating the transport of ions into the nanopipette. The combination of this surface induced rectification (SIR) and the ICR allow the detection of the changing nature of the double layer using SICM.[271]

Often in electrochemical experiments, the electrodes used are assumed to be ideally polarizable; though in reality fouling, adsorption, or surface het-

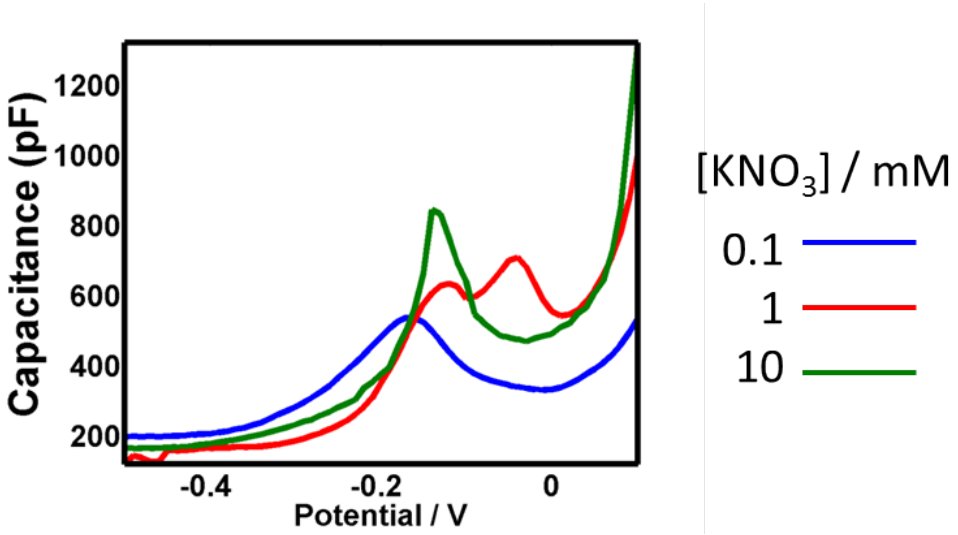

Figure 7.2: Impedance spectroscopy plot of capacitance at liquid-liquid interface between a hemispherical Hg electrode and supporting electrolyte KNO_3 in three different concentrations.

erogeneities as a result of the polycrystalline nature of the conductor used can compromise this assumption. These effects are particularly prevalent in impedance Mott-Schottky measurements, where the contribution from the intrinsic capacitance of the substrate is unknown, often leading to hysteresis of the forward and reverse scans. Herein, we chose to work with a Hg hemisphere as the working electrode, as this will give a close approximation of the ideally polarizable electrode. The setup for all of the experiments described below is given in Figure 7.1. V_{ref} is used to generate a bias between the reference electrode and the probe, making the probe sensitive to the surface charge.[271]

V_{UME} is used to sweep the potential applied to the substrate, continuously changing the surface charge density on the surface. The polarity and magnitude of the surface charge in the system depends on the potential applied to the substrate relative to the potential of zero charge (PZC). In order to see regions of both positive and negative charge in one voltammogram, the PZC of the Hg electrode was determined using impedance spectroscopy (Figure 7.2) and found to be -100 ± 25 mV vs. an Ag|AgCl QRCE.

SICM approaches to the Hg were then carried out with a fixed bias applied to the substrate in order to verify the changing polarity of the surface

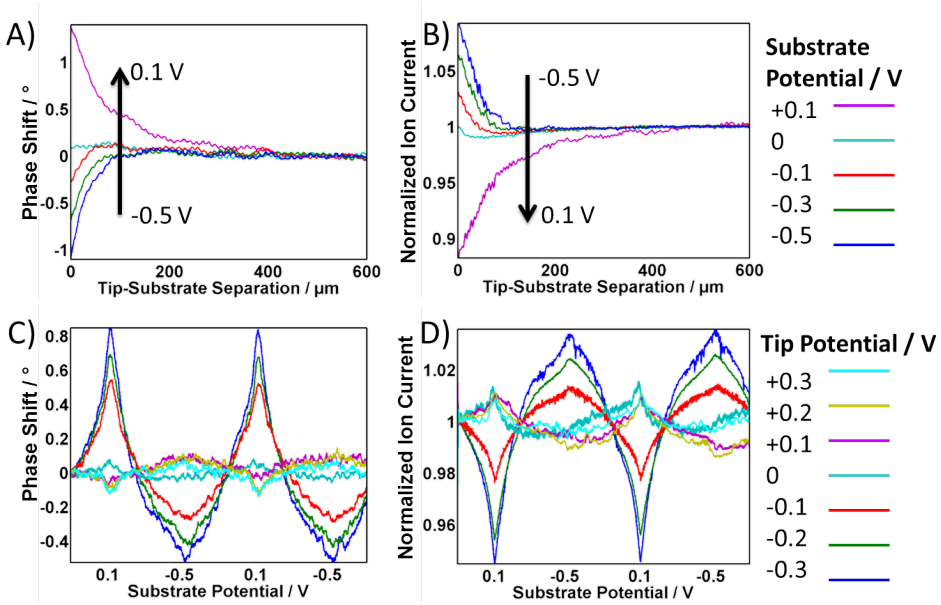

Figure 7.3: Approach curves of (A) subtracted phase and (B) normalized ion current to a fixed-potential Hg-covered Pt UME. All were recorded with a bias between the probe and the reference electrodes (V_{ref}) of -0.4 V while the potential applied to the UME (V_{UME}) was varied. CVs show the change in (C) Phase and (D) ion current collected at the nanopipette while the potential is swept at the UME. Each line represents a different bias between the nanopipette and the reference electrode (V_{ref}), with the negative biases showing higher sensitivity to changes in surface charge.

charge around the PZC. The results of those approaches in both the AC phase (Figure 7.3(A)) and ion current (Figure 7.3(B)) show a gradual change in the response as an increasingly positive bias is applied to the substrate during the approach. These results are consistent with previous work; when the probe is biased negative and the UME is biased negative, current enhancement is observed. This was explained by McKelvey *et al*[270] by the theory of perm-selectivity at the end of the pipette. The approaches suggest that the PZC is thus somewhere between 0 V and +0.1 V (as this is where the AC phase/DC responses switch polarity), in close agreement with the impedance data given that the response from the probe will be offset due the dependence of the current on ICR in the probe as well as SIR.

Figure 7.3(C and D) show the AC phase and DC response during a series of 'approach then surface CV' experiments. The bias between the probe and

the reference electrode is held at values ranging from -0.3 V to 0.3 V (in 0.1 V intervals) before approaching the Hg and then running a CV at the substrate while the probe is at the point of closest approach. These data show that it is possible to track the surface charge in real time as well as showing that some probe biases are more suitable than others for detecting the changes. At negative probe biases the technique is more sensitive than at positive biases, evinced by the fact that the effect is far greater at even the lowest negative probe bias (-0.1 V, red) than it is at the highest positive probe bias (+0.3 V, light blue). As well as the polarity of the bias, the magnitude also affects the signal. The peaks in the voltammogram is twice as pronounced at a probe bias of -0.3 V (dark blue) as it is at -0.1 V (red). It is timely now to discuss the limits of the resolution of this technique, and to quantify the magnitudes of the surface charges detected. If we assume the PZC of the Hg in 10 mM KNO_3 to be -100 mV, we can use the following equation, derived from the Poisson-Boltzmann equation[125] to determine the surface charge density, σ^M:

$$\sigma^M = (8\mathscr{K}T\varepsilon\varepsilon_0 n^0)^{1/2} \sinh\left(\frac{ze\phi_0}{2\mathscr{K}T}\right) \tag{7.1}$$

which, for dilute aqueous solutions of 1:1 electrolyte at 25 °C, can be written as:

$$\sigma^M = 11.7(C_b)^{1/2} \sinh(19.5\phi_0) \tag{7.2}$$

where σ^M is the surface charge density in $\mu C\,cm^{-2}$, C_b is the bulk electrolyte concentration in $mol\,dm^{-3}$ and ϕ_0 is the offset from the PZC in V. For example, when applying a potential of +0.1 V to the Hg (+0.2 V above the PZC), the surface charge density can be estimated at 0.29 $C\,m^{-2}$, this is in close agreement with previously reported values.[164] This suggests that a wide range of surface charge values should be detectable with this technique. After conducting more approaches to fixed potentials (not included here), the detection limit of this technique in its present form is around 50 mV either side of the PZC, or a surface charge of around 0.01 $C\,m^{-2}$. However, with smaller nanopipettes, and thus lower probe-substrate separation that detection limit may yet be improved substantially.

7.3.2 Dynamic Surface Charge Mapping

This technique can also be used to give spatial resolution of surface charge, and distinguish between surfaces of differing surface charge density. The 'approach then surface CV' regime described above was used at every pixel in a hopping mode scan to produce Figure 7.4.

The Hg droplet occupies the left hand side of each image, as seen in the accompanying topography scan that was recorded simultaneously (Figure 7.4(E)). The Hg droplet can easily be distinguished from the glass surrounding it at the extreme potentials of -0.5 V and +0.1 V, but in the middle of the CV the UME and the glass become indistinguishable allowing us to postulate that the surface charge of the Hg at that point is somewhat similar to the surface charge of the glass.

The hopping 'approach then surface CV' program was also used to image more complex substrates than the idealized Hg droplet electrode. A 25 µm Pt UME was functionalized with 1-dodecanethiol to form a methyl-terminated self-assembled monolayer (SAM), giving a uniform surface, avoiding any issues that may arise from either the polycrystalline makeup or the fouling of Pt. Attempts to perform impedance spectroscopy on this substrate met with the usual difficulties of the technique *vide infra*, and yet the functionalized Pt was scanned (Figure 7.5) with a similar level of success to that of the Hg droplet. This suggests that this technique is robust enough to deal with non-ideal, real-world substrates in addition to those already studied.

7.4 Conclusion

The three electrode setup described in this work has shown it is possible to measure surface charge of an electrode independently of the current at that electrode. This allows for the dynamic mapping of the charge on the surface as it is changing during a CV. The ability to resolve variations in surface charge on a conducting surface in real time has many applications; notably in the realm of nanoscale systems such as batteries and electrical double-layer capacitors

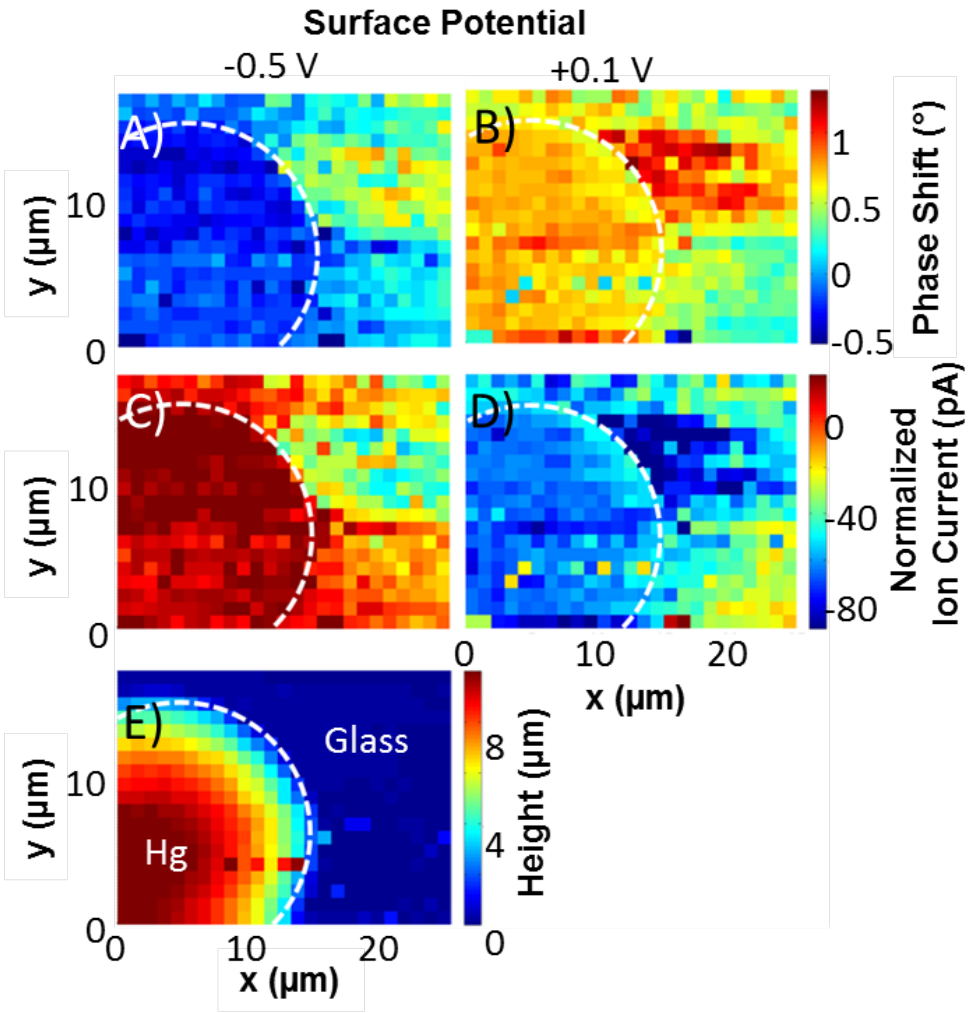

Figure 7.4: Four frames from a video showing a CV applied to a Hg electrode, as detected by a nanopipette at ∼50 nm probe-substrate separation. (A) and (B) shows the subtracted AC phase and opposite ends of the surface CV (-0.5 V and +0.1 V) while (C) and (D) show the subtracted DC ion current. Each pixel was collected in the 'approach then surface CV' regime. (E) The topography of the substrate, recorded simultaneously, for reference.

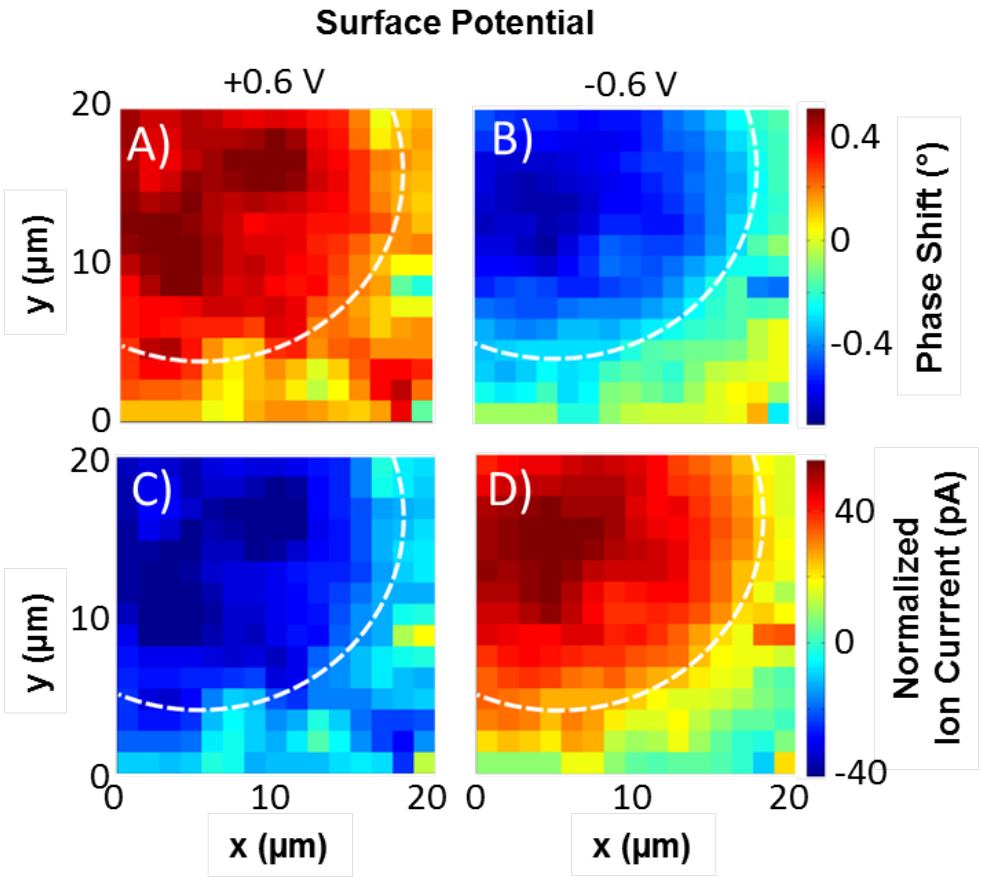

Figure 7.5: Four frames from a video showing a CV applied to a SAM-coated Pt electrode, as detected by a nanopipette at ∼50 nm probe-substrate separation. The white dotted line denotes the approximate boundary between the glass and the UME. (A) and (B) show the subtracted AC phase and opposite ends of the surface CV (-0.6 V and +0.6 V) while (C) and (D) show the subtracted DC ion current. Each pixel was collected in the 'approach then surface CV' regime.

where the size and makeup of the DDL can enhance or hinder functionality. In addition, this technique could also be used to study heterogeneities of polycrystalline macroscopic electrode surfaces A complete understanding of how these systems change with a changing applied voltage could inform more informed design in the future. In combination with finite element modelling, this technique could be used to build a more quantitative understanding of surface charge density at an interface. This technique could then be used for extracting local electrical properties (*e.g* PZC) of systems such as those described in this work with comparable accuracy to current values from impedance. However, the most diverse applications of this area of study are in a biological setting. This work takes the first step towards such use by proving that the technique is applicable to organic surfaces, in this case the SAM molecules. There are myriad systems in which surface charge can be used to indicate the phenotype of a given protein or cell. Further work will focus in this area, combining the method described herein with other electrochemical techniques to simultaneously probe many physicochemical properties of living cells.

7.5 Acknowledgements

We extend our thanks to European Research Council (ERC-2009-AdG247143-QUANTIF) for funding for SLK and the EPSRC (through the MOAC DTC) for funding for AP. We are grateful to Alex W. Colburn (University of Warwick) for custom built electronics.

Chapter 8

Conclusion and Future Perspective

> "We're happy, free, confused, and lonely at the same time, it's miserable and magical. Oh, yeah. Tonight's the night when we forget about the deadlines. It's time"
>
> Taylor Swift

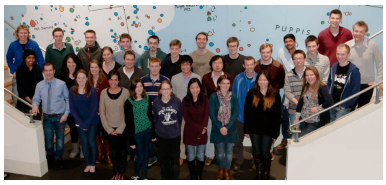

Scanning probe microscopy (SPM) has continually evolved since its creation and now encompasses a large range of techniques and within each of those techniques are a variety of modes and probes for different specific experiments. This thesis has continued to expand and improve the capabilities of SPM. Firstly, a brand new SPM platform, the hardware of which is described in Chapter 2, allows for a multitude of probes to be used interchangeably on the same instrument. The advantages enjoyed by such a platform have been numerous. The hardware that controls the experiments, the FPGA card, can be reprogrammed so is will not be necessary to replace the card for many years, during this time new functionality can be continually added. Due to

the size and scope of the platform a multitude of different SPM techniques can be performed on the same rig, eliminating the need to purchase separate equipment. With the ability to change the software, new hardware can be added and supported when necessary, examples have been the addition of the Picomotors and the auto-scaling current followers. The major advantage of the platform is the waypoint system for experiment design. The software and the implementation of this waypoint system is described in Chapter 3. With the level of freedom to create new waypoint patterns that the platform has, new techniques can go from conception to execution in days. At time of writing there are over 60 different 'User VI's that create different waypoint patterns, each with several options for various types of probe. The electrical noise and thermal shielding allows currents in the femto amp range to be recorded and a piezo drift of $<10\ \mathrm{nm\,min^{-1}}$. This thermal stability also works to remove any affect of convection in an experiment with a bath of solution.

In Chapter 4, the advantages of the dual-barrel conductance micropipette also known as scanning electrochemical cell microscopy (SECCM) are discussed with their relevance to ionic crystal dissolution. A significant advantage is that the sample is kept in air until the point the meniscus of the probe lands on the surface. This not only provides an obvious and well-defined starting point for the dissolution but also maintains the sample's pristine surface. Therefore the probe can land at a large number of sites on a single sample with a high degree of reproducibility as the sample has been completely unaffected by the previous landings. All other current techniques require the sample to be submerged and therefore the surface is in a state of flux before the measurement has begun.

Due to the speed of the FPGA card, the temporal resolution is extremely high. Data can be collected at 55.5 kHz, however the dissolution of NaCl takes place over milliseconds so a data collection rate of 25.2 kHz was sufficient, this also had the advantage of having time to perform averaging on the incoming signal and therefore less noise. It is shown that kinetic information can be elucidated for NaCl (111) crystals.

The SECCM system has been modelled with a high level of accuracy using finite element method (FEM) modelling and the parameters of the ex-

periment can be fit to the simulation to determine a rate constant. We can now report a dissolution rate constant of $(7.5 \pm 2.5) \times 10^{-5}$ cm s^{-1} with the largest source of error being the width of the meniscus after spreading onto the surface.

The scope of dual-barrel conductance micropipette experiments can be widened when the technique is used in conjunction with another SPM. Both SECCM and AFM are used in Chapter 5 to investigate the dissolution kinetics of calcite. In the process of recording ion current during dissolution with SECCM etch pits are created. Both the ion current traces and etch pit morphology are a function of dissolution rate and therefore the rate can be extracted by coupling these data with a FEM model and AFM respectively. In the case of calcite, a dissolution rate constant of 0.14 ± 0.07 cm s^{-1} was extracted from the FEM model in combination with the AFM data.

Since developing this technique for crystal dissolution it has already been applied to enamel.[275] Different protective treatments can be tested on a single enamel surface, eliminating the error arising from natural variation from sample to sample. Looking forward, it will not only be possible to screen a range of surface treatments but also different solutions additives to either promote or retard dissolution of a crystal sample. The only drawback being different probes would have to be used for each solution. However, with laser puller technologies at their current level it is already possible to fabricate highly reproducible probes.

The unique ability to perform experiments in air, only exposing the crystal to solution on the microscale, has allowed for the investigation of dissolution of separate steps on calcite. The $[48\bar{1}]_+$ and $[\bar{4}41]_+$ (positive) planes dissolved to produce wide shallow trenches, while the $[48\bar{1}]_-$ and $[\bar{4}41]_-$ (negative) planes gave narrow, thin trenches. This was explained by the difference in angle between the basal plane and the dissolving terrace on the positive and negative planes. The positive planes have an obtuse angle and the negative planes an acute angle, these dissolve at different rates. The author expects that future studies will take advantage of the speed and ease with which to make these dynamic measurements, and dissolution of individual steps will be studied on a wide range of crystals.

The ability of SECCM to pattern crystals has also been demonstrated, text 12 µm tall was etched into the calcite. The ability to make precise patterns onto a crystal surface presents the possibility to direct and control crystal growth. This technique can be used, not to dissolve a surface, but to pattern a material on top of a surface. This work has been touched on in a report outlining how to make wires of conductive polymer.[97] Further development could see this technique employed to make nanosized wires or channels for circuit boards and 'Lab-on-chip' technologies.

The same scanning probe microscope rigs, developed for SECCM, have been used for scanning ion conductance microscopy (SICM). In Chapter 6 a brand new use for SICM is presented in which a low concentration of electrolyte is used so that ion current rectification can be observed in the probe. The low concentration creates a diffuse double layer (DDL) that extends far enough into the solution that it can be detected by the probe. As the properties of the DDL are directly proportional to the surface charge of the substrate it is possible to calculate a value for surface charge on any sample, be they conductive or non-conductive. The theory behind this is that an ion perm-selective region is created at the end of the probe due to the charge on the glass probe and on the surface. The charge on the glass probe, although can change slightly over time, can be assumed to be a constant offset. The charge on the surface then can vary which changes the perm-selective region and therefore the current that can flow. Although the results were not quantitative, it was shown that the technique can qualitatively differentiate non-conductive samples that were positively, negatively or neutrally charged. This work has been continued to use bias modulation SICM to accurately measure topography and surface charge simultaneously.[271]

So far only ideal surfaces have been used in order to fully test the methodology. We have reached a point where novel non-conductive samples can be used, of great interest will be the study of biological system, this would fully taken advantaged of the technique as SICM allows for living cells to be studied in a bio-compatible environment. The surface charge of cells will have a large influence on how they react with each other and with drug molecules. Understanding the surface local charge over an entire cell will be important in

the design and study of new drugs. Other biological uses of this technology would be to skin cells, and large section of skins. Knowing the surface charge of skin would help design a number of different products from treatments for skin conditions and transdermal drug delivery to touch technologies and skin care creams and cosmetics. Similarly, the study of hair would help inform on the design of new hair care and shampoo products. Potential non-biological samples include nanopore sensors. These sensors are often constructed from glass, silicon nitride and more recently diamond. They reply on particles passing through the pore and surface charge of both the particle and the pore will play a role in this process.

Chapter 7 extend the capabilities of this new SICM based technique and applies it to a conductive substrate. In this case the substrate surface charge can be changed *in-situ* and in real time. SICM can dynamically observe these changes and can produce 3D functional maps of the information. The charge resolution was shown to be $\sim$0.01 $\mathrm{C\,m^{-2}}$. A test system of a Hg hemisphere on a Pt ultramicroelectrode (UME) is studied but another sample, self assembled monolayer molecules on the same Pt UME mimicking a biological sample is also studies as a proof of concept. A range of biological processes could be studied with this technique, The potential of this technique to improve electrode and battery technology is high. Fully understanding surface charge in these systems will allow us to synthesize new materials with the exact requirements for energy storage and transfer.

Bibliography

[1] N. J Gray and P. R Unwin. *Analyst*, 125(5):889–893, 2000.

[2] C. G Williams, M. A Edwards, A. L Colley, J. V Macpherson, and P. R Unwin. *Anal. Chem.*, 81(7):2486–2495, April 2009.

[3] M. D Rubianes and G. A Rivas. *Electrochem. commun.*, 5(8):689–694, August 2003.

[4] C. O Laoire, S Mukerjee, K. M Abraham, E. J Plichta, and M. A Hendrickson. *J. Phys. Chem. C*, 114(19):9178–9186, May 2010.

[5] M. D Levi and D Aurbach. *J. Phys. Chem. B*, 101(23):4630–4640, June 1997.

[6] J. E Zuliani, J. N Caguiat, D. W Kirk, and C. Q Jia. *J. Power Sources*, 290:136–143, September 2015.

[7] H. S White and A Bund. *Langmuir*, 24(5):2212–2218, March 2008.

[8] C.-H Chen, K. E Meadows, A Cuharuc, S. C. S Lai, and P. R Unwin. *Phys. Chem. Chem. Phys.*, 16(34):18545–52, September 2014.

[9] A. A Gewirth and B. K Niece. *Chem. Rev.*, 97(4):1129–1162, June 1997.

[10] G Binnig, H Rohrer, C Gerber, and E Weibel. *Phys. Rev. Lett.*, 49(1):57–61, July 1982.

[11] G. K Binnig. *Phys. Scr.*, T19A:53–54, January 1987.

[12] Q Zhong, D Inniss, K Kjoller, and V Elings. *Surf. Sci.*, 290(1-2):L688–L692, June 1993.

[13] H.-J Butt, B Cappella, and M Kappl. *Surf. Sci. Rep.*, 59(1-6):1–152, October 2005.

[14] B Bhushan and V. N Koinkar. *Appl. Phys. Lett.*, 64(13):1653, March 1994.

[15] S. N Magonov and D. H Reneker. *Annu. Rev. Mater. Sci.*, 27(1):175–222, August 1997.

[16] A. L Weisenhorn, P Maivald, H.-J Butt, and P. K Hansma. *Phys. Rev. B*, 45(19):11226–11232, May 1992.

[17] H Lee, N. F Scherer, and P. B Messersmith. *Proc. Natl. Acad. Sci. U. S. A.*, 103(35):12999–3003, August 2006.

[18] R Erlandsson, G Hadziioannou, C. M Mate, G. M McClelland, and S Chiang. *J. Chem. Phys.*, 89(8):5190, October 1988.

[19] R. E Mahaffy, S Park, E Gerde, J Käs, and C. K Shih. *Biophys. J.*, 86(3):1777–93, March 2004.

[20] D. J Müller and Y. F Dufrêne. *Nat. Nanotechnol.*, 3(5):261–269, May 2008.

[21] M Basletic, J.-L Maurice, C Carrétéro, G Herranz, O Copie, M Bibes, E Jacquet, K Bouzehouane, S Fusil, and A Barthélémy. *Nat. Mater.*, 7(8):621–5, August 2008.

[22] G Leatherman, E. N Durantini, D Gust, T. A Moore, A. L Moore, S Stone, Z Zhou, P Rez, Y. Z Liu, and S. M Lindsay. *J. Phys. Chem. B*, 103(20):4006–4010, May 1999.

[23] A. J Bard, F.-r. R. F Fan, J Kwak, and O Lev. *Anal. Chem.*, 61(24):132–138, January 1989.

[24] L Niu, Y Yin, W Guo, M Lu, R Qin, and S Chen. *J. Mater. Sci.*, 44(17):4511–4521, June 2009.

[25] P Sun, Z Zhang, J Guo, and Y Shao. *Anal. Chem.*, 73(21):5346–5351, November 2001.

[26] W Zhan and A. J Bard. *Anal. Chem.*, 78(3):726–733, February 2006.

[27] B. B Katemann and W Schuhmann. *Electroanal.*, 14(1):22–28, January 2002.

[28] C Cannes, F Kanoufi, and A. J Bard. *J. Electroanal. Chem.*, 547(1):83–91, April 2003.

[29] C. J Slevin, S Ryley, D. J Walton, and P. R Unwin. *Langmuir*, 14(19):5331–5334, September 1998.

[30] P Sun and M. V Mirkin. *Anal. Chem.*, 78(18):6526–6534, September 2006.

[31] Y Takahashi, A. I Shevchuk, P Novak, B Babakinejad, J Macpherson, P. R Unwin, H Shiku, J Gorelik, D Klenerman, Y. E Korchev, and T Matsue. *Proc. Natl. Acad. Sci.*, 109(29):11540–11545, 2012.

[32] P Sun and M. V Mirkin. *Anal. Chem.*, 79(15):5809–5816, 2007.

[33] A Kucernak, P Chowdhury, C Wilde, G Kelsall, Y Zhu, and D Williams. *Electrochim. Acta*, 45(27):4483–4491, September 2000.

[34] A. K Neufeld, A. P O'Mullane, and A. M Bond. *J. Am. Chem. Soc.*, 127(40):13846–53, October 2005.

[35] S Nugues and G Denuault. *J. Electroanal. Chem.*, 408(1-2):125–140, May 1996.

[36] C. G Zoski, N Yang, P He, L Berdondini, and M Koudelka-Hep. *Anal. Chem.*, 79(4):1474–84, February 2007.

[37] S Amemiya, A. J Bard, F.-R. F Fan, M. V Mirkin, and P. R Unwin. *Ann. Rev. Anal. Chem.*, 1:95–131, 2008.

[38] J. L Fernández and A. J Bard. *Anal. Chem.*, 76(8):2281–9, April 2004.

[39] G Lu, J. S Cooper, and P. J McGinn. *Electrochim. Acta*, 52(16):5172–5181, April 2007.

[40] D. A Walsh, J. L Fernandez, and A. J Bard. *J. Electrochem. Soc.*, 153(6):E99, 2006.

[41] C. G Zoski. *J. Phys. Chem. B*, 107(26):6401–6405, July 2003.

[42] R. D Martin and P. R Unwin. *Anal. Chem.*, 70(2):276–284, January 1998.

[43] C. M Sánchez-Sánchez, J Rodríguez-López, and A. J Bard. *Anal. Chem.*, 80(9):3254–60, May 2008.

[44] P. I James. *J. Electrochem. Soc.*, 145(4):L64, April 1998.

[45] M Etienne, A Schulte, S Mann, G Jordan, L. D Dietzel, and W Schuhmann. *Anal. Chem.*, 76(13):3682–3688, 2004.

[46] B. R Horrocks, M. V Mirkin, D. T Pierce, and A. J Bard. *Anal. Chem.*, 65(9):1213–1224, May 1993.

[47] K Eckhard and W Schuhmann. *Analyst*, 133(11):1486, November 2008.

[48] K Eckhard, T Erichsen, M Stratmann, and W Schuhmann. *Chem. Eur. J.*, 14(13):3968–3976, April 2008.

[49] P. M Diakowski and Z Ding. *Phys. Chem. Chem. Phys.*, 9(45):5966–5974, December 2007.

[50] S Bergner, J Wegener, and F.-M Matysik. *Anal. Chem.*, 83(1):169–174, January 2011.

[51] J. V Macpherson, P. R Unwin, A. C Hillier, and A. J Bard. *J. Am. Chem. Soc.*, 118(27):6445–6452, 1996.

[52] J. V Macpherson and P. R Unwin. *Anal. Chem.*, 73(3):550–557, February 2001.

[53] J. V Macpherson and P. R Unwin. *Anal. Chem.*, 72(2):276–285, 2000.

[54] A Eifert, B Mizaikoff, and C Kranz. *Micron*, 68:27–35, January 2015.

[55] H Shin, P Hesketh, B Mizaikoff, and C Kranz. *Sensors Actuators B Chem.*, 134(2):488–495, September 2008.

[56] M. A Derylo, K. C Morton, and L. A Baker. *Langmuir*, 27(22):13925–30, November 2011.

[57] A. A Bertagnolli, A Lugstein, M Wu, B Gollas, I Pobelov, T Wandlowski, K Leonhardt, and G Denuault. *Nanotechnology*, 22(14):145306, 2011.

[58] A Davoodi, J Pan, C Leygraf, and S Norgren. *Electrochem. Solid-State Lett.*, 8(6):B21, June 2005.

[59] W Smirnov, A Kriele, R Hoffmann, E Sillero, J Hees, O. A Williams, N Yang, C Kranz, and C. E Nebel. *Anal. Chem.*, 83(12):4936–41, June 2011.

[60] A Eifert, W Smirnov, S Frittmann, C Nebel, B Mizaikoff, and C Kranz. *Electrochem. commun.*, 25:30–34, November 2012.

[61] A Davoodi, J Pan, C Leygraf, and S Norgren. *J. Electrochem. Soc.*, 155(4):C138, April 2008.

[62] A Kueng, C Kranz, A Lugstein, E Bertagnolli, and B Mizaikoff. *Angew. Chem. Int. Ed.*, 42(28):3238–3240, July 2003.

[63] Y Matsumae, Y Takahashi, K Ino, H Shiku, and T Matsue. *Anal. Chim. Acta*, 842:20–6, September 2014.

[64] P. K Hansma, B Drake, O Marti, S. A. C Gould, and C. B Prater. *Science (80-.).*, 243(4891):641–643, 1989.

[65] Y Zhou, C.-C Chen, and L. A Baker. *Anal. Chem.*, 84(6):3003–9, March 2012.

[66] C.-C Chen, Y Zhou, and L. A Baker. *ACS Nano*, 5(10):8404–8411, October 2011.

[67] C.-C Chen, Y Zhou, and L. A Baker. *Annu. Rev. Anal. Chem.*, 5(1):207–228, 2012.

[68] A Schulte, M Nebel, and W Schuhmann. *Ann. Rev. Anal. Chem.*, 3:299–318, January 2010.

[69] S Bergner, P Vatsyayan, and F.-m Matysik. *Anal. Chim. Acta*, 775:1–13, May 2013.

[70] Y. E Korchev, M Milovanovic, C. L Bashford, D. C Bennett, E. V Sviderskaya, I Vodyanoy, and M. J Lab. *J. Microsc.*, 188(1):17–23, 1997.

[71] A. I Shevchuk, G. I Frolenkov, D Sánchez, P. S James, N Freedman, M. J Lab, R Jones, D Klenerman, and Y. E Korchev. *Angew. Chem. Int. Ed.*, 45(14):2212–2216, March 2006.

[72] Y. E Korchev, J Gorelik, M. J Lab, E. V Sviderskaya, C. L Johnston, C. R Coombes, I Vodyanoy, and C. R Edwards. *Biophys. J.*, 78(1):451–7, January 2000.

[73] S. C Walker, S Allen, G Bell, and C. J Roberts. *J. Microsc.*, 258(2):119–26, May 2015.

[74] J Seifert, J Rheinlaender, P Novak, Y. E Korchev, and T. E Schäffer. *Langmuir*, 31(24):6807–6813, June 2015.

[75] Y. E Korchev, Y. A Negulyaev, C. R Edwards, I Vodyanoy, and M. J Lab. *Nat. Cell Biol.*, 2(9):616–9, September 2000.

[76] A. I Shevchuk, J Gorelik, S. E Harding, M. J Lab, D Klenerman, and Y. E Korchev. *Biophys. J.*, 81(3):1759–1764, September 2001.

[77] D. J Comstock, J. W Elam, M. J Pellin, and M. C Hersam. *Anal. Chem.*, 82(4):1270–1276, February 2010.

[78] A. J Pollard, N Faruqui, M Shaw, C. A Clifford, Y Takahashi, Y. E Korchev, N Ebejer, J. V Macpherson, P. R Unwin, and D Roy. *MRS Proc.*, 1422(1422):mrsf11—-1422—-qq07—-04, March 2012.

[79] M. A O'Connell and A. J Wain. *Anal. Chem.*, 86(24):12100–7, December 2014.

[80] B. P Nadappuram, K McKelvey, J. C Byers, A. G Güell, A. W Colburn, R. A Lazenby, and P. R Unwin. *Anal. Chem.*, 87(7):3566–73, April 2015.

[81] Y Takahashi, T Miyamoto, H Shiku, K Ino, T Yasukawa, R Asano, I Kumagai, and T Matsue. *Phys. Chem. Chem. Phys.*, 13(37):16569–16573, October 2011.

[82] C. A Morris, C.-C Chen, and L. A Baker. *Analyst*, 137(13):2933–2938, 2012.

[83] M Sen, Y Takahashi, Y Matsumae, Y Horiguchi, A Kumatani, K Ino, H Shiku, and T Matsue. *Anal. Chem.*, 87(6):3484–3489, February 2015.

[84] B. P Nadappuram, K McKelvey, R Al Botros, A. W Colburn, and P. R Unwin. *Anal. Chem.*, 2013.

[85] N Ebejer, M Schnippering, A. W Colburn, M. A Edwards, and P. R Unwin. *Anal. Chem.*, 82(22):9141–9145, 2010.

[86] B. D. B Aaronson, S. C. S Lai, and P. R Unwin. *Langmuir*, 30(7):1915–9, February 2014.

[87] K. T Rodolfa, A Bruckbauer, D Zhou, Y. E Korchev, and D Klenerman. *Angew. Chemie Int. Ed.*, 44(42):6854–6859, 2005.

[88] S. L Kinnear, K McKelvey, M. E Snowden, M Peruffo, A. W Colburn, and P. R Unwin. *Langmuir*, 29(50):15565–15572, 2013.

[89] T. S Miller, N Ebejer, A. G Güell, J. V Macpherson, and P. R Unwin. *Chem. Comm.*, 48(60):7435–7437, August 2012.

[90] M. E Snowden, A. G Gueell, S. C. S Lai, K McKelvey, N Ebejer, M. A O'Connell, A. W Colburn, and P. R Unwin. *Anal. Chem.*, 84(5):2483–2491, 2012.

[91] A. G Güell, N Ebejer, M. E Snowden, J. V Macpherson, and P. R Unwin. *J. Am. Chem. Soc.*, 134(17):7258–7261, May 2012.

[92] A. N Patel, M. G Collignon, M. A O'Connell, W. O. Y Hung, K McKelvey, J. V Macpherson, and P. R Unwin. *J. Am. Chem. Soc.*, 134(49):20117–20130, December 2012.

[93] S. C. S Lai, A. N Patel, K McKelvey, and P. R Unwin. *Angew. Chemie Int. Ed.*, 51(22):5260, 2012.

[94] A. G Güell, A. S Cuharuc, Y.-R Kim, G Zhang, S.-y Tan, N Ebejer, and P. R Unwin. *ACS Nano*, 9(4):3558–71, April 2015.

[95] A. G Güell, N Ebejer, M. E Snowden, K McKelvey, J. V Macpherson, and P. R Unwin. *Proc. Natl. Acad. Sci.*, 109:11487–11492, May 2012.

[96] S. C. S Lai, P. V Dudin, J. V Macpherson, and P. R Unwin. *J. Am. Chem. Soc.*, 133(28):10744–10747, 2011.

[97] K McKelvey, M. A O'Connell, and P. R Unwin. *Chem. Commun.*, 49(29):2986–2988, 2013.

[98] K McKelvey, D Perry, J. C Byers, A. W Colburn, and P. R Unwin. *Anal. Chem.*, 86(7):3639–3646, April 2014.

[99] C.-H Chen, L Jacobse, K McKelvey, S. C. S Lai, M. T. M Koper, and P. R Unwin. *Anal. Chem.*, 87(11):5782–9, June 2015.

[100] M. R Langer. *J. Eukaryot. Microbiol.*, 55(3):163–169, 2008.

[101] S.-S Wang and A.-W Xu. *Cryst. Growth Des.*, 13(5):1937–1942, 2013.

[102] A Danesh, S. D Connell, M. C Davies, C. J Roberts, S. J. B Tendler, P. M Williams, and M. J Wilkins. *Pharm. Res.*, 18(3):299–303, 2001.

[103] H Wen, T Li, K. R Morris, and K Park. *J. Phys. Chem. B*, 108(30):11219–11227, 2004.

[104] A. A. C Bode, S Jiang, J. A. M Meijer, W. J. P van Enckevort, and E Vlieg. *Cryst. Growth Des.*, 12(12):5889–5896, 2012.

[105] E Charola, J Pühringer, and M Steiger. *Environ. Geol.*, 52(2):339–352, 2006.

[106] M Dejmek and C. A Ward. *J. Chem. Phys.*, 108(20):8698–8704, 1998.

[107] A. J Bard and Larry R. Faulkner. *Electrochemical Methods*. John Wiley & Sons, 2001.

[108] A. C Fisher. *Electrode Dynamics*. Oxford University Press, 2009.

[109] P Atkins and J De Paula. *Physical Chemistry*. Oxford University Press, 2006.

[110] N Agmon. *Chem. Phys. Lett.*, 244(5-6):456–462, October 1995.

[111] W Hamer. *The structure of electrolytic solutions*. Wiley, New York :, 1959.

[112] P. R Unwin and J. V Macpherson. *Chem. Soc. Rev.*, 24(2):109–119, 1995.

[113] J. V Macpherson and P. R Unwin. *J. Phys. Chem.*, 98(6):1704–1713, 1994.

[114] I. N MacInnis and S. L Brantley. *Geochim. Cosmochim. Acta*, 56:1113–1126, 1992.

[115] B Henderson. *Defects in crystalline solids*. Edward Arnold, London, 1972.

[116] D Hull. *Introduction to dislocations*. Butterworth Heinemann, Oxford, 2001.

[117] A Malkin, Y Kuznetsov, and A McPherson. *J. Cryst. Growth*, 196(2-4):471–488, January 1999.

[118] A. C Lasaga and A Luttge. *Science*, 291(5512):2400–4, March 2001.

[119] B Simon. *J. Cryst. Growth*, 52(2):789–794, 1981.

[120] R Orton and P. R Unwin. *J. Chem. Soc. Faraday Trans.*, 89(21):3947–3954, 1993.

[121] Y Liang and D Baer. *Surf. Sci.*, 373(2-3):275–287, March 1997.

[122] P. M Dove and F. M Platt. *Chem. Geol.*, 127(4):331–338, 1996.

[123] W. H Casey, M. J Carr, and R. A Graham. *Geochim. Cosmochim. Acta*, 52(6):1545–1556, 1988.

[124] H. V Alexandru. *J. Cryst. Growth*, 10(2):151–157, 1971.

[125] A. J Bard and L. R Faulkner. *Electrochemical Methods: Fundamentals and Applications*. Wiley, New York, 1980.

[126] B Hendriksen and J Williams. *Int. J. Pharm.*, 69(2):175–180, March 1991.

[127] O. S Pokrovsky, S. V Golubev, and G Jordan. *Chem. Geol.*, 265(12):33–43, 2009.

[128] M Alkattan, E. H Oelkers, J.-L Dandurand, and J Schott. *Chem. Geol.*, 151(14):199–214, 1998.

[129] C Peng, J. P Crawshaw, G. C Maitland, and J. M Trusler. *Chem. Geol.*, 403:74–85, May 2015.

[130] K Burns, Y.-T Wu, and C. S Grant. *Langmuir*, 19(14):5669–5679, 2003.

[131] S Lee, S. G Lee, M Sim, D Kwak, J. H Park, and K Cho. *Cryst. Growth Des.*, 11(11):4920–4926, 2011.

[132] E. L Sjoeberg and D. T Rickard. *Chem. Geol.*, 42:119–136, 1984.

[133] H. H Hassan, J Sculfort, M Etman, F Ozanam, and J.-N Chazalviel. *J. Electroanal. Chem.*, 380(1-2):55–61, January 1995.

[134] R. G Compton and G. H. W Sanders. *J. Colloid Interface Sci.*, 158(2):439–445, 1993.

[135] Q Gong, J Deng, Q Wang, L Yang, and M She. *J. Earth Sci.*, 21(4):402–411, 2010.

[136] P Lehto, J Aaltonen, P Niemelä, J Rantanen, J Hirvonen, V. P Tanninen, and L Peltonen. *Int. J. Pharm.*, 363(12):66–72, 2008.

[137] Y Sugawara, T Okayasu, A. P Yadav, A Nishikata, and T Tsuru. *J. Electrochem. Soc.*, 159(11):F779–F786, September 2012.

[138] R. G Compton and C. A Brown. *J. Colloid Interface Sci.*, 170(2):586–590, 1995.

[139] E Kaunisto, M Marucci, and A Axelsson. *AIChE J.*, 57(10):2610–2617, 2011.

[140] R. D Fisher, M. M Mbogoro, M. E Snowden, M. B Joseph, J. A Covington, P. R Unwin, and R. I Walton. *ACS Appl. Mater. Interfaces*, 3(9):3528–3537, 2011.

[141] J. J De Yoreo, L. A Zepeda-Ruiz, R. W Friddle, S. R Qiu, L. E Wasylenki, A. A Chernov, G. H Gilmer, and P. M Dove. *Cryst. Growth Des.*, 9:5135–5144, 2009.

[142] S Wu, X Lan, F Huang, Z Luo, H Ju, C Meng, and C Duan. *Biosens. Bioelectron.*, 32(1):293–296, 2012.

[143] C.-A McGeouch, M. A Edwards, M. M Mbogoro, C Parkinson, and P. R Unwin. *Anal. Chem.*, 82(22):9322–9328, 2010.

[144] D Bosbach and W Rammensee. *Geochim. Cosmochim. Acta*, 58(2):843–849, 1994.

[145] J. W Morse and R. S Arvidson. *Earth-Science Rev.*, 58(12):51–84, 2002.

[146] H. H Teng. *Spectroscopy*, 20(6):16, 2005.

[147] M Urosevic, C Rodriguez-Navarro, C. V Putnis, C Cardell, A Putnis, and E Ruiz-Agudo. *Geochim. Cosmochim. Acta*, 80:1–13, 2012.

[148] E. H Oelkers, S. V Golubev, O. S Pokrovsky, and P Bénézeth. *Geochim. Cosmochim. Acta*, 75(7):1799–1813, 2011.

[149] D.-Y Fan, A. B Hope, P. J Smith, H Jia, R. J Pace, J. M Anderson, and W. S Chow. *Biochim. Biophys. Acta*, 1767(8):1064–1072, August 2007.

[150] S Guo, M. D Ward, and J. A Wesson. *Langmuir*, 18(11):4284–4291, 2002.

[151] D. P Burt, N. R Wilson, U Janus, J. V Macpherson, and P. R Unwin. *Langmuir*, 24(22):12867–12876, 2008.

[152] N.-S Park, M.-W Kim, S. C Langford, and J. T Dickinson. *Langmuir*, 12(19):4599–4604, 1996.

[153] N.-S Park, M.-W Kim, S. C Langford, and J. T Dickinson. *J. Appl. Phys.*, 80(5):2680–2686, 1996.

[154] R Shiraki, P. A Rock, and W. H Casey. *Aquat. Geochemistry*, 6(1):87–108, 2000.

[155] C.-A McGeouch, M Peruffo, M. A Edwards, L. A Bindley, R. A Lazenby, M. M Mbogoro, K McKelvey, and P. R Unwin. *J. Phys. Chem. C*, 116(28):14892–14899, 2012.

[156] J. W Still and D. O Wipf. *J. Electrochem. Soc.*, 144(8):2657–2665, 1997.

[157] K Fushimi, K Azumi, and M Seo. *J. Electrochem. Soc.*, 147(2):552, February 2000.

[158] K Fushimi and M Seo. *J. Electrochem. Soc.*, 148(11):B450, November 2001.

[159] C Gabrielli, S Joiret, M Keddam, H Perrot, N Portail, P Rousseau, and V Vivier. *Electrochim. Acta*, 52(27):7706–7714, 2007.

[160] H Helmholtz. *Ann. der Phys. und Chemie*, 165(6):211–233, 1853.

[161] C Brett and M Brett. *Electrochemistry Principles, Methods, and Applications*. Oxford University Press, 2005.

[162] K. B Oldham. *J. Electroanal. Chem.*, 613(2):131–138, 2008.

[163] D. C Grahame. *J. Am. Chem. Soc.*, 63(5):1207–1215, May 1941.

[164] D. C Grahame. *Chem. Rev.*, 41(3):441–501, 1947.

[165] J Bockris and M Habib. *Electrochim. Acta*, 22(1):41–46, January 1977.

[166] H Ohshima. Zeta Potential. In T Tadros, editor, *Encycl. Colloid Interface Sci.*, pages 1424–1436. Springer, Berlin, 2013.

[167] H Ohshima. *Colloid Polym. Sci.*, 285(13):1411–1421, August 2007.

[168] M Butterworth, R Corradi, J Johal, S Lascelles, S Maeda, and S Armes. *J. Colloid Interface Sci.*, 174(2):510–517, September 1995.

[169] H.-J Butt. *Biophys. J.*, 60(6):1438–1444, December 1991.

[170] W. A Ducker, T. J Senden, and R. M Pashley. *Nature*, 353(6341):239–241, September 1991.

[171] Y. E Korchev, C. L Bashford, M Milovanovic, I Vodyanoy, and M. J Lab. *Biophys. J.*, 73(2):653–658, August 1997.

[172] P Novak, C Li, A. I Shevchuk, R Stepanyan, M Caldwell, S Hughes, T. G Smart, J Gorelik, V. P Ostanin, M. J Lab, G. W. J Moss, G. I Frolenkov, D Klenerman, and Y. E Korchev. *Nat. Methods*, 6(4):279–281, April 2009.

[173] Y Nashimoto, Y Takahashi, H Ida, Y Matsumae, K Ino, H Shiku, and T Matsue. *Anal. Chem.*, 87(5):2542–5, March 2015.

[174] C Wei, A. J Bard, and S. W Feldberg. *Anal. Chem.*, 69(22):4627–4633, 1997.

[175] D Momotenko, F Cortes-Salazar, J Josserand, S Liu, Y Shao, and H. H Girault. *Phys. Chem. Chem. Phys.*, 13(12):5430–5440, 2011.

[176] R. M Wightman and D. O Wipf. Voltammetry at Ultramicroelectrodes. In A. J Bard, editor, *Electroanal. Chem.*, pages 268–353. Marcel Dekker, New York, 1988.

[177] J Macpherson. *New Approaches for the Study of Dissolution Kinetics at the Microscopic Level*. PhD thesis, University of Warwick, 1996.

[178] S Chen, Y Liu, and J Chen. *Chem. Soc. Rev.*, May 2014.

[179] K. M McKelvey. *New Approaches and Applications in Electrochemical Scanning Probe Microscopy*. Phd thesis, University of Warwick, 2012.

[180] L Zhang and A Lüttge. *Geochim. Cosmochim. Acta*, 73(10):2832–2849, 2009.

[181] S. R Vippagunta, H. G Brittain, and D. J. W Grant. *Adv. Drug Deliv. Rev.*, 48(1):3–26, 2001.

[182] A. A. C Bode, V Vonk, F. J van den Bruele, D. J Kok, A. M Kerkenaar, M. F Mantilla, S Jiang, J. A. M Meijer, W. J. P van Enckevort, and E Vlieg. *Cryst. Growth Des.*, 12(4):1919–1924, 2012.

[183] J. V Macpherson and P. R Unwin. *J. Phys. Chem.*, 99(40):14824–14831, 1995.

[184] L Peltonen, P Liljeroth, T Heikkilä, K Kontturi, and J Hirvonen. *Eur. J. Pharm. Sci.*, 19(5):395–401, 2003.

[185] M. M Mbogoro, M. E Snowden, M. A Edwards, M Peruffo, and P. R Unwin. *J. Phys. Chem. C*, 115(20):10147–10154, 2011.

[186] C Wu, K Zhao, X Wang, M Cao, H Xu, and J. R Lu. *Cryst. Growth Des.*, 12(5):2594–2601, 2012.

[187] A. O Harstad and S. L. S Stipp. *Geochim. Cosmochim. Acta*, 71(1):56–70, 2007.

[188] T Jung, X Sheng, C. K Choi, W.-S Kim, J. A Wesson, and M. D Ward. *Langmuir*, 20(20):8587–8596, 2004.

[189] D Gasperino, A Yeckel, B. K Olmsted, M. D Ward, and J. J Derby. *Langmuir*, 22(15):6578–6586, 2006.

[190] C. E Jones, P. R Unwin, and J. V Macpherson. *ChemPhysChem*, 4(2):139–146, 2003.

[191] D Zhan, D Yang, Y Zhu, X Wu, and Z.-Q Tian. *Chem. Commun.*, 48(93):11449–11451, 2012.

[192] C Laslau, D. E Williams, B Kannan, and J Travas-Sejdic. *Adv. Funct. Mater.*, 21(24):4607–4616, 2011.

[193] J Hu and M.-F Yu. *Science (80-.).*, 329(5989):313–316, 2010.

[194] J Burgess. *Metal Ions in Solution*. Halsted Press, New York, 1978.

[195] C Wagner. *J. Phys. Colloid Chem.*, 53(7):1030–1033, 1948.

[196] R. A Lipasek, J. C Ortiz, L. S Taylor, and L. J Mauer. *Food Res. Int.*, 45(1):369–380, 2012.

[197] M. B Tomson and G. H Nancollas. *Science (80-.).*, 200:1059–1060, 1978.

[198] G Taylor and H Girault. *J. Electroanal. Chem. Interfacial Electrochem.*, 208(1):179–183, August 1986.

[199] J Rheinlaender and T. E Schaeffer. *J. Appl. Phys.*, 105(9), 2009.

[200] D Sánchez, U Anand, J Gorelik, C. D Benham, C Bountra, M Lab, D Klenerman, R Birch, P Anand, and Y Korchev. *J. Neurosci. Methods*, 159(1):26–34, 2007.

[201] Y Takahashi, Y Murakami, K Nagamine, H Shiku, S Aoyagi, T Yasukawa, M Kanzaki, and T Matsue. *Phys. Chem. Chem. Phys.*, 12(34):10012–10017, 2010.

[202] C.-C Chen, Y Zhou, C. A Morris, J Hou, and L. A Baker. *Anal. Chem.*, 85(7):3621–3628, 2013.

[203] M Shen, R Ishimatsu, J Kim, and S Amemiya. *J. Am. Chem. Soc.*, 134(24):9856–9859, 2012.

[204] L Pastero, D Aquilano, and M Moret. *Cryst. Growth Des.*, 12(5):2306–2314, 2012.

[205] R Lide. *CRC Handbook of Chemistry and Physics*. CRC Press/Taylor and Francis, Boca Raton, 90th edition, 2008.

[206] J. S Newman. *Electrochemical Systems*. Wiley, New Jersey, 2004.

[207] S. M Hamza and S. K Hamdona. *J. Phys. Chem.*, 95(8):3149–3152, 1991.

[208] C. J Stephens, Y.-Y Kim, S. D Evans, F. C Meldrum, and H. K Christenson. *J. Am. Chem. Soc.*, 133(14):5210–5213, 2011.

[209] R. R Yadav, S. N Mudliar, A. Y Shekh, A. B Fulke, S. S Devi, K Krishnamurthi, A Juwarkar, and T Chakrabarti. *Process Biochem.*, 47(4):585–590, 2012.

[210] H. A Al-Hosney and V. H Grassian. *J. Am. Chem. Soc.*, 126(26):8068–8069, 2004.

[211] K Friis, R. G Najjar, M. J Follows, S Dutkiewicz, A Körtzinger, and K. M Johnson. *Biogeosciences*, 4(2):205–213, March 2007.

[212] M. K Conyers, C. L Mullen, B. J Scott, G. J Poile, and B. D Braysher. *Aust. J. Exp. Agric.*, 43(1):71–78, 2003.

[213] W De Muynck, N De Belie, and W Verstraete. *Ecol. Eng.*, 36(2):118–136, February 2010.

[214] R. S Arvidson, I. E Ertan, J. E Amonette, and A Luttge. *Geochim. Cosmochim. Acta*, 67(9):1623–1634, 2003.

[215] E Ruiz-Agudo, M Kowacz, C. V Putnis, and A Putnis. *Geochim. Cosmochim. Acta*, 74:1256–1267, 2010.

[216] E Ruiz-Agudo, C. V Putnis, L Wang, and A Putnis. *Geochim. Cosmochim. Acta*, 75:3803–3814, 2011.

[217] F Xu, W. Q Zhu, L Yan, H Xu, L. H Xiong, and J. H Li. *Org. Electron.*, 13(2):302–308, February 2012.

[218] P. R Unwin and R. G Compton. *J. Chem. Soc. Faraday Trans.*, 86(9):1517–1525, 1990.

[219] R. G Compton, K. L Pritchard, P. R Unwin, G Grigg, P Silvester, M Lees, and W. A House. *J. Chem. Soc. Faraday Trans. 1*, 85(12):4335–4366, 1989.

[220] A Lea, J Amonette, D Baer, Y Liang, and N Colton. *Geochim. Cosmochim. Acta*, 65(3):369–379, February 2001.

[221] A Godelitsas, J. M Astilleros, K. R Hallam, J Löns, and A Putnis. *Mineral. Mag.*, 67(6):1193–1204, December 2003.

[222] N Sa and L. A Baker. *J. Am. Chem. Soc.*, 133(27):10398–10401, July 2011.

[223] L Luo, D. A Holden, and H. S White. *ACS Nano*, 8(3):3023–3030, March 2014.

[224] M Davenport, K Healy, M Pevarnik, N Teslich, S Cabrini, A. P Morrison, Z. S Siwy, and S. E Létant. *ACS Nano*, 6(9):8366–8380, September 2012.

[225] C. A Morris, A. K Friedman, and L. A Baker. *Analyst*, 135(9):2190–2202, June 2010.

[226] J. D Piper, C Li, C.-j Lo, R Berry, Y Korchev, L Ying, and D Klenerman. *J. Am. Chem. Soc.*, 130(31):10386–10393, August 2008.

[227] C Laslau, D. E Williams, and J Travas-Sejdic. *Prog. Polym. Sci.*, 37(9):1177–1191, September 2012.

[228] N Ebejer, A. G Güell, S. C. S Lai, K McKelvey, M. E Snowden, and P. R Unwin. *Ann. Rev. Anal. Chem.*, 6:329–351, April 2013.

[229] S. C. S Lai, J. V Macpherson, and P. R Unwin. *MRS Bull.*, 37(07):668–674, July 2012.

[230] J Gorelik, A. I Shevchuk, G. I Frolenkov, I. A Diakonov, M. J Lab, C. J Kros, G. P Richardson, I Vodyanoy, C. R. W Edwards, D Klenerman, and Y. E Korchev. *Proc. Natl. Acad. Sci. U. S. A.*, 100(10):5819–5822, May 2003.

[231] V. O Nikolaev, A Moshkov, A. R Lyon, M Miragoli, P Novak, H Paur, M. J Lohse, Y. E Korchev, S. E Harding, and J Gorelik. *Science*, 327(5973):1653–1657, March 2010.

[232] P Novak, A Shevchuk, P Ruenraroengsak, M Miragoli, A. J Thorley, D Klenerman, M. J Lab, T. D Tetley, J Gorelik, and Y. E Korchev. *Nano Lett.*, 14(3):1202–1207, March 2014.

[233] D Klenerman, Y. E Korchev, and S. J Davis. *Curr. Opin. Chem. Biol.*, 15(5):696–703, 2011.

[234] J Rheinlaender, N. A Geisse, R Proksch, T. E Schäffer, and T. E Schaffer. *Langmuir*, 27(2):697–704, January 2010.

[235] Z Siwy, E Heins, C. C Harrell, P Kohli, and C. R Martin. *J. Am. Chem. Soc.*, 126(35):10850–10851, September 2004.

[236] R. J White and H. S White. *Langmuir*, 24(6):2850–2855, March 2008.

[237] N Sa, W.-J Lan, W Shi, and L. A Baker. *ACS Nano*, 7(12):11272–11282, 2013.

[238] S Manne, J. P Cleveland, H. E Gaub, G. D Stucky, and P. K Hansma. *Langmuir*, 10(12):4409–4413, December 1994.

[239] W. F Heinz and J. H Hoh. *Biophys. J.*, 76(1):528–538, January 1999.

[240] T Miyatani, S Okamoto, A Rosa, O Marti, and M Fujihira. *Appl. Phys. A*, 66:S349–S352, 1998.

[241] A. C Hillier, S Kim, and A. J Bard. *J. Phys. Chem.*, 100(48):18808–18817, January 1996.

[242] C.-C Chen and L. A Baker. *Analyst*, 136(1):90–97, 2011.

[243] H. V Powell, M Schnippering, M Mazurenka, J. V Macpherson, S. R Mackenzie, and P. R Unwin. *Langmuir*, 25(1):248–255, January 2009.

[244] A. K Chauhan, D. K Aswal, S. P Koiry, S. K Gupta, J. V Yakhmi, C Sürgers, D Guerin, S Lenfant, and D Vuillaume. *Appl. Phys. A*, 90(3):581–589, November 2007.

[245] J Kim, M Shen, N Nioradze, and S Amemiya. *Anal. Chem.*, 84(8):3489–3492, 2012.

[246] S Umehara, N Pourmand, C. D Webb, R. W Davis, K Yasuda, and M Karhanek. *Nano Lett.*, 6(11):2486–2492, November 2006.

[247] M. L Kovarik, K Zhou, and S. C Jacobson. *J Phys. Chem. B*, 113(49):15960–15966, December 2009.

[248] M. A Edwards, C. G Williams, A. L Whitworth, and P. R Unwin. *Anal. Chem*, pages 4482–4492, April 2009.

[249] S. H Behrens and D. G Grier. *J. Chem. Phy.*, 115(14):6716–6721, 2001.

[250] K van der Maaden, K Sliedregt, A Kros, W Jiskoot, and J Bouwstra. *Langmuir*, 28(7):3403–3411, 2012.

[251] R. W Clarke, A Zhukov, O Richards, N Johnson, V Ostanin, and D Klenerman. *J. Am. Chem. Soc.*, 135(1):322–329, 2012.

[252] J. P Guerrette and B Zhang. *J. Am. Chem. Soc.*, 132(48):17088–17091, December 2010.

[253] D Momotenko and H. H Girault. *J. Am. Chem. Soc.*, 133(37):14496–14499, September 2011.

[254] P. J Yunker, T Still, M. A Lohr, and A. G Yodh. *Nature*, 476(7360):308–311, August 2011.

[255] A. V Ryzhkova, M Škarabot, and I Muševič. *Phys. Rev. E*, 91(4):42505, April 2015.

[256] H Ohshima, T. W Healy, and L. R White. *J. Colloid Interface Sci.*, 90(1):17–26, November 1982.

[257] N Tufenkji and M Elimelech. *Langmuir*, 21(3):841–52, February 2005.

[258] V Hirsch, C Kinnear, M Moniatte, B Rothen-Rutishauser, M. J. D Clift, and A Fink. *Nanoscale*, 5(9):3723–32, May 2013.

[259] P Zhu, Y Masuda, and K Koumoto. *Biomaterials*, 25(17):3915–21, August 2004.

[260] A Abdullah Ceyhan and A Nusret Bulutcu. *J. Cryst. Growth*, 327(1):110–116, July 2011.

[261] J Vandiver, D Dean, N Patel, W Bonfield, and C Ortiz. *Biomaterials*, 26(3):271–283, January 2005.

[262] N. H Lin, W.-Y Shih, E Lyster, and Y Cohen. *J. Colloid Interface Sci.*, 356(2):790–7, April 2011.

[263] T Yeung, G. E Gilbert, J Shi, J Silvius, A Kapus, and S Grinstein. *Science*, 319(5860):210–3, January 2008.

[264] C. C Fleischer and C. K Payne. *J. Phys. Chem. B*, 116(30):8901–7, August 2012.

[265] J. F. M Oudenhoven, L Baggetto, and P. H. L Notten. *Adv. Energy Mater.*, 1(1):10–33, January 2011.

[266] J Chmiola, G Yushin, Y Gogotsi, C Portet, P Simon, and P. L Taberna. *Science*, 313(5794):1760–3, September 2006.

[267] H Ji, X Zhao, Z Qiao, J Jung, Y Zhu, Y Lu, L. L Zhang, A. H MacDonald, and R. S Ruoff. *Nat. Commun.*, 5:3317, January 2014.

[268] J. D Norton, H. S White, and S. W Feldberg. *J. Phys. Chem.*, 94(17):6772–6780, August 1990.

[269] J Xiong, Q Chen, M. A Edwards, and H. S White. *ACS Nano*, 9(8):8520–9, August 2015.

[270] K McKelvey, S. L Kinnear, D Perry, D Momotenko, and P. R Unwin. *JACS*, 2014.

[271] D Perry, R Al Botros, D Momotenko, S. L Kinnear, and P. R Unwin. *ACS Nano*, 9(7):7266–76, July 2015.

[272] D. C Grahame. *J. Am. Chem. Soc.*, 68(2):301–310, February 1946.

[273] M. A Baldo, S Daniele, M Corbetta, and G. A Mazzocchin. *Electroanalysis*, 7(10):980–986, October 1995.

[274] D. Y Petrovykh, H Kimura-Suda, A Opdahl, L. J Richter, M. J Tarlov, and L. J Whitman. *Langmuir*, 22(6):2578–87, March 2006.

[275] A. S Parker, A. N Patel, R Al Botros, M. E Snowden, K McKelvey, P. R Unwin, A. T Ashcroft, M Carvell, A Joiner, and M Peruffo. *J. Dent.*, 42 Suppl 1:S21–9, June 2014.